MULTI-FIDELITY WIND TURBINE SIMULATION AND WIND ASSESSMENT AT MASDAR CITY

By

Liu Su

A Thesis Presented to the

Masdar Institute of Science and Technology

in Partial Fulfillment of the Requirements for the Degree of

Master of Science

in

Mechanical Engineering

MULTI-FIDELITY WIND TURBINE SIMULATION AND WIND ASSESSMENT AT MASDAR CITY

By Liu Su

A Thesis Presented to the Masdar Institute of Science and Technology in Partial Fulfillment of the Requirements for the Degree of

Master of Science in Mechanical Engineering

August 2012

AUTHOR'S DECLARATION

I understand that copyright in my thesis is transferred to Masdar Institute of Science and Technology.

Author _____

RESEARCH SUPERVISORY COMMITTEE MEMBERS

Dr. Isam Janajreh, Chair, _____

Masdar Institute of Science and Technology

Dr. Hassan E. S. Fath, _____

Masdar Institute of Science and Technology

Dr. Muhammad Hajj, _____

Virginia Tech

Abstract

Wind energy is undergoing unmatched growth amongst renewable energy portfolios with over 25% annual increase in deployment. Since the regional wind pattern has tremendous influence on wind project development, characterizing the wind at a given site becomes an indispensable step. BEM based engineering models are still dominating among wind turbine R&D community due to their low computational requirement and high accuracy. Furthermore, advanced development in computation power, computational algorithms and memory storage render the migration into high fidelity CFD wind turbine simulation.

This work began by first, characterizing the wind in Masdar City. Both low and high resolution wind data were collected. Intermittency was identified by initially utilizing FFT then by wavelet analysis to remedy the shortcomings of FFT by preserving the time-scale information. Then the analysis focused on the wind power assessment starting by fitting the wind data with Weibull distribution. Two wind turbines were considered to explore their power generation under the measured Masdar City low density wind pattern.

The second part of the work focused on developing a BEM based MATLAB code as a low fidelity tool to assess wind turbine performance. The code was first validated against the NREL phase VI experimental data before applying it to the 3.5KW Windspot. The power generations under different operational conditions were obtained and several key parameters, i.e. TSR, Twist angle, and Pitch angle, were genuinely studied and discussed. Results suggested that designing wind turbine blades with proper twist angle, operating wind turbine under proper TSR and Pitch angle can lead to a substantial increase in power generation.

Finally, high fidelity CFD simulation was explored to provide better insight for the flow over the 3.5KW Windspot. The flow domain was discretized using ICEM CFD and the model was comprised of 4.5 million hexahedral elements. The blade was wrapped with high resolution O-grid mesh to achieve reasonable y+ value. The model features SRF formulation and RANS based SST k-ω turbulence model. The results showed good agreement with experimental data and the extended running cases suggest 3.5KW Windspot has a high power coefficient within the TSR range between 4.0 and 6.0.

This research was supported by the Government of Abu Dhabi to help fulfill the vision of the late President Sheikh Zayed Bin Sultan Al Nayhan for sustainable development and empowerment of the UAE and humankind.

Acknowledgments

It is a good opportunity to thank many people who made this thesis possible. This work would not have been possible without the support from my research advisor, Dr. Isam Janajreh, under whose guidance I chose this topic. I would like to gratefully acknowledge the supervision of my advisor who has been abundantly helpful and has assisted me in numerous ways. I specially thank him for his infinite patience. The discussions I had with him were invaluable. I would like to thank the members of my research supervisory committee, Dr. Hassan E. S. Fath and Dr. Muhammad Hajj, for their valuable discussion and fruitful comments. I would like to say a big thanks to my fellow colleagues and friends Syed Shabbar Raza, Ilham Talab, Rana Qudaih, Fabian Hampp, Arnar Snaer Valmundsson, and Rasha Abd Rabu for sharing their enthusiasm vision and courage.

Most importantly, I would like to give my sincere thanks to my parents: Wenying Liu and Zhensong Su for their infinite love and I am indebted to them.

Liu Su,

Waste to Energy lab, Masdar Institute

Masdar City, June 25, 2012

Contents

List of Tables

List of Figures

CHAPTER 1

Introduction

1.1 Problem definition

Due to the rise of the world population and rapid pace of industrial development in emerging countries such as Brazil, Russia, India and China, the world's high demand for energy continues to grow. Currently, energy is mainly provided by fossil fuel, geothermal, wind, solar and nuclear energy. Among those energy sources, fossil fuel is still the main source of world energy consumption even though the reserves of oil, coal and gas projected to vanish in approximately 35, 107 and 37 years, respectively [1]. Much attention is paid to wind and solar energy which are regarded as both clean and sustainable energy. By possessing advantages such as technological mature, progressive infrastructure and relatively low cost, wind energy offers a cost-efficient alternative renewal energy source [2] and thus becomes competitive in the energy market. Since using wind energy as a main energy source is planned in countries such

as Denmark, Germany, China and United States [3], it is expected to play a more important role in meeting the current and future world's energy demand now and in the future.

The world has great wind energy potential which has been estimated to secure 96 PWh electricity production per year [4], which was 3 times the world electricity consumption in 2008 [5]. A more conservative assessment was given by Wijk and Coelingh [6], indicating the global wind energy potential was 20,000 TWh per year. As wind energy is becoming more mature technologically, regions such as Europe, North America, China and India continue to open their markets for wind turbine installation. The vast potential for wind power development in Asia, Latin America, Africa and the Middle East is illustrated by the Global Wind Energy Council (GWEC) [3]. For the past five years, UAE has shown its commitment to the area of renewable energy. In 2009, Abu Dhabi announced its plans to offset at least 7% of its electricity generation capacity based on renewable energy sources by 2020 [7]. Together with the Abu Dhabi offshore wind energy plan, wind energy is expected to play an indispensable role in those renewable energy development plans.

The Gulf region, especially UAE is facing similar kind of environmental problems. The fast growing economy and a high demand of energy is met by fossil fuel recourses. According to World Wildlife Fund (WWF) Living Planet 2008 report, the UAE stands ahead of United States and Kuwait in terms of carbon footprint per capita [8]. It is a huge challenge to reduce the emission, which, however, can be achieved by shifting the energy production method toward renewable and more sustainable technologies. As wind energy is widely utilized and regarded as a substitute for fossil fuel, the research on regional wind energy and wind turbine technology becomes essential.

1.2 Motivation

Unlike conventional energy source, e.g. fossil fuel, with high energy density, wind energy exhibits relatively low energy density and blows randomly. Due to both the spatial and temporal variations of the wind, characterize of regional wind is of utmost importance. The knowledge of the wind characteristics at a particular site can influence at least the following work: system design, performance evaluation, site choosing, and the operation of a system. These are the reasons why characterizing regional wind has always been the very first step of wind related projects development.

As wind turbine is the main energy harvesting device from wind, it increasingly attracts much attention from scientists, researchers and engineers from different fields. The size of commercial wind turbines has increased dramatically in the last 30 years from approximately a rated power of 50 KW and a rotor diameter of 10-15m up to today's commercial available 7 MW wind turbine with a rotor diameter of 164m. The ever-increasing of the wind turbine size and the high requirement for their energy capture ability have forced the designers to seek not only simple tools that based on simple static calculations but also dynamic and high fidelity simulation.

BEM is still one of the most widely used tools for designing wind turbines and estimating their performance. It is computationally cheap and fast; besides, relatively accurate results can be obtained provided the accuracy of required input data can be maintained. Nevertheless, due to the assumptions made when deriving the technique, the defects become inevitable. As a result, some corrections have to be introduced until BEM can be relied on as an engineering tool.

Benefiting from the advancement in computation power, computation algorithm and storage memory, the usage of CFD on wind energy continues to draw much attention. In 2000, the National Renewable Energy Laboratory (NREL) made an initial comparison between the experimental results and that from CFD simulation which was the first real proof that CFD for wind turbine rotor application can be useful. Compared to BEM, CFD has less assumption and models the physical phenomenon reasonably accurate. Besides, it gives one the opportunity to have an insight look at the flow around wind turbine blades but with more computation effort and higher cost.

1.3 Objectives

It is of enormous importance to characterize the regional wind pattern. Due to lack of wind data, the thesis work will start with collecting both high resolution and low resolution wind data in Masdar City. Based on the collected data, different analyses will be explored and models will be built. Turbulence intensity, average wind speed and average wind power density can be then identified. FFT and Wavelet analysis will be utilized to identify the frequency/scale information in the data. Probability analysis will be carried out, based on which the possible power generation of two wind turbines (small and large scale) can be explored.

Due to the inevitable defects of BEM technique, it has to be studied carefully together with its corrections before being applied to a given HAWT. Corrections such as Tip loss correction, Buhl empirical correction, Skewed wake correction and 3D correction of Snel et al. will be included. An improved BEM code for HAWT application will be developed incorporating the aforementioned corrections. The code will be first implemented on UAE phase-VI turbine for validation. It will be then applied on

3.5KW Windspot to estimate its performance under different operation conditions. Since the key success for BEM is to obtain accurate aerodynamic coefficients (C_d and C_l) which are lacking for the 3.5KW Windspot airfoil, two levels of simulation are pursued to obtain such aerodynamic data, i.e. panel method and CFD simulation. Following the development of an improved BEM model, the key wind turbine parameters such as twist angle, pitch angle, TSR, etc., will be studied. As a result, recommendations will be given for turbine blade design and wind turbine operation.

In order to remedy the defects of BEM technique and have an insight look at the flow over wind turbine blades, 3D high fidelity CFD simulation will be also explored. The 3.5KW Windspot will be meshed in ANSYS ICEM with complete hexahedral elements, and imported into FLUENT environment. Upon conducting further simulation, the model will be validated by mesh sensitivity study. SST k-ω turbulence model will be utilized for turbulence modeling. The power generation under different operation conditions will be obtained, meanwhile, the flow over the blade will be carefully studied.

CHAPTER 2

Literature Review

2.1 Wind energy and wind turbine introduction

A wind turbine is a device that converts the kinetic energy of the wind into mechanical energy. Depending on whether to use mechanical energy for electricity production or drive force, the device is called wind generator or windmill. The usage of wind energy dates back to the 14th century when Dutch windmills were used to drain areas of the Rhine delta. The first electricity generating wind turbine was installed in 1887 with a battery charging machine. While the first utility grid-connected wind turbine to operate in the UK was built by John Brown & Company in 1951 in the Orkney Islands.

2.1.1 HAWT VS VAWT

Wind turbines, according to the rotating axis, can be categorized into Horizontal Axis Wind Turbine (HAWT) and Vertical Axis Wind Turbine (VAWT). VAWTs have the

main rotor shaft arranged vertically. Advantages of this arrangement can be, first, the turbine does not need to be aligned to the oncoming wind to be effective, and second, the generator and gear box can be placed near the ground, using a direct drive from the rotor assembly to the ground-based gearbox, hence improving accessibility for maintenance. However, it is suffering from more serious defects compare to HAWTs, which prevent it from being commercially implemented. As VAWTs are not tending to be mounted with a tall tower, less wind speed would be available to harness. And the inevitable high fatigue damages lead to short life cycle. Additionally, they are less efficient compare to HAWTs.

HAWT have the main rotor shaft and electrical generator at the top of a tower, and must be pointed to the wind. Small turbines are pointed by a simple wind vane, while large turbines generally use a servo motor. Gearbox is often included in the system, which turns the slow rotation of the blades into a quicker rotation that is more suitable to drive an electrical generator. Today, HAWTs have been widely used for energy harvesting due to, but not limited to, the following reasons:

- More efficient in harvesting wind energy.
- Operate in the high Atmospheric Boundary Layer (ABL) instead of the bottom shear layer, thereby, operating under more uniform and intense wind speeds.
- Have more stable mechanical behavior and could operate in large sizes.

Thus, the following discussion, analysis and simulation will be focus on HAWT.

2.1.2 Wind turbine size and main components

Wind energy market has always been extremely competitive; lead by the giants including GE (US), Vestas (Denmark), Sinovel (China), Siemens (Germany), Goldwind (China), who continue to perform aggressively in both domestic and

international wind energy market. Consequently, the size of wind turbines, as one of key parameters, has been increasing dramatically for the last three decades, as shown in Figure 2.1. In the early and mid-1980s, a typical wind turbine size was less than 100KW. Between the late 1980s and the early 1990s wind turbines increased in size from 100KW to 500KW and by the mid-1990s the typical size ranged from 775KW to 1000KW. So far, the capacity of commercial available wind turbine can reach as high as 7 MW [9], with a rotor diameter of 164m, and a swept area of more than 21000 m^2.

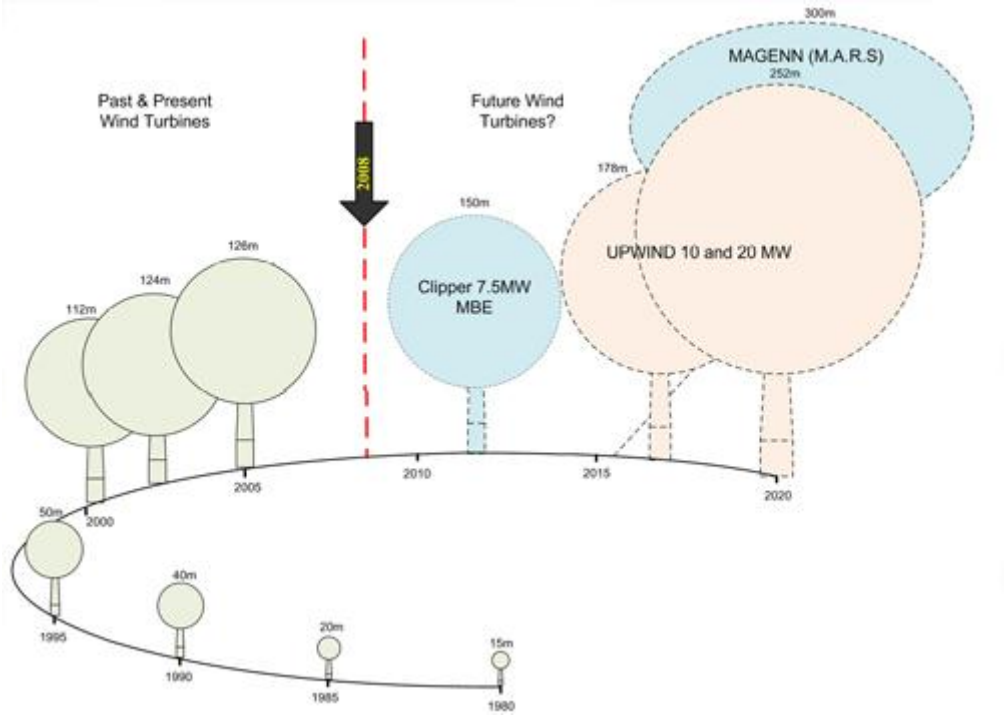

Figure 2. 1 Growth of wind turbine size

Corresponding to the size and capability of wind turbines, wind turbines can be classified into three broad classes: the utility class, the industrial class, and the residential class [10].

The principal components for wind turbines are the rotor, the drive train, the main frame, the yaw system, and the tower. The rotor includes the hub and the blades; the drive train includes the gearbox (if any), the generator, mechanical brake, and shafts

and couplings connecting them; the yaw system includes at least a yaw bearing and may include a yaw drive, yaw brake and yaw damper. The main frame provides support for mounting other components and a means for protecting them by the nacelle cover; the tower group includes the tower itself, its foundation, and may include the means for self-erection of the machine. A simplified picture is shown in Figure 2.2.

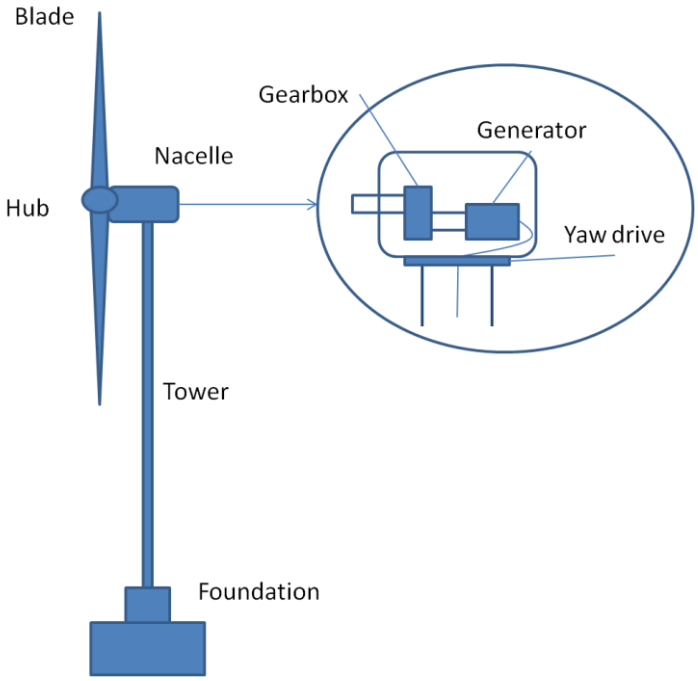

Figure 2. 2 HAWT main components

The most fundamental components of the rotor are the blades. They are the devices that harvest energy from wind by converting the force of the wind into the torque needed to generate useful power. So careful attention need to be paid to the design, most of which may fall into two categories: aerodynamic performance and structural strength. Parameters such as solidity, airfoil shape, number of blades, have a huge impact on the wind turbine operation and power generation.

2.2 Wind energy implementation scenario

The usage of wind energy has appeared in human history as early as 5000 B.C. when people travelled along the Nile River with boats propelled by wind energy. Also in ancient China, people already started using windmills to pump water by 200 B.C. Windmills were used extensively in the Middle East for food production by the 11th century, which then influenced merchants and crusaders to carry this idea back to Europe. The Dutch adapted a new method of the windmill and used it to drain lakes and marshes in the Rhine River Delta. In the late 19th century, this technology was brought to the New World by settlers who then pumped water to farms and ranches and later generated electricity for homes and industry. In Europe and later in America, industrialization led a steady decline in the use of windmills. However, it also sparked the development of larger windmills in order to generate electricity. These windmills became known as wind turbines which appeared in Denmark as early as 1890. Electric power was fed to the local utility network for months during World War II by the largest wind turbine known in the 1940's. This wind turbine sat on a Vermont Hilltop known as Grandpa's Knob and was rated at 1.25 megawatts in winds of about 30 mph. Popularity of wind energy usage has always fluctuated with the price of fossil fuels. Interest in wind turbines waned after World War II when fuel prices fell. But by the 1970s, when price of oil escalated, the interest in wind turbine generators rose proportionately. For many years to come, the fastest growing energy source of wind energy will power industry, business and homes with clean renewable electricity.

The use of wind energy in the world has exhibited a large increase in recent years. In 2010, the world total installed capacity was 196,630 MW, which was almost 9 times the installed capacity in 2001, as shown in Figure 2.3.

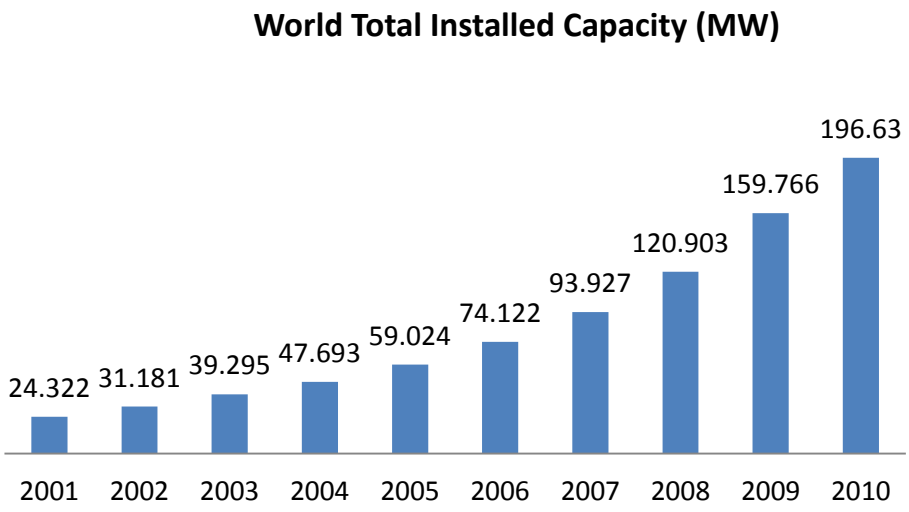

Figure 2. 3 World total installed capacity (2001-2010)

According to the published data from the World Wind Energy Association (WWEA) in 2010, the worldwide capacity reached 196,630 MW, out of which 37,642 MW were added in 2010, slightly less than in 2009. The wind power showed a substantial growth rate of 23.6%. China became number one in total wind installed capacity and the center of the international wind industry, and added 18,928 MW within one year, accounting for more than 50% of the world market for new wind turbines. Many western European countries are showing stagnation, whereas there is strong growth in a number of eastern European countries. It is foreseen that a global capacity of 600,000 MW by the year 2015 and a global capacity of more than 1,500,000 MW by the year 2020 would be possible.

2.3 Wind turbine aerodynamic models review

The wind energy has seen significant developments compare to when it first became commercially available. Models like Blade Element Momentum (BEM) method, panel and vortex methods, actuator disc method and Navier-Stokes solvers have been used in analyzing wind turbine forces and performances.

2.3.1 BEM Method

BEM theory is one of the oldest and most commonly used methods for analyzing wind turbine forces and performances. This theory is an extension of actuator disk theory, which was first proposed by the pioneering work of Rankine and Froude in the late 19th century. The BEM theory, generally attribute to Betz and Glauert [11], and was derived by combining the blade element theory and the momentum method. Blade element theory assumes that blades can be divided into small elements that act independently of surrounding elements and operate aerodynamically as two-dimensional airfoils whose aerodynamic forces can be calculated based on the local flow conditions. The forces exerted on these elements are summed along the span of the blade to calculate the total forces and moments exerted on the turbine. The other half of BEM, the momentum theory, assumes that the loss of pressure or momentum in the rotor plane is caused by the work done by the airflow passing through the rotor plane on the blade elements. Using the momentum theory, one can calculate the induced velocities from the momentum which lost in the flow in the axial and tangential directions. These induced velocities affect the inflow in the rotor plane and therefore also affect the forces calculated by blade element theory. This coupling of two theories ties together blade element momentum theory and sets up an iterative process to determine the aerodynamic forces and also the induced velocities near the rotor.

As BEM is derived with lots of assumptions and simplifications, limitations present in the method inevitably. In practice, it is those corrections that make BEM method applicable in wind turbine design. It includes Tip loss correction [12], Hub loss correction [13], Glauert correction [14], Skewed wake correction [15] and “3D correction” of Snel et al. [16]. Details can be found in Chapter 3.

2.3.2 Panel and vortex method

3D inviscid aerodynamic models are developed in attempt to obtain a more detailed description of the 3D flow that develops around a wind turbine. The fact that viscous effects are neglected is certainly restrictive as regards the usage of such models on wind turbines. However, they did help us understand the dynamic inflow effects as well as provided a better insight into the overall flow development [17, 18]. Attempts of incorporating viscous effects into those inviscid models by using viscous-inviscid interaction techniques have been explored [19]; however, they are still not mature enough to become engineering tools according to Hansen et al. [20].

In vortex models the rotor blades, trailing and shed vortices in the wake are represented by lifting lines or surfaces [21]. On the blades the vortex strength is determined from the bound circulation that stems from the amount of lift created locally by the flow past the blades. The trailing wake is generated by the spanwise variation of the bound circulation while the shed wake is generated by a temporal variation and ensures that the total circulation over each section along the blade remains constant in time. Knowing the strength and position of the vortices the induced velocity can be found in any point using the Biot–Savart law.

The inviscid incompressible flow past the blades can be found numerically by applying a surface distribution of sources and dipoles. This is the approach followed by panel method and is fundamentally based on Green's theorem which allows obtaining an integral representation of any potential flow field in terms of singularity distribution. The active boundary of the flow includes both the solid boundaries as well as the wake surfaces. Dipoles are added so as to develop circulation into the flow to simulate lift.

2.3.3 Generalized actuator disc models

As the oldest analytical tool for analyzing rotor performance, it still reveals its popularity among wind energy applications. In the model, the rotor is represented by a permeable disc that allows the flow to pass through the rotor and is subjected to surface force simultaneously. The classical actuator disc model is based on conservation of mass, momentum and energy, and constitutes the main ingredient in the 1D momentum theory, as originally formulated by Rankine [22]. When combining it with a blade element theory, one end up with the well-known BEM method, as discussed before. In its general form, however, the actuator disc model can be combined with the Euler or NS equations.

Wu conducted the pioneering work using actuator disc model analyzed the flow through a heavily loaded propeller [23] in 1962. Later, Greenberg et al. [24, 25] made improvements on the numerical treatment of the equations. Recently, Conway [26, 27] has further developed the analytical treatment of the method. Within wind turbine aerodynamics, Madsen [28] developed a semi-analytical actuator cylinder model to describe the flow field about a vertical-axis wind turbine. Later developments of the method have mainly been directed towards the use of the NS or Euler equations.

In a numerical actuator disc model, the NS (or Euler) equations are typically solved by a second order accurate finite difference/volume scheme, as in a usual CFD computation. However, the geometry of the blades and the viscous flow around the blades are not resolved. Instead the swept surface of the rotor is replaced by surface forces that act upon the incoming flow. This can be either implemented at a rate corresponding to the period-averaged mechanical work that the rotor extracts from the flow or by using local instantaneous values of tabulated airfoil data.

2.3.4 Navier-Stokes solvers

The first application of CFD to wings and rotor configurations were studied back in the late seventies and early eighties in connection with airplane wings and helicopter rotors using potential flow solvers [29-33]. A shift towards unsteady Euler solvers was seen through the eighties.

In the late nineties, with the CFD solver capable of handling viscous flow around rotors, its application on wind turbine rotors received much attention. The major part of wind turbine rotor computations performed until now has been focused on zero yaw rotor configuration, where nacelle and tower have been neglected, and the inflow to the rotor has been assumed to be steady without shear. These are, of course, great simplifications, but in many cases are still good approximations. The effect of the tower on the rotor on an upwind turbine is comparable to other unsteady effects, such as incoming turbulence, time variations of the rotor and of the incoming flow. However, those minor factors are attracting attentions as well. The most recent work have been conducted by Timothy [34] by taking atmospheric boundary layer (ABL) into consideration when simulating Wind Turbine Wake Interactions.

One of the first real proofs that CFD for wind turbine rotor applications can be useful came in connection with the comparison organized by the National Renewable Energy Laboratory (NREL) in Boulder, Colorado in December 2000 [35-37]. Some of these results were later published in [38, 39]. The published data revealed that CFD codes were consistently reproducing the measured distribution of the aerodynamic forces along the blade span for the 3D and under extreme stall conditions.

Turbulence modeling represent a key issue using these methods, since full DNS or LES simulations are far beyond present days computing capacity. Forced by

computational limitations, hybrid methods are emerging which mix conventional turbulence models with LES (see Johansen et al. [40]) referred to as Detached-Eddy Simulation (DES). Such methods include considerable more dynamics and three-dimensional flow behavior like spanwise development of vortex structures. Although 3D Navier-Stokes methods has a promising future, computing cost will limit their wider application for some time and give room for improvements of the simpler methods. Such necessary improvements of simpler methods range from better handling of coned rotors, rotors at high yaw angles, dynamic inflow, large tip-speed ratios, etc, to fundamental issues like tip correction, influence of pressure forces on expanding stream tubes, etc.

2.4 Summary

A general review of the wind turbine, its historical and recent development, and the development of analytical tools has been covered. It started with introducing the main components of wind turbine. Two types of wind turbines are compared: HAWT and VAWT, their advantages and disadvantages are addressed. The literature review focused on the current status of wind energy development. The current models and tools for designing wind turbine and analyzing wind turbine performance are discussed in depth. The models and techniques such as BEM method, generalized actuator disc model, panel and vortex method, NS solvers are widely used in different areas under different levels and circumstances.

CHAPTER 3

Wind energy assessment: Masdar City case study

In this chapter, an overview of wind energy assessment is given and Masdar City is taken here, as a case study.

3.1 Introduction

Masdar City is a living large scale laboratory, sustainable and emission free city and the home of Masdar Institute. Currently the city is overproducing nearly 10MW of additional solar (concentrated thermal and photovoltaic) power that is sent out to electrical grid. To diversify energy sources in the city, wind energy, waste to energy and geothermal energy portfolios are being explored. Globally, Wind energy has been observed tremendous growth. In China, wind energy market was doubled between 2006 and 2009 [41], whilst over 213MW wind turbine has been newly installed in

Africa and the Middle East region [42]. Locally, UAE is pursuing towards the inclusion of wind energy resource in their 7% renewable energy plan by 2020.

Measuring and analyzing wind data at a given site has always been the first step in any wind project development [43]. The main factors influencing power production at a given site over a period of time are: 1) the power curve of the wind turbine, 2) the annual distribution of wind velocity, and 3) their temporal characteristic, i.e. turbulence intensity, gust speed, intermittency, etc. The wind speed probability distributions are widely used in wind-related data analysis and applications [44-48]. Since Putnam [49] and Sherlock's [50] pioneer work, several distributions have been suggested as appropriate models. These include inverse Gaussian [51], log-normal [52], and Weibull [53]. Weibull distribution is the most widely used and has been found to fit a wide collection of recorded wind data [54-57].

Wind pattern tends to be localized despite its global planetary, and regional (hills lulls as well as sea breeze) heat driven mechanisms. In order to have a good understanding of wind capacity, regional annual records collection, data analysis, and model prediction, are all necessary. From wind speed records, one can estimate the average wind power density and infer their turbulence intensity and intermittency levels. Spatial data provides ABL information, allowing accurate incoming flow modeling and virtual assessment of the performance of given wind turbine configurations. Virtual wind tunnel simulation cut down upfront capital cost and reduces development risk while gaining confidence on wind turbine implementation.

In general, Arabian Peninsula eastern coastlines experience a relatively low level of wind; it also varies from one season to another. In Dhahran (26˚32′ N, 50˚13′ E, eastern coastal plain of Saudi Arabia), Elhadidy [58] reported annual average wind speed of 4.3 m/s in the period between 1986 and 1998, and monthly average wind

speed varying between 4m/s and 6.5m/s. Therefore, care must be taken in selecting the type and configuration of wind turbines in Abu Dhabi region as the mean local wind speed is at the borderline speed of many commercial wind turbines. Generally, wind turbine with a lower turning moment and, thereby, a lower cut-in speed is best suited for the eastern gulf region.

In this chapter, annual records, as well as high resolution records with small duration are collected first. These records are subjected to linear regression, spectrum and wavelet analyses and Weibull distribution fitting. As Masdar City has been categorized as poor wind region, the power curves of small and large size HAWT are coupled with the inferred Weibull distribution and recommendations to their regional implementation are made.

3.2 Masdar City Wind Data

Masdar City is located at 24.4202° N latitude and 54.6132° E longitude and is being constructed 17 kilometers southeast of the city of Abu Dhabi. A 50m tubular meteorological tower was installed at the Masdar City site and has been collecting continuous records of wind speed since the beginning of August, 2008 at a sampling interval/rate of 10 minutes. The mast is equipped with 5 calibrated Hersteller Thies Cilma cup anemometers [59], two wind vanes, one Campbell CR1000 data logger, and three sensors to measure temperature, barometric pressure and humidity [60]. It records five velocities (at 10m, 30m, 40m, 49m, and 50m), two directions (at 30m, and 50m) as well as pressure, relative humidity, and temperature at 50m. Figure 3.1 shows the daily average records at the height of 50m measured in the year 2010.

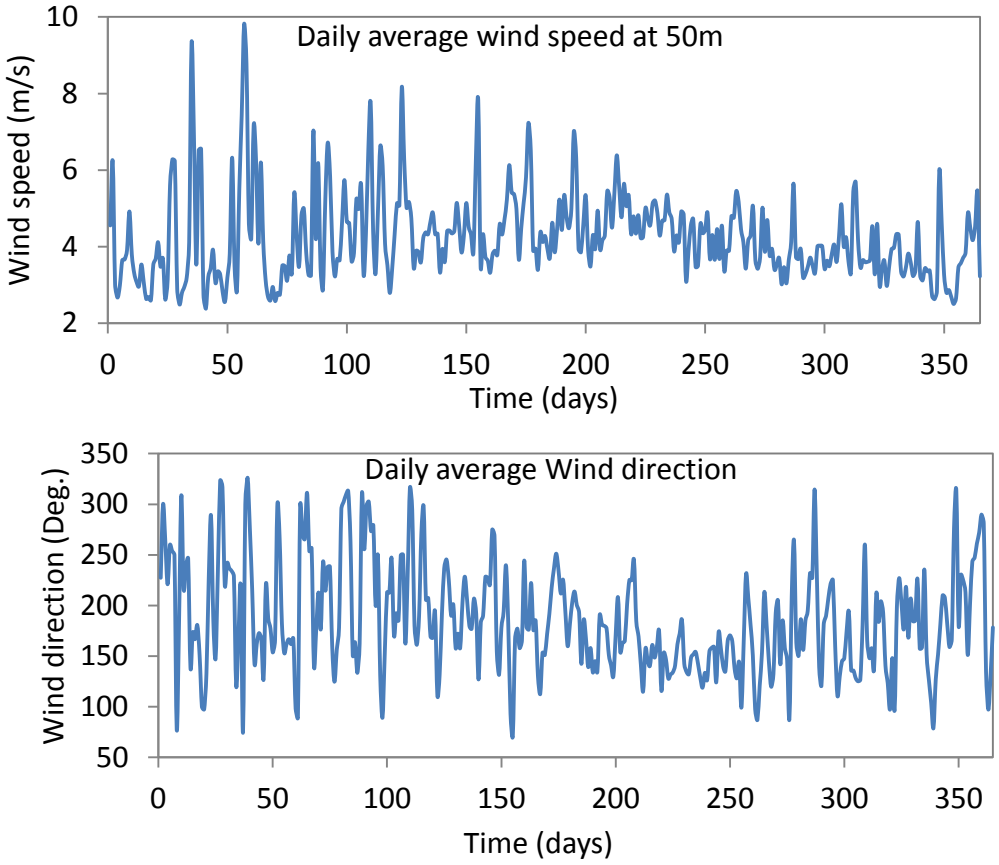

Figure 3. 1 Daily average wind speed and direction at 50m in 2010

As shown in Figure 3.1, the maximum daily wind speed for few days, i.e. day 55 to day 60, has reached 9.5 m/s, and on the average, the direction can be characterized as a southwestern direction. Figure 3.2 shows the monthly average wind speed at the height of 10m, 30m, 40m, and 50m.

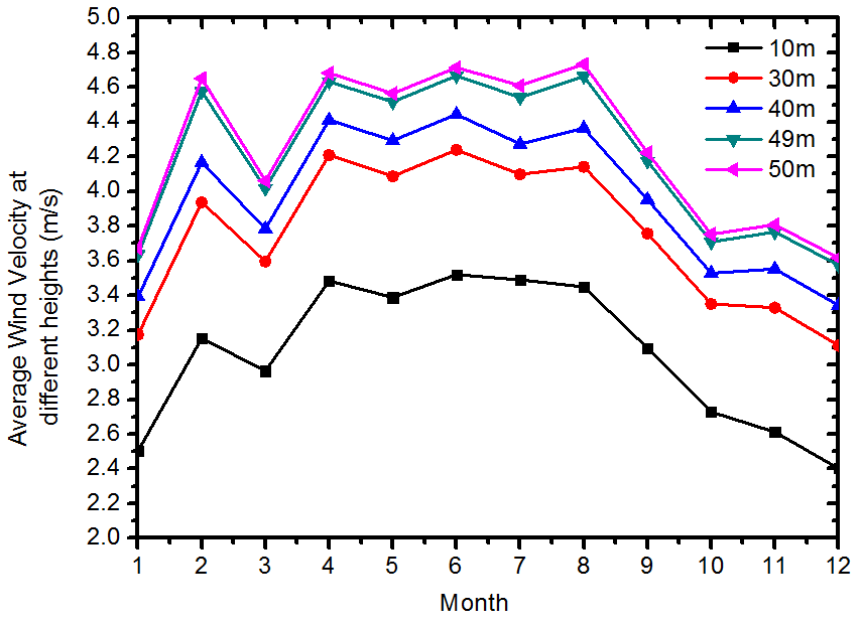

Figure 3. 2 Monthly average wind speed in 2010

As expected and shown in Figure 3.2, the wind becomes stronger as the height increases. The month of February, and April to August, are the windiest months in Masdar City, with the mean wind speed of around 4.5m/s, while other seasons especially the winter season, e.g. December, becomes calmer. The annual average wind speed is only near the cut-in wind speed of commonly used HAWT, i.e. Vestas, GE series, Sonkyo 3.5KW Windspot and Nordtank 500/41. Their technical specifications are summarized in Table 3.1.

Table 3. 1 Metrics of several Vestas and GE wind turbines

Wind turbine model	Rated power (KW)	Rated speed (m/s)	Cut-in/Cut-out speed (m/s)	Rotor diameter (m)	Hub height (m)
Vestas 52-850	850	16	4.0/25.0	52	44, 49, 55, 65,74
Vestas 82-1.65	1650	13	3.5/20.0	82	70, 78, 80
GE 1.5 sle	1500	14	3.5/25.0	77	65, 80
GE 1.5 xle	1500	11.5	3.5/20.0	82.5	80
Sonkyo 3.5KW windspot	3.5	12	1.5-3.0/NA	4.05	Suits any tower height
Nordtank 500/41	500	15	3.0-4.0/25.0	41	35 (ex. foundation)

The flow is fitted appropriately as a typical power law of open terrain with an exponential of 0.18 (0.13 for maximum speed) and ABL thickness 100m (fits both the annual average and annual maximum wind speed profiles), as shown in Figure 3.3.

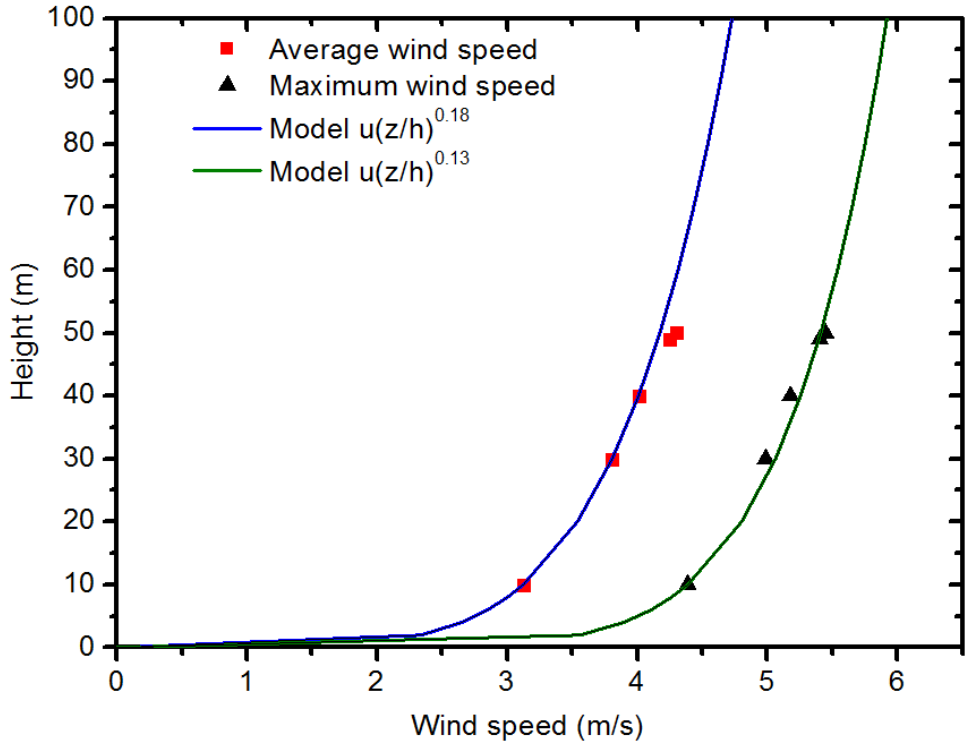

Figure 3. 3 Wind profile power law fitting for annual average wind speed and maximum wind speed

3.3 Wind data analysis and modeling

The annual wind data is collected and analyzed via models including available wind power, turbulence intensity, normal wind speed distribution, and Weibull wind speed distribution, as well as Fourier Transform (spectrum) and Wavelet analyses. The description and results of these models are given below.

3.3.1 Available wind power, Turbulence intensity and Normal probability density function

The mean wind power density is defined as

$$P = \frac{1}{2}\rho\overline{V}^3 \tag{3.1}$$

Where $\overline{V}$ is the annual mean wind speed and ρ is the air density. This is a conservative estimation that can be improved when explicit wind data is available, which is expressed by

$$P = \frac{1}{2}\rho\frac{\sum_{i=1}^{N} V_i^3}{N} \tag{3.2}$$

Where N is the number of data through a period of time (preferably over one year) and V_i is the measured wind velocity. Turbulence intensity is the Root Mean Square (RMS) of the data which is the ratio between the standard deviation of the wind speed to the mean wind speed and defined as

$$T_i = {}^{\sigma_v}/_{\overline{V}} \tag{3.3}$$

Where σ_v is the standard deviation, which is given by

$$\sigma_v = \sqrt{\frac{1}{N-1}\sum_{i=1}^{N}(V_i - \overline{V})^2} \tag{3.4}$$

The calculations for both the mean and standard deviation are conducted over a time period; the time period hereby is chosen to be 10 minutes as recommended in wind energy engineering [61]. For three directional probes, three intensities (RMS) can be measured, i.e. the dominant mainstream along the prevailing wind, the intermediate in the lateral direction and miniature vertical except near the ground surface.

Normal wind speed probability density function is a measure of the probability of wind velocity far/close to the mean wind speed, which can be described as

$$Pr = \frac{1}{\sigma_v\sqrt{2\pi}}\exp[-\frac{(V-\overline{V})}{2\sigma_v^2}] \tag{3.5}$$

3.3.2 Fourier Transform and Wavelet Transform

Frequency-domain of wind data is a powerful representative of periodic/semi-periodic data, which gives one possibility of looking at the data in another dimension. Fourier Transform (FT) and Wavelet Transform (WT) are two well-known mathematical methods.

FT is a mathematical operation that can decompose time-domain data into a compressed frequency-magnitude data. If f(t) is assumed to stand for the time-domain data which is continuous, then the mathematical expression of FT becomes:

$$F(f) = \int_{-\infty}^{+\infty} f(t) e^{-i2\pi ft} dt \tag{3.6}$$

Where f is the frequency variable, F(f) is the Fourier value in frequency domain. This is also called Continuous Fourier Transform (CFT) to be distinguished from Discrete Fourier Transform (DFT). Digital data are more are more practically follow DFT which is shown below.

$$F(f) = \frac{1}{N} \sum_{n=0}^{N-1} f(n)\, e^{-i2\pi fn/N} \tag{3.7}$$

In which f(n) stands for the discrete time-domain data, n is the data number, N is the number of all the discrete data. The DFT allows one to calculate the FT on a computer in a discrete way; however, it is inefficient especially when it is applied on a large branch of data. Several algorithms have been developed to make the transform efficient, in which the Cooley-Tukey FFT algorithm [62] is the most common and well known.

FT used to be the most popular signal processing tool, however it is only suitable when dealing with stationary data [63]. Short-Time Fourier Transform (STFT) was later developed to attempt the analysis of non-stationary signal. However, using STFT

involves making a choice to use either narrow window which produces good time resolution but poor frequency resolution or the opposite.

WT is used to analyze time-domain signals that contain non-stationary power at many different frequencies [64], and does not require one to make a compromise between time resolution and frequency resolution. It is mathematically defined by

$$W_n(s) = \sqrt{\frac{\delta t}{s}} \sum_{n'=0}^{N-1} f(n')\, \psi_0[\frac{(n'-n)\delta t}{s}] \tag{3.8}$$

Where $\sqrt{\frac{\delta t}{s}}$ is the normalization factor, s is the wavelet scale, $\psi_0(\eta)$ is the mother function. There are several proposed mother functions, e.g. Morlet, Paul, Mexican hat and DOG [65]. Morlet function was chosen in current study by virtue of its ability to reflect gradual changes in the climatic changes [66], as shown in equation (3.9).

$$\psi_0(\eta) = \pi^{-1/4} e^{iw_0\eta} e^{-\eta^2/2} \tag{3.9}$$

Where w_0 is the non-dimensional frequency, here is taken to be 6 to satisfy the admissibility condition [67]. It is necessary to choose a set of scales which can satisfy the resolution required. It is given by Torrence and Compo [65] that choosing scales as fractional powers of two is convenient, as shown in equation (3.10) and (3.11).

$$s_j = s_0 2^{j(\delta j)}, j = 0,1,2,3 \ldots, J \tag{3.10}$$

$$J = (\delta j)^{-1} \log_2(N\delta t/s_0) \tag{3.11}$$

Where s_0 is the smallest resolvable scale which equals $2\delta t$ and J determines the largest scale, δt is the equally time spacing. Value of δj decides the resolution, the smaller it is, the finer the resolution obtained. The smallest value of δj is 0.5 for the Morlet wavelet.

3.3.3 Weibull distribution and productivity calculation of real wind turbines

Weibull probability density function is characterized by its probability density function $f_{(V)}$ and cumulative distribution function $F_{(V)}$ as follows:

$$f_{(V)} = \frac{k}{c}\left(\frac{V}{c}\right)^{k-1} e^{-(V/c)^k} \text{ and } F_{(V)} = 1 - e^{-(V/c)^k} \tag{3.12}$$

Where c is the scale parameter, k is the shape parameter, which are solved by using the maximum likelihood method [68]. By using the iteration equation suggested by Seguro and Lambert [46] :

$$k = \left(\frac{\sum_{i=1}^{N} V_i^k \ln(V_i)}{\sum_{i=1}^{N} V_i^k} - \frac{\sum_{i=1}^{N} \ln(V_i)}{N}\right)^{-1} \tag{3.13}$$

Start the iteration procedure by setting initial value of k to be 2. After obtaining the value of k, c can be calculated by applying the following equation:

$$c = \left(\frac{1}{N}\sum_{i=1}^{N} V_i^k\right)^{1/k} \tag{3.14}$$

Note that the iteration equation (3.11) can only be used upon nonzero wind data. As the scale and shape parameters are obtained, the most wind speed V_{mp} and the wind speed carrying maximum energy V_{max} can be easily calculated by using the following two equations:

$$V_{mp} = c\left(\frac{k-1}{k}\right)^{1/k} \text{ and } V_{max} = c\left(\frac{k+2}{k}\right)^{1/k} \tag{3.15}$$

V_{max} is an important element to consider when choosing wind turbine for the site. It is preferred that the optimal rated wind speed (corresponding to both technical and economic considerations) of a wind turbine is close to V_{max}.

Following the calculation of $f_{(V)}$, the production of a real wind turbine can be calculated by using the following equation:

$$\overline{P} = \int_0^{\infty} P_{(V)} f_{(V)} dV \tag{3.16}$$

Where $P_{(V)}$ is the wind turbine power production under different wind speeds which can be easily obtained from the given or estimated power curve.

3.4 Results and discussions

3.4.1 Potential wind power

From the obtained wind data at different heights, Equation (3.2) is utilized for estimating the available wind power in Masdar City. Figure 3.4 shows the average monthly wind energy at different heights.

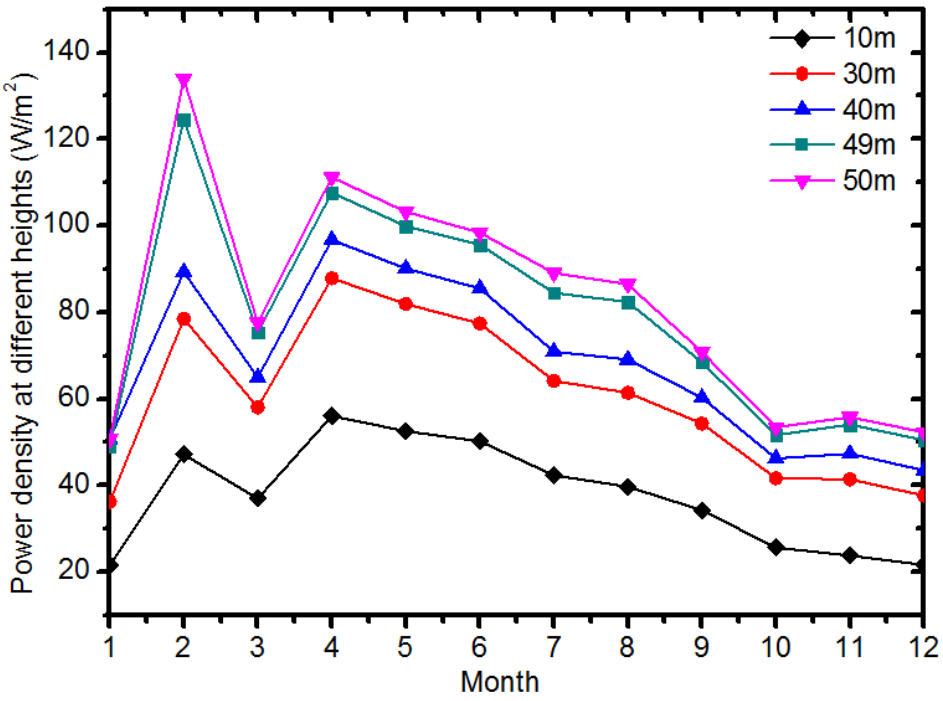

Figure 3. 4 Monthly available wind energy at different heights

It is clearly illustrated in Figure 3.4 that the highest wind energy can be extracted in February, while the lowest wind energy obtained in December. Average power of 37.36W/m^2, 59.56 W/m^2, 66.59 W/m^2, 77.86 W/m^2 and 81.08 W/m^2 can be harvested

annually from wind corresponding to the heights of 10m, 30m, 40m, 49m and 50m, respectively.

3.4.2 Turbulence intensity and Wind speed probability density function

Based on annual wind data in Masdar City, standard deviation and mean wind speed at different heights were obtained by utilizing Equation (3.4), whereas the turbulence intensity and wind speed probability density function are obtained using equation (3.3) and (3.5). The turbulence intensity calculation was conducted through the whole year every 10 mintues, the average value was taken and summarized in Table 3.2.

Table 3. 2 Mean wind speed and turbulence intensity at different heights

Height (m)	Yearly average wind speed (m/s)	Turbulence intensity (%)
10	3.06	19.82
30	3.74	15.01
40	3.95	14.03
49	4.20	12.97
50	4.25	12.71

Based on the values summarized in Table 3.2, Masdar City is classified as a high-turbulent region. One main reason to consider is that the average wind speed is low which add to the value of turbulence intensity significantly.

3.4.3 Fourier Transform and Wavelet Analysis

The monthly and annually average power spectrums were first computed, as shown in Figure 3.5.

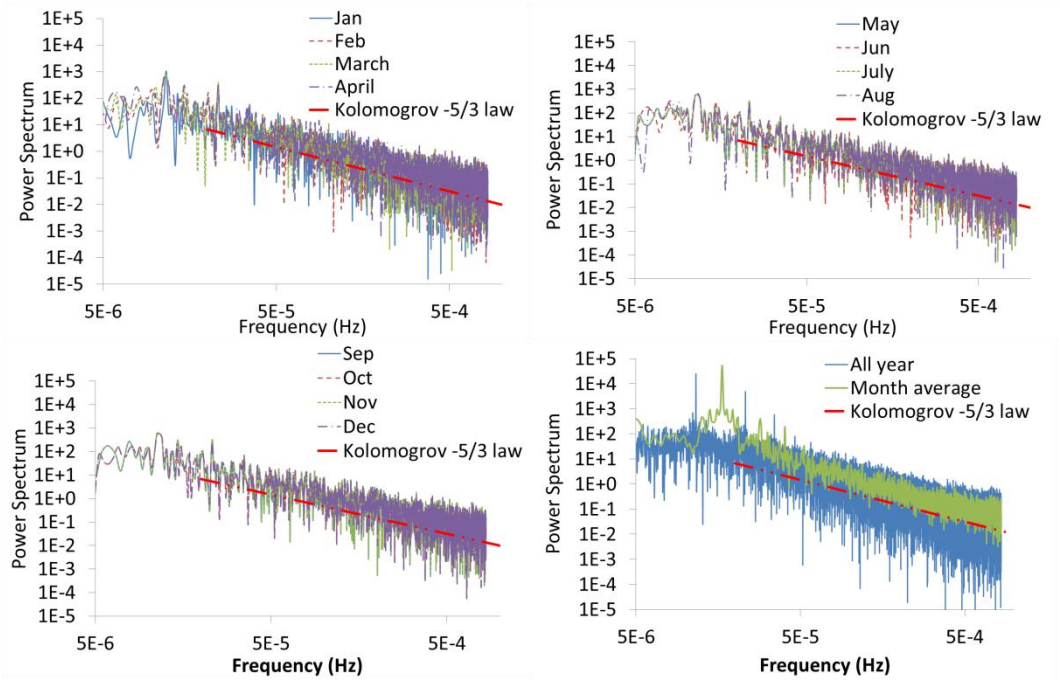

Figure 3. 5 Monthly and annual average power spectrum

As shown in Figure 3.5, the power spectrum does not have distinct frequency signature and appear to follow the Kolomogrove -5/3 turbulence order, which is generally observed in turbulence. Higher sampling rate data is also analyzed, as Shown in Figure 3.6, at 2 hours interval and at 1Hz sampling rate. It also demonstrated the intermittency of the Atmospheric Boundary Layer (ABL) and high energy eddies at low frequency with the falloff at high frequency. The spectrum with the energy contacting eddies occurs in the lower frequency region.

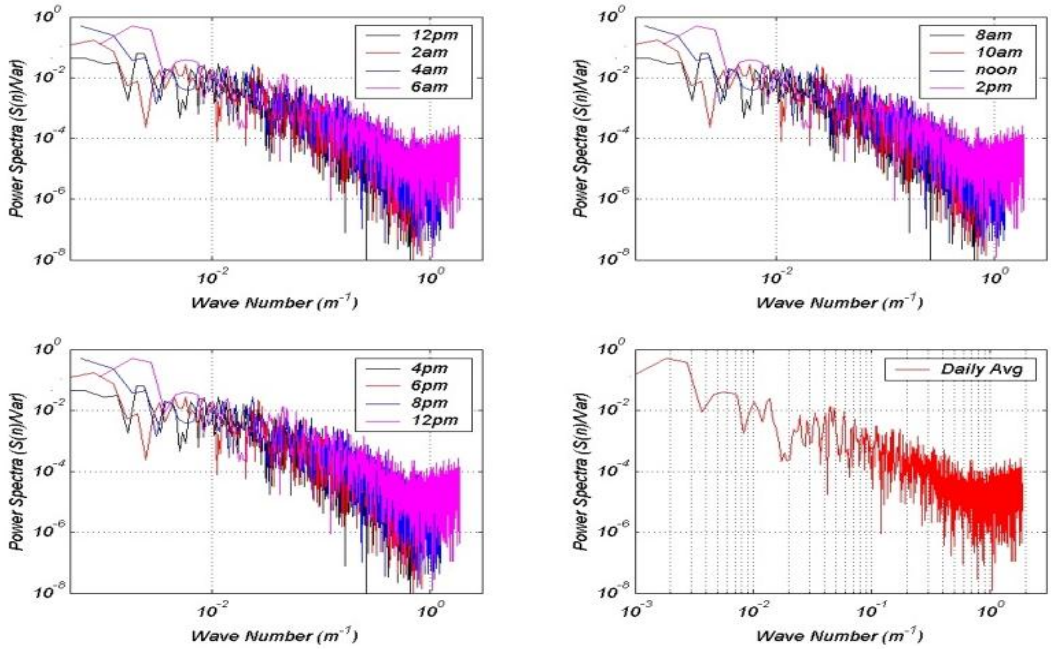

Figure 3. 6 Hourly and daily average power spectra at 1Hz sampling rate

As data is non-periodic and intermittent, wavelet analysis can remedy this shortcoming by combing time and scale analyses. For the data being analyzed, $N = 52560$, $\delta t = 10\text{min} = 0.17\text{h}$, $s_0 = 0.34\text{h}$, $\delta j = 0.25$ and $J = 59$, giving a total of 60 scales ranging from 0.34h to 9368.53h. The value of δj turns out to provide a smooth picture of wavelet power coefficient, as shown in Figure 3. 7.

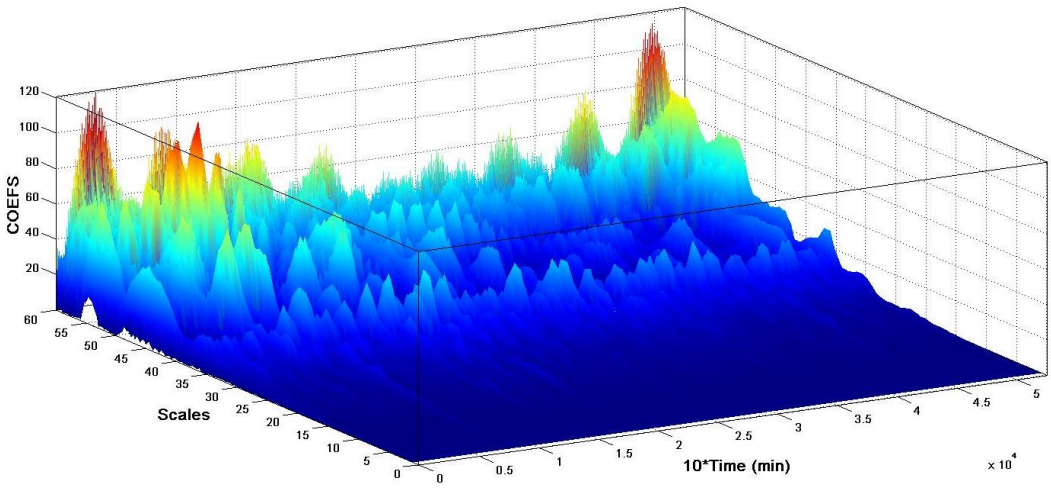

Figure 3. 7 Wavelet analyses of the one year data

Wavelet results demonstrate the large scale (low frequency) containing eddies appears at different times of the year. The intermediate scale between 30 and 40 appear to be universal while large scales are very intermittent as they appear to evolves in the 0-0.5, 0.75-1.5, 4.5-5 $\times 10^5$(min).

3.4.4 Weibull distribution

Following the iteration procedure proposed by equations 3.13 and 3.14, the scale parameter c and the shape parameter k at different heights are determined, thereby computed most wind speed (V_{mp}), and the wind speed carrying maximum energy (V_{max}). The results are summarized in Table 3.3.

Table 3. 3 Important parameters at different heights

Heights (m)	c (m/s)	k	V_{mp} (m/s)	V_{max} (m/s)
10	3.36	1.56	1.74	5.71
30	4.22	1.94	2.91	6.08
40	4.49	2.10	3.30	6.17
50	4.78	2.06	3.46	6.56

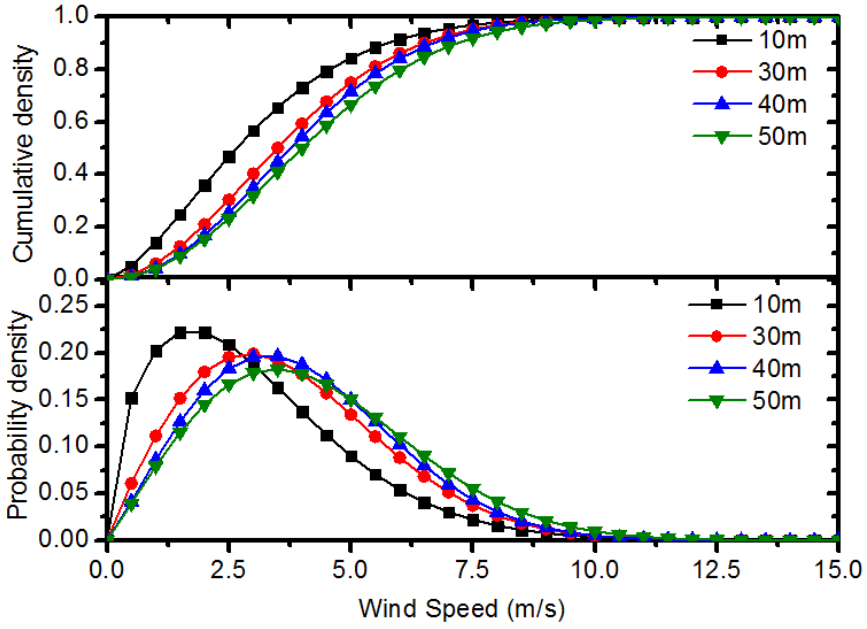

Figure 3. 8 Weibull probability and cumulative density distribution at different heights

The Weibull density distribution and Weibull cumulative density distribution is obtained for heights of 50 m, 40 m, 30 m and 10 m, as shown in Figure 3.8. As the height increases, the peak point in Weibull density distribution has the tendency of moving towards the higher wind speed values.

The wind speed density distribution obtained from measurement and Weibull fitting are shown in Figure 3.9. Due to the good fitting quality, the Weibull distribution is chosen for further wind turbine production.

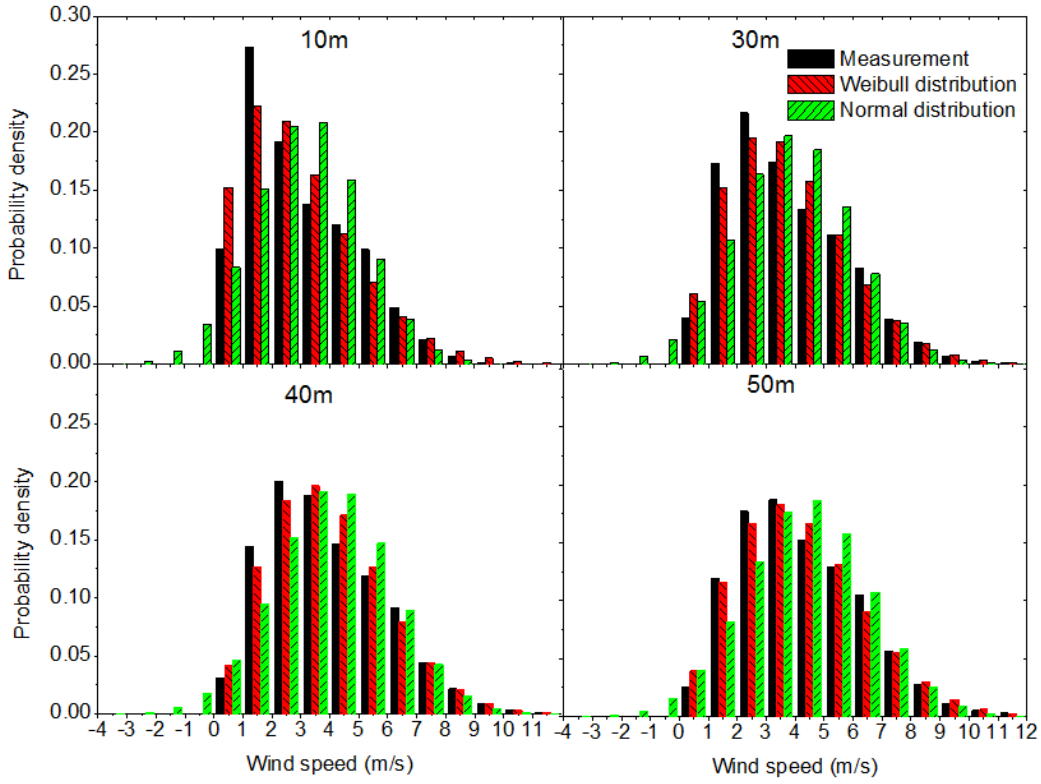

Figure 3. 9 Comparison of measured and calculated (Weibull) wind speed probability

3.5 HAWT power generation assessment

Two categories of HAWT are assessed in the Masdar wind conditions, the large size Nordtank 500/41 and the small size Windspot. The main technical specifications of

the two are given in Table 3.1. The measured power curves of the two are shown in Figure 3.10.

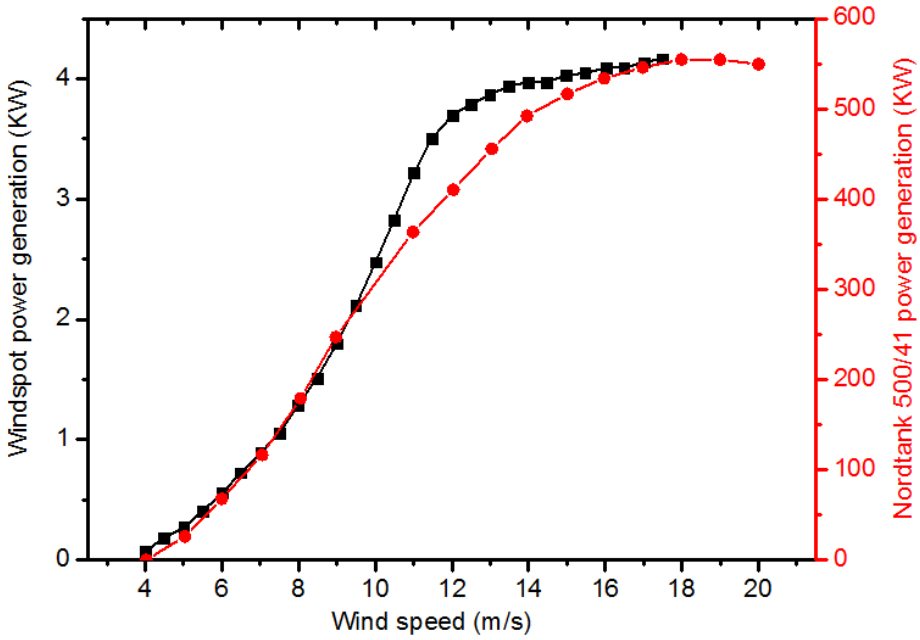

Figure 3. 10 The power curve of Nordtank 500/41 and 3.5KW Windspot

Combining power curves of Figure 3.10 and Weibull probability density distribution of Figure 3.8, the annual power generation and capacity factors of Nordtank 500/41 and 3.5KW Windpot under different heights were obtained and summarized in Table 3.4. It is clearly shown from the capacity factors that 3.5KW Windspot has a significant advantage over Nordtank 500/41 in the low wind power regions like Masdar City. Based on the annual power generated by Nordtank of 225.53MWh at the height of 30m, equivalent number of 100 Windspot are required. Evidently, wind farm of this size will occupy much large land than one Nordtank. Therefore, there exists a tradeoff between gain in capacity factor and loss in the real estate arose.

Table 3. 4 Annual power generation and capacity factors of Nordtank 500/41 and 3.5KW Windpot

	Annual power generation (MWh)		Capacity factor	
Height (m)	Nordtank 500/41	3.5KW Windspot	Nordtank 500/41	3.5KW Windspot
10	1438.84	16.71	3.29%	5.46%
30	2255.42	22.66	5.15%	7.39%
40	2544.01	24.80	5.81%	8.09%
50	3307.08	28.73	7.55%	9.37%

3.6 Conclusions

This work covered different aspects of cases of study for HAWT implementation at Masdar City. First, annual data was collected at different heights at different temporal resolutions. Second, the data was subjected to linear regression and spectral as well as wavelet decomposition. It was then modeled with an appropriate Weibull probability distribution. As the annual collected data categorized Masdar City as poor wind region, the Weibull distribution model is combined with two different sizes of commercial HAWT power curves. The estimated power obtained by the Nordtank 500/41 at the height of 30m is equivalent to the power obtained from approximately a hundred of 3.5KW Windspots at the same height in Masdar City. Based on the investment-return and without accounting for the carbon trading, results support small wind turbine implementation. However, there must be a tradeoff as the mortgage of the large land occupy by the small wind turbines may be associated with a prohibitive cost.

CHAPTER 4

Application of an Improved BEM Model on 3.5KW HAWT

4.1 Introduction

Currently, significant number of approaches, theories and models are developed to predict wind turbine performance. Although high fidelity CFD continues to be perused [69-71], it remains extremely costly as far as computational resources, analysis time, and required expertise. Amongst lower fidelity approaches, methods and models, Blade Element Momentum (BEM) method is the oldest and remains to be the most widely used method for predicting wind turbine performance. It was originally developed by Glauert [72] who combined blade element theory and momentum theory to analyze the airplane propeller performance. Blade element theory assumes that blades can be divided into multiple elements, which can act independently as two-dimensional airfoils. The forces and moments can be calculated

separately then summed to obtain the overall blades forces and moments. The other half of BEM method, the momentum theory, assumes that wind turbine harvests energy from incoming flow, thereby, the flow is subjected to pressure and moment losses. Using momentum theory, induced velocities from the momentum loss can be calculated. These induced velocities can affect the flow over blades and the forces on them.

In practice, corrections need to be introduced such that BEM method can be applicable in wind turbine design. The corrections include Tip loss correction[12], Hub loss correction [13], Glauert correction [14], Skewed wake correction [15] and rotational correction of [16]. Tip loss correction accounts for the influence made by vortex shedding from the blade tips into the wake. Hub loss correction accounts for the vortex shed near the hub. Glauert correction accounts for the turbulent wake phenomenon. Skewed wake correction accounts for the influence made by wind turbine operating at yaw angles, while rotational correction accounts for the lift augmentation caused by rotation.

4.2 Mathematical Formulation

4.2.1 Momentum theory

Axial momentum and Betz limit

Let us consider the stream tube around a wind turbine as shown in Figure 4.1. The flow crosses the ends of the stream tube and the turbine is represented by a uniform “actuator disc” and creates a discontinuity of pressure within the stream tube at the turbine location.

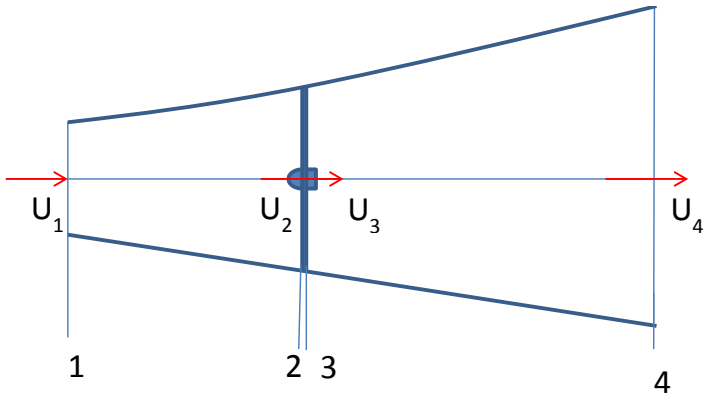

Figure 4. 1 Axial stream tube around a Wind Turbine

Four positions shown in the figure are, at the upstream of the turbine (1); just before the blades (2); just after the blades (3) and downstream of the blades (4). Energy is extracted from the wind between the two positions (3) and (4) which results in a total pressure drop. Since no work is done on either side of the turbine rotor, thus the Bernouli's equation can be used in both control volumes, as shown below:

$$p_1 + \frac{1}{2}\rho U_1^2 = p_2 + \frac{1}{2}\rho U_2^2 \tag{4.1}$$

$$p_3 + \frac{1}{2}\rho U_3^2 = p_4 + \frac{1}{2}\rho U_4^2 \tag{4.2}$$

As we assume $p_1 = p_4$ and $U_2 = U_3$, the thrust can be expressed as:

$$dT = (p_2 - p_3)dA, \text{ thus } dT = \frac{1}{2}\rho(U_1^2 - U_4^2)dA \tag{4.3}$$

Where, the area at the disc A_2 is replaced by A. By realizing that the thrust also equals to the rate of change of momentum of the air stream, as expressed below:

$$T = \dot{m}(U_1 - U_4) \tag{4.4}$$

Mass flow rate can be related to the velocity at the disc by $\dot{m} = \rho A_2 U_2$, by equating the thrust from equations (4.3) and (4.4), one obtain:

$$U_2 = \frac{U_1 + U_4}{2} \tag{4.5}$$

Here define the axial induction factor as:

$$a = \frac{U_1 - U_2}{U_1} \tag{4.6}$$

And dA can be written as $2\pi r dr$, where r is the radius of the disc. The thrust can be rewritten as:

$$dT = \rho U^2 4a(1-a)\pi r dr \tag{4.7}$$

Where free stream velocity U_1 is replaced by U. The power output P, is equal to the thrust times the velocity at the disc as expressed below:

$$P = \frac{1}{2}\rho(U_1^2 - U_4^2)AU_2 \tag{4.8}$$

By substituting U_4 and U_2 with U_1 and a, one obtain:

$$P = \frac{1}{2}\rho U^3 4a(1-a)^2 \tag{4.9}$$

Wind turbine rotor performance is often characterized by its power coefficient, C_P:

$$C_P = \frac{\text{Rotor Power}}{\text{Power in the wind}} = \frac{P}{\frac{1}{2}\rho U^3} \tag{4.10}$$

By comparing equations (4.9) and (4.10), the power coefficient for Wind Turbine is $C_P = 4a(1-a)^2$, the maximum C_P is determined by taking the derivative of the power coefficient with respect to a and setting it equal to zero, yielding $a = {}^1/_3$ and resulting in the maximum power coefficient $C_P = {}^{16}/_{27}$, which is known as the Betz limit. Betz limit defines the maximum possible rotor power coefficient; it cannot be surpassed or even reached in practice due to the three main reasons as listed below.

- The rotation of the wake behind the rotor.

- Finite number of blades and associated tip losses.
- Non-zero aerodynamic drag.

Angular momentum

In the previous analysis using linear/axial momentum theory, it was assumed that no rotation was imparted to the flow. However, in reality, the rotation of wind turbine results in a rotational wake, which reduce the energy extraction from the wind than expected. Meanwhile, the analysis of the annular stream tube, as shown in Figure 4.2, can be related to the rotor torque.

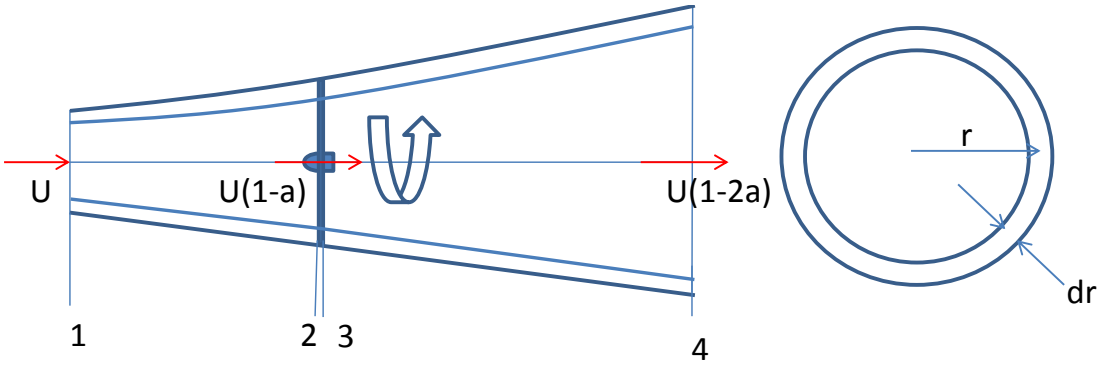

Figure 4. 2 Rotating annular stream tube

Thus for a small element the corresponding torque will be:

$$dQ = \omega^2 r d\dot{m} \tag{4.11}$$

Where ω is the angular speed of the wake. For the rotating annular element, $d\dot{m} = 2\pi r\rho U(1-a)dr$, and define the angular induction factor a' by:

$$a' = \frac{\omega}{2\Omega} \tag{4.12}$$

Where Ω is the angular speed of the wind turbine. One can then obtain the expression for the torque, as shown below:

$$dQ = 4a'(1-a)\rho U\pi r^3\omega dr \tag{4.13}$$

Where ρ is the air density, U is the mean air flow velocity, r is the local blade radius, ω is the blade angular rotational speed.

4.2.2 Blade element theory

The forces on the blades of a wind turbine can also be expressed as a function of lift and drag coefficient and the angle of attack. As shown in Figure 4.3 that the blade is assumed to be divided into N sections/elements, and the forces are calculated element by element and summed up to obtain the overall forces on the blade.

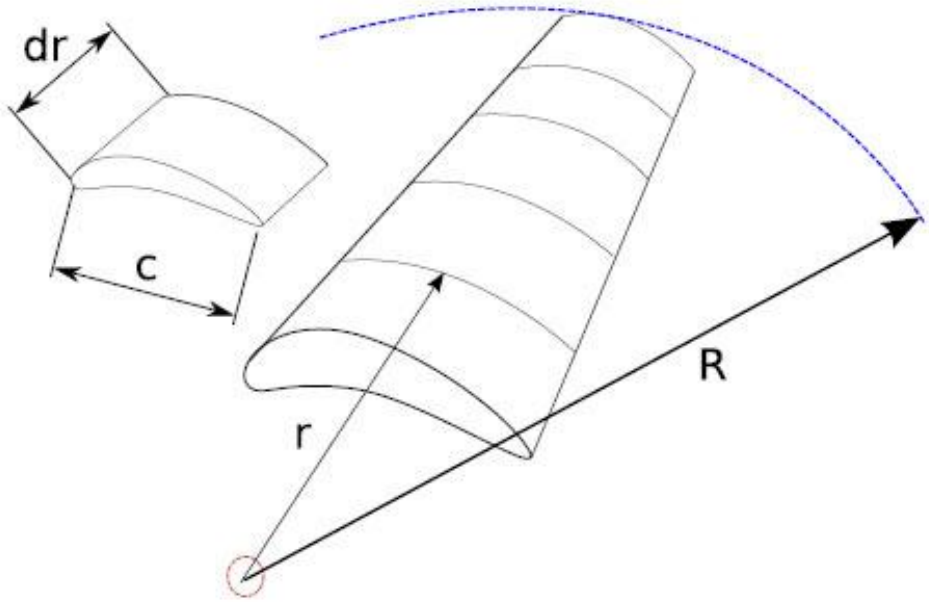

Figure 4. 3 The blade element model

It is further assumed in the theory that there is no aerodynamic interaction between the blade elements, that is, radial flow is ignored; also the forces on the blades are determined solely by the characteristic of the airfoil implemented in the blades. Figure 4.4 shows the illustration of flow over the element.

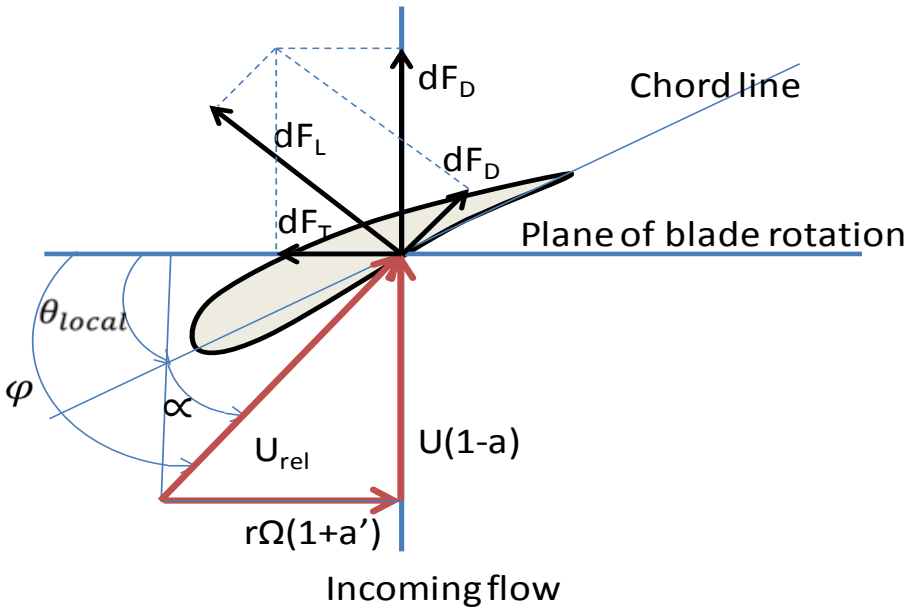

Figure 4. 4 Illustration of flow over the element

The thrust and the torque, here are noted as dF_T and dF_N, can be determined as follows:

$$dF_T = dF_L\cos\varphi + dF_D\sin\varphi \tag{4.14}$$

$$dF_N = dF_L\sin\varphi - dF_D\cos\varphi \tag{4.15}$$

Where $dF_L = C_l\frac{1}{2}\rho U_{rel}^2 cdr$, $dF_D = C_d\frac{1}{2}\rho U_{rel}^2 cdr$, φ is the angle of relative wind, U_{rel} is the relative wind speed, C_l and C_d are the lift and drag coefficients, respectively.

As a result, one can obtain:

$$dT = \sigma'\pi\rho\frac{U^2(1-a)^2}{\sin^2\varphi}(C_l\cos\varphi + C_d\sin\varphi)rdr \tag{4.16}$$

$$dQ = \sigma'\pi\rho\frac{U^2(1-a)^2}{\sin^2\varphi}(C_l\sin\varphi - C_d\cos\varphi)r^2dr \tag{4.17}$$

Where σ' is the local solidity which can be calculated by $\sigma' = Bc/2\pi r$; Here B is the number of blades and c is the local blade chord length, φ is the angle of relative wind, C_l and C_d are the lift and drag coefficients, respectively.

Thus the torque at the shaft (Q^*) is the summation of dQ for all the blades elements, and the wind turbine power is given by $P = Q^*\omega$. Eventually, the wind turbine power prediction lies in solving the axial induction factor a and the tangential induction factor a' [73]. By combining equations (4.7), (4.13), (4.16) and (4.17), one can solve the induction factors a and a' as given below:

$$a = \frac{1}{1 + \frac{4\sin^2\varphi}{\sigma'(C_l\cos\varphi + C_d\sin\varphi)}} \tag{4.18}$$

$$a' = \frac{C_l\sin\varphi - C_d\cos\varphi}{(C_l\cos\varphi + C_d\sin\varphi)\lambda_s + \frac{4\lambda_s\sin^2\varphi}{\sigma'}} \text{ or } a' = a\frac{C_l\sin\varphi - C_d\cos\varphi}{(C_l\cos\varphi + C_d\sin\varphi)\lambda_s} \tag{4.19}$$

Where λ_s is the local speed ratio which is defined as $\lambda_s = \omega r/U$. The axial thrust coefficient C_T is expressed as:

$$C_T = \frac{\sigma'(1-a)^2(C_l\cos\varphi + C_d\sin\varphi)}{\sin^2\varphi} \text{ or } C_T = 4a(1-a) \tag{4.20}$$

By substituting the two induction factors into equation (4.14) the wind turbine performance can be assessed.

4.3 Corrections for BEM method

When the BEM method was originally developed by Glauert, it was far from giving accurate and reliable results before the implementation of several correction factors. These include Tip and Hub Loss, Glauert and Buhl empirical corrections, as well as the "3D correction" of Snel et al. and the Skewed wake correction.

4.3.1 Tip and hub loss

Tip and hub losses consider the influence of vortices shed from tip and hub, which plays an important role in the induced velocity distribution at the rotor. Prandtl model is the most widely used model for calculating the tip and hub loss correction factors. An approximate formula for the Prandtl tip and hub function was firstly introduced by Glauert [72] as expressed below:

$$F = \frac{\pi}{2}\cos^{-1}(\exp(-f)) \tag{4.21}$$

Where $f = \frac{B(R-r)}{2\, r \sin\varphi}$ is for tip loss factor, and $f = \frac{B(r-R_{hub})}{2\, r \sin\varphi}$ is for hub loss factor, where R is the radius of blade tip and R_{hub} is the radius of blade hub.

Ultimately, the correction factor can be calculated by the multiple of the tip and hub loss correction factors, as illustrated in equation (4.22):

$$F = F_{tip}F_{hub} \tag{4.22}$$

Figure 4.5 shows the relationship between thrust coefficient and axial induction factor at $F \leq 1$ and for with and without tip and hub correction factors. A pronounced increase in the axial thrust is observed with the deviation of F from unity.

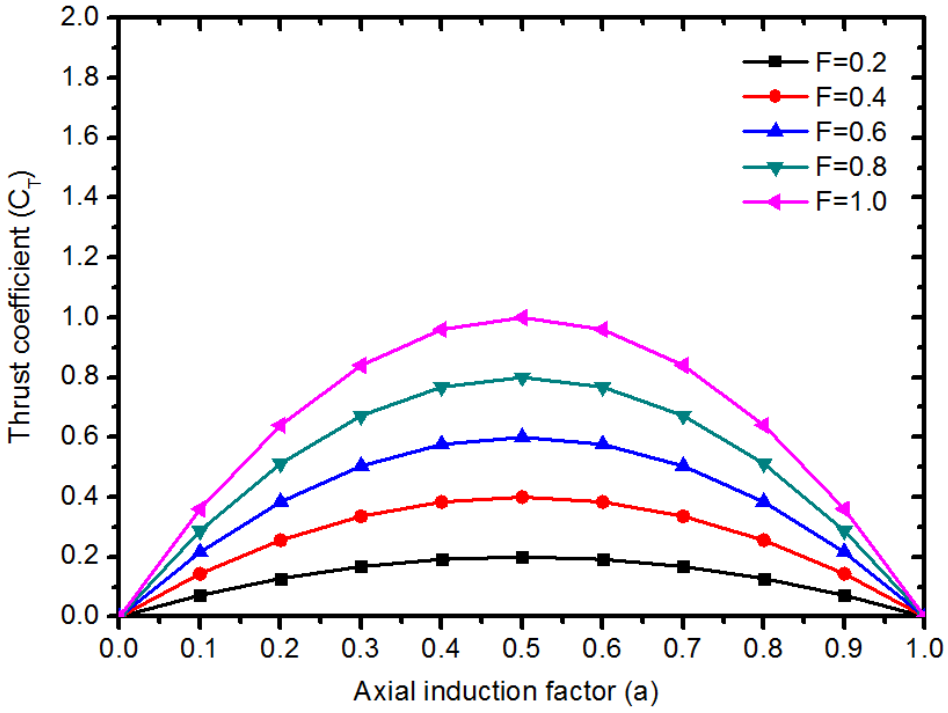

Figure 4. 5 Classical a-C_T curve under different F values

Due to the influence of the tip and hub correction factors, the forces derived from momentum theory have to be modified accordingly:

$$dT = F\rho U^2 4a(1-a)\pi r dr \tag{4.23}$$

$$dQ = 4Fa'(1-a)\rho U\pi r^3 \omega dr \tag{4.24}$$

Thus, the calculations for two induction factors and thrust coefficients are updated as follows:

$$a = \frac{1}{1+\frac{4F\sin^2\varphi}{\sigma'(C_l\cos\varphi + C_d\sin\varphi)}} \tag{4.25}$$

$$a' = \frac{C_l\sin\varphi - C_d\cos\varphi}{(C_l\cos\varphi + C_d\sin\varphi)\lambda_s + \frac{4\lambda_s F\sin^2\varphi}{\sigma'}} \text{ or } a' = a\frac{C_l\sin\varphi - C_d\cos\varphi}{(C_l\cos\varphi + C_d\sin\varphi)\lambda_s} \tag{4.26}$$

$$C_T = \frac{\sigma'(1-a)^2(C_l\cos\varphi + C_d\sin\varphi)}{\sin^2\varphi} \text{ or } C_T = 4Fa(1-a) \tag{4.27}$$

4.3.2 Glauert correction and Buhl empirical corrections

As the induction factor is greater than 0.4, wind turbines will be under a turbulence wake. This puts an upper limit for the validity of the basic theory. Glauert developed a correction [74] to the rotor thrust coefficient based on experimental measurements of helicopter rotors with large induced velocities. Buhl [75] later developed a new relation between rotor thrust coefficient and induction factor which solved the instability caused by applying Glauert correction as illustrated below:

$$a = \frac{18F-20-3\sqrt{C_T(50-36F)+12F(3F-4)}}{36F-50} \text{ for } C_T \geq 0.96 \quad (4.28)$$

Figure 4.6 shows the Classical relationship between thrust coefficient and axial induction factor, Glauert correction relationship, Buhl empirical correction relationship and experimental data of Moriarty et al. [13].

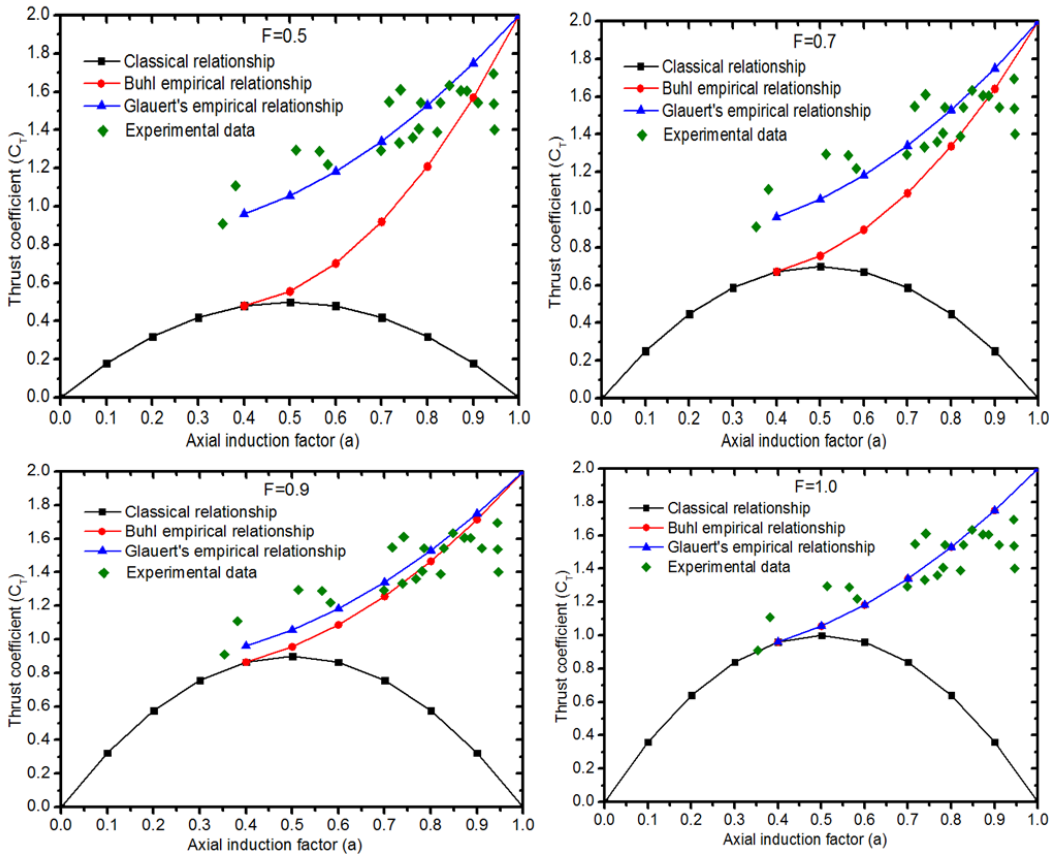

Figure 4. 6 a-C_T plots under different models when F=0.5, 0.7, 0.9 and 1.0

The wide spread experimental data indicates that the thrust coefficient is not a simple function of axial induction factor in the turbulent wake region. As clearly shown from Figure 4.6, the Buhl empirical relationship between C_T and a plausibly follows the experimental data trend, and could also solve the instability/mismatch problem caused by Glauert's empirical relationship at the same time.

4.3.3 Skewed wake correction

BEM method was originally proposed to solve for the axisymmetric flow, however, wind turbines are often running at yaw angles. This again invalidates the basic theory unless a correction is introduced accounting for the skewed effect. Snel and Schepers [17] derived the following correction formulation:

$$a_{skew} = a(1 + \frac{15\pi}{32}\frac{r}{R}\tan\frac{\chi}{2}\cos\psi) \tag{4.29}$$

Where χ is the wake skew angle, ψ is the azimuth angle. However, Eggers's work [76] concluded that the correction is too large at some situations which reveals its limitation.

4.3.4 Rotational effect

The effects of rotation were first investigated intensively for helicopter rotors. Later, the fact that aerodynamic power tends to exceed the design value for wind turbine starts attracting attention. The effect may include centrifugal pumping effect, stall delay, rotational augmentation, etc. Even though several corrections have been developed to predict the rotational effect, challenge still remains.

Followed by the conclusion made by Lindenburg [77] that the "3D correction" of Snel et al. fits reasonably, the correction is further incorporated in our work. "3D correction" of Snel et al. gives an increase of the aerodynamic lift coefficient for the effects of rotation, which is described below:

$$c_{l,rot} = c_{l,non-rot} + 3.1 \times \left(\lambda_s^2 / 1+\lambda_s^2\right) \times (c/r)^2 \times (c_{l,pot} - c_{l,non-rot}) \quad (4.30)$$

Where $c_{l,non-rot}$ is defined as $2\pi\sin(\propto -\propto_0)$, $\propto_0$ is the angle of attack when lift coefficient is zero.

Summarizing, the above mathematical formulation propose an iteration procedure for solving the axial and tangential induction factors accounting for different types of losses. As obtaining the two induction factors is indispensable for predicting the performance of wind turbines, Figure 4.7 illustrates the flow sheet for computing these induction factors.

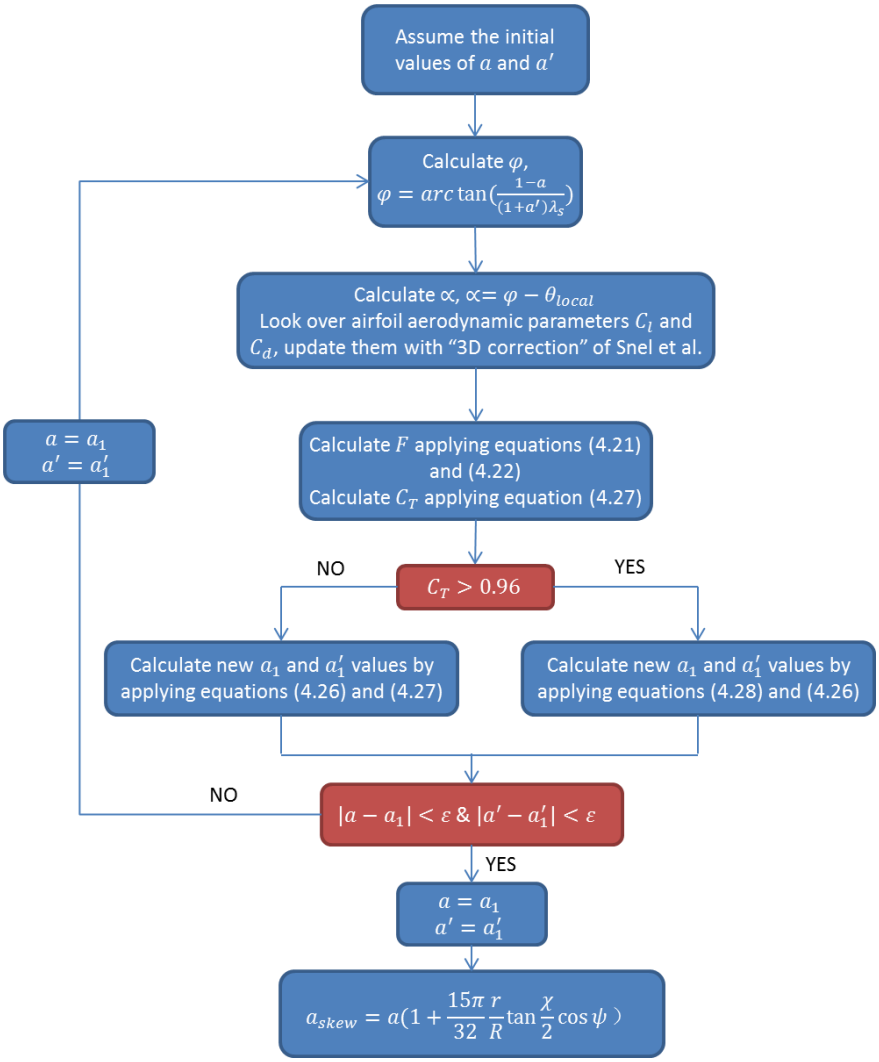

Figure 4. 7 Calculation flow sheet for induction factors

The iterative induction factor error/tolerance (ε) is set to be 0.001. The procedures are integrated to classical BEM method calculation leading to the development of robust numerical procedures, i.e. extended BEM. The code follows the iteration procedure shown in Figure 4.7. It provides the wind turbine power generation/coefficient as an ultimate result.

4.4 Verification of the extended BEM model

The UAE phase-VI turbine [78] is used as a baseline to validate the proposed extended BEM model. Its experimental data were collected by National Renewable Energy Laboratory (NREL) in the 24×36m wind tunnel of NASA Ames.

UAE phase-VI turbine is a 2-bladed and S809 airfoil type wind turbine with fixed operation state of 72RMP rotational speed and 3° pitch angle. The blades have a literal sweeping chord length of 0.737m which decreases to 0.305m and twist angle of 20.04° degrees at the largest chord [77] that fade -2.50° at the tip, as depicted in Figure 4.8.

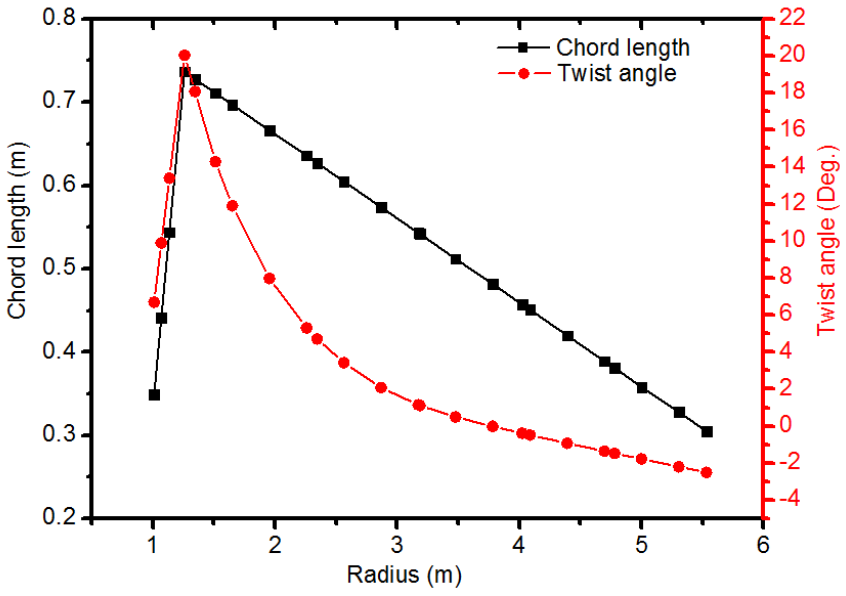

Figure 4. 8 Chord length and Twist angle over blade

The code user provides the following data: i) sectional pitch angle, ii) twist angle, iii) chord length at different radii, and iv) the lift and drag coefficients as a function of angle of attack. The aerodynamic data for S809 airfoil were taken from [77, 79]. The airfoil aerodynamic data, as shown in Figure 4.9, was initially developed at TU-Delft wind tunnel and subjected to the angle-of-attack shift technique for large angles of attack and empirical tool "Stall Coefficients (StC)" for deep stall [77].

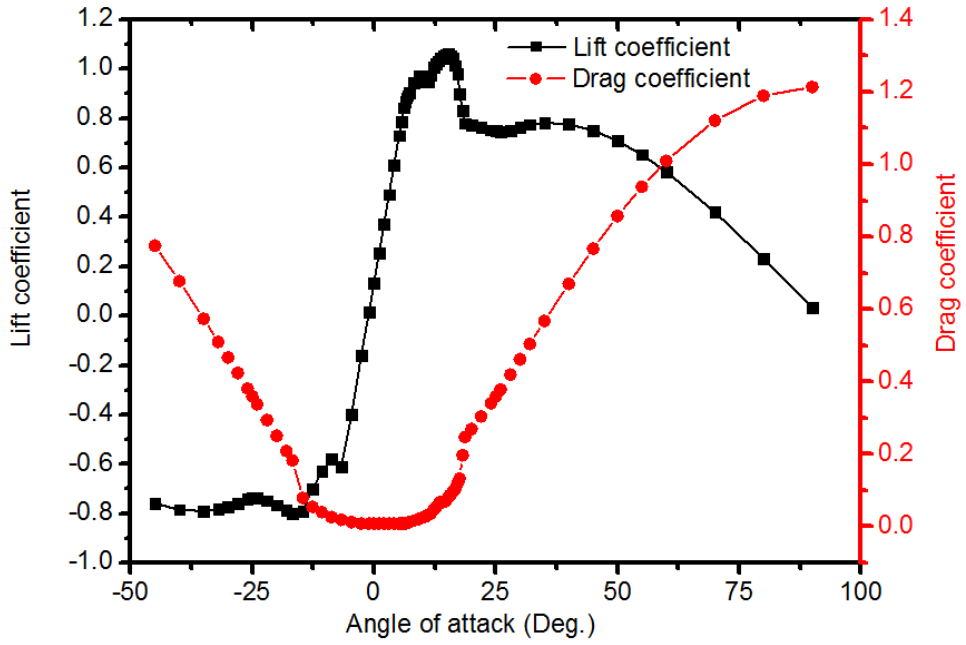

Figure 4. 9 Lift and drag coefficients under different angles of attack [77]

The influence of the different correction factors on the power coefficients of the turbine under different wind speeds were sought and compared with experimental data, as shown in Figure 4.10.

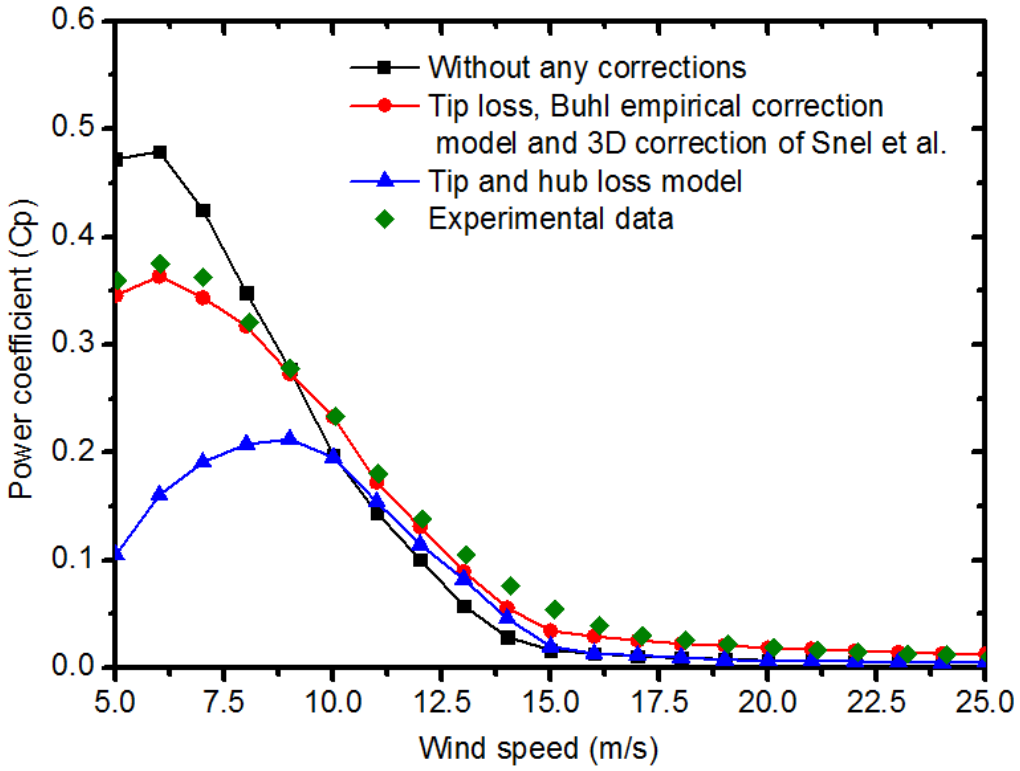

Figure 4. 10 Power coefficients under different models

It is clear from Figure 4.10 that the power coefficients obtained from BEM without any corrections overestimate the performance, while with Tip and hub corrections it reduces it at large margin. Simultaneously, the model with tip loss, Buhl empirical correction and "3D correction" of Snel et al. managed to predict the power coefficients under different wind speeds. However, the discrepancies between the results obtained from the model with Tip loss and Buhl empirical correction and the experimental data can still be observed. Even though results obtained from the model strictly follow the experimental data, but overall slightly underestimates the turbine performance. This is attributed to two reasons: i) Empirical correction of the tip loss and Buhl that require further improvements in order to describe wind turbine and incoming wind interaction, ii) Lack of accuracy in the airfoil aerodynamic data that account for the rotation effect, even though "3D correction" of Snel et al. is included.

4.5 Application of BEM to 3.5KW HAWT

Windspot is a small size HAWT, 3.5KW, three-bladed with 4.05m rotor diameter. It is characterized with low cut-in speed (<3m/s) and reaches its rated power at 12m/s. It can be fitted with different set of blades, essentially at zero twist angle with a centrifugal/active pitch control system. The chord length is 0.254m at the root, decreases linearly to 0.156m at the blade tip.

4.5.1 Aerodynamic data

The Windspot airfoil was extracted from 3D model which was transferred as International Graphics Exchange Specification (IGES) file. Panel method (governed by potential flow) and high fidelity CFD numerical simulations were developed and carried out to obtain the BEM required aerodynamic lift (C_l) and drag (C_d) coefficients at varying angle of attack ($\propto$). Figure 4.11 shows the geometry of the airfoil, in which the nodes are the captured points dividing the airfoil into panels. The trailing and leading edges are further refined with additional panels.

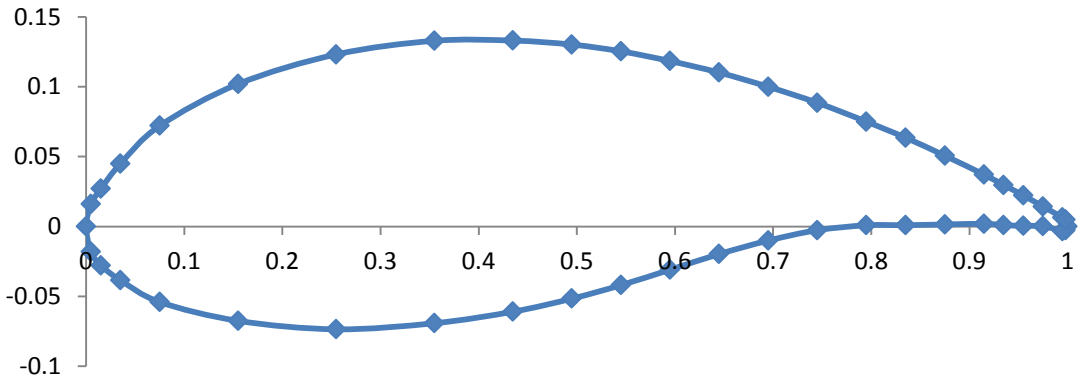

Figure 4. 11 Airfoil shape of Windspot

Figure 4.12 show the (C_l) result of panel method which clearly vary linearly with the angle of attack ($\propto$). The panel solution is based on potential flow theory with no

reference to the viscous boundary layer. These results, and when incorporated zero viscous drag, clearly will overestimate wind turbine performance.

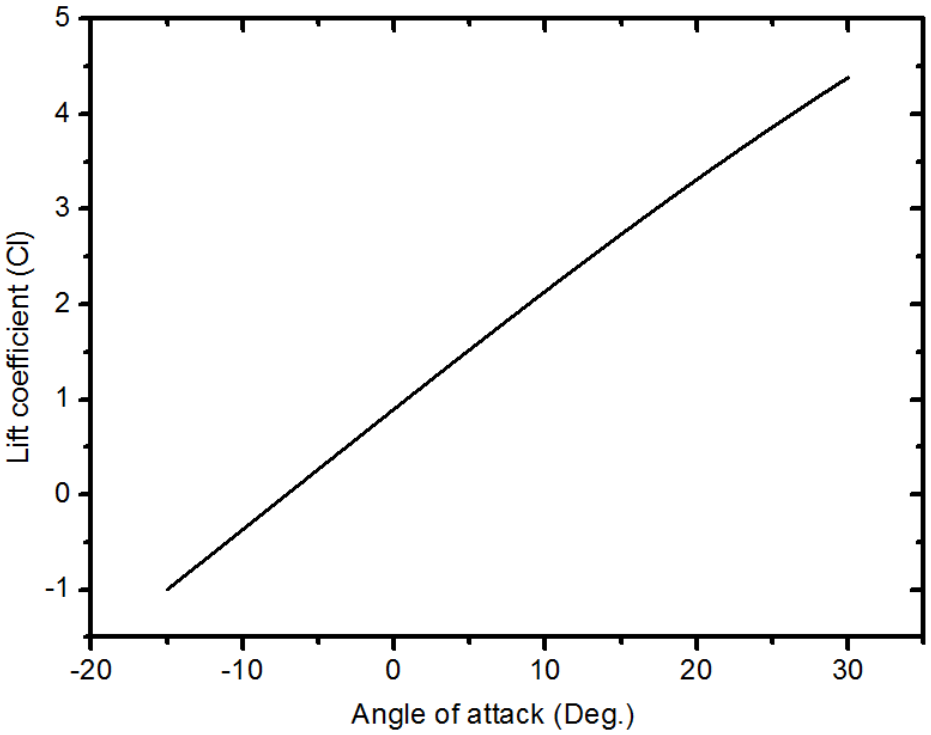

Figure 4. 12 Results of the Lift coefficient (CL) from Panel method

High fidelity CFD simulation is also carried out for the Windspot airfoil. The flow is governed by the two dimensional, steady incompressible Navier–Stokes equations. These equations represent statements of mass and momentum conservation and are written after applying the scalar variable expansion Øi ($\vec{x}$,t) = $\overline{Ø}_i(\vec{x},t)$ + Øi′ ($\vec{x}$,t) and ensemble (over bar) averaging as:

$$\text{Continuity: } \frac{\partial \bar{\rho}}{\partial t} + \frac{\partial \overline{\rho u_i}}{\partial x_i} = 0 \tag{4.31}$$

$$\text{Momentum: } \frac{\partial \overline{\rho u_i}}{\partial t} + \frac{\partial}{\partial x_j}(\rho \bar{u}_j \bar{u}_i) = \frac{\partial \tau_{ij}}{\partial x_j} + \bar{\rho} g_i \tag{4.32}$$

$$\text{Constitutive: } \tau_{ij} = -\bar{p}\delta_{ij} + \mu\left(\frac{\partial \overline{\rho u_i}}{\partial x_j} + \frac{\partial \overline{\rho u_j}}{\partial x_i}\right) - \overline{\rho u_i' u_j'} \tag{4.33}$$

where t is the time advancement, x_i is the Cartesian coordinate (i= 1, 2), u_i is the velocity component in x_i direction, ρ is the density, g_i is the gravitational acceleration component in x_i direction, τ_{ij} is the stress tensor components, p is the pressure, μ is the molecular viscosity, u_i' is the velocity fluctuations about ensemble average velocities. The $\overline{u_i'u_j'}$ term is the Reynolds stresses and is modeled utilizing the mean ($\bar{u}$) velocity via the common eddy viscosity k-epsilon turbulent. It is expressed as:

$$\text{Turbulence closure: } -\overline{\rho u_i' u_j'} = \mu_t \left(\frac{\partial \overline{\rho u_i}}{\partial x_j} + \frac{\partial \overline{\rho u_j}}{\partial x_i} \right) - \frac{2}{3} \bar{\rho} k \delta_{ij} \tag{4.34}$$

Where k is the kinetic energy ($\overline{u_k' u_k'}$) and μ_t is the turbulent viscosity which links k and turbulent dissipation rate such that $\mu_t = f_\mu \frac{C_\mu \rho k^2}{\varepsilon}$, where f_μ and C_μ are empirical constants. Substituting Eq. (4.34) to (4.33) conveniently allows summing the Reynolds stresses terms to the diffusion term (2nd right hand term in Eq. (4.34)) with an equivalent viscosity $\mu_{equ} = \mu + \mu_t$. Therefore, closure of the above system is achieved with the integration of two additional transport equations for k and ε. The above equations are discretized on well posed/bounded domain forming an algebraic system of equations. The boundary conditions including incoming velocity (Dirichlet), side boundaries symmetry (Neumann), outflow at the exit, and no-penetration, no-slip at the airfoil surface.

The airfoil geometry and the flow zone model were built and discretized using quad type cells. The airfoil surface is padded with a refined cell cluster of less than 0.01% chord length initial height and at smooth growth of 1.4 to achieve one unit normalized wall distance (y^+=1). The geometry, the baseline mesh, and the imposed boundary conditions are shown in Figure 4.13. The domain subjected to upstream uniform velocity (5m/s which is the annual average wind speed in Masdar City [60]) and

output atmospheric pressure to be used during the iteration in the event of recirculation at the outflow boundary.

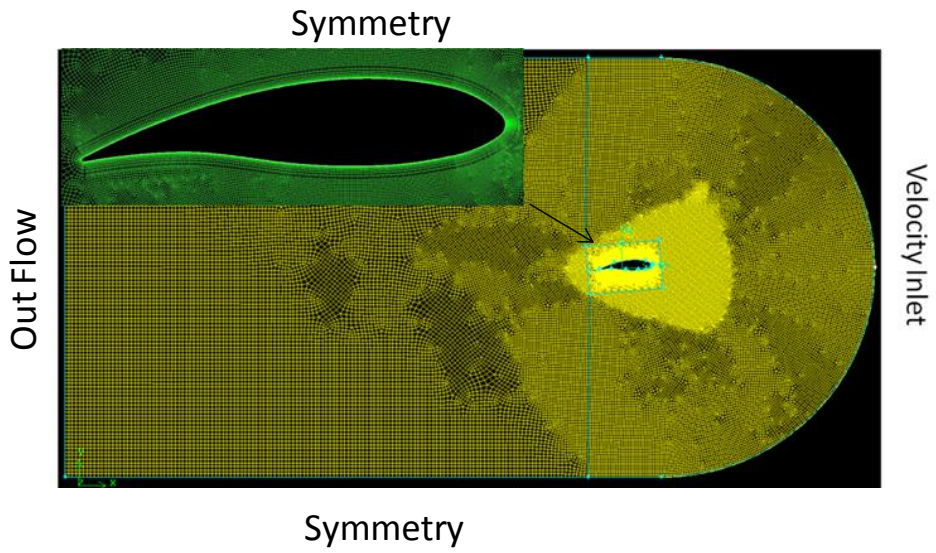

Figure 4. 13 The meshed airfoil geometry

The Fluent iterative, double precision, pressure based, SIMPLE solver are used to compute the aerodynamic data as a function of angle of attack with as low as 10^{-10} residuals in the continuity and the two momentum equations. Mesh sensitivity studies were carried out first to assess the discretization error. Results of the 5 degrees angle of attack case is carried out at the baseline, fine and two levels of coarseness, and these are summarized in Table 4.1.

Table 4. 1 Lift and Drag coefficients and their relative errors under different mesh resolution (element count and Maximum y+)

Level	Element Count	C_l	C_d	C_l R. E.	C_d R. E.	Max y+
Fine	204786	0.717	0.0621	--	--	0.768
Baseline	67446	0.721	0.0620	0.56%	0.16%	1.534
Coarse	33208	0.722	0.0623	0.7%	0.32%	5.332
V. Coarse	19294	0.7337	0.0619	2.33%	0.32%	5.526

The mesh dependence of the solution observed to reduce as it becomes finer. The baseline mesh appears to capture the solution at a reasonable level of accuracy relative to the other successive refinement and coarseness. This is also clear from the normalized value of the wall distance (y+) that it is desired to be unit one to avoid excessive and unnecessary refinement. Figure 4.14 shows the results of the lift and drag coefficients as function of the angle of attack for the 3.5KW Windspot airfoil from baseline mesh.

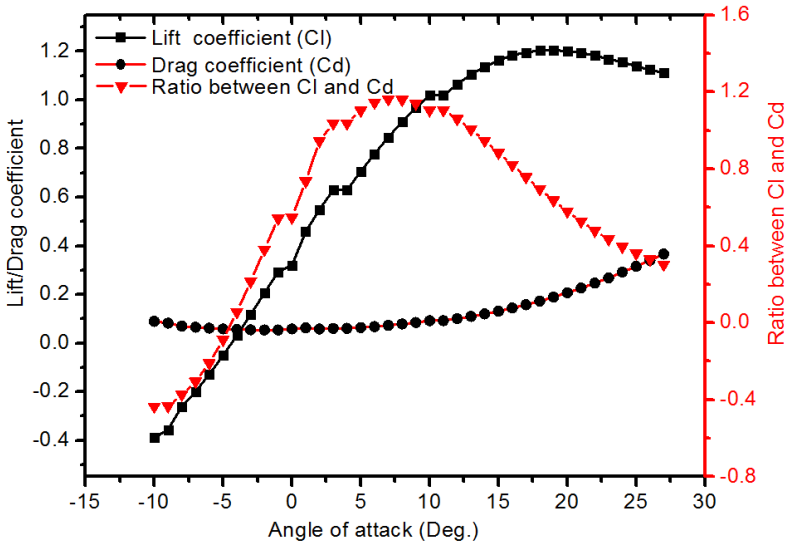

Figure 4. 14 CFD results of the Lift and drag coefficient as a function of angle of attack

4.5.2 Performance estimation

The improved BEM is used to estimate the Windspot power coefficient of which is limited by Betz law (<0.59) [80]. As the operation condition of the wind turbine is unknown, it is reasonably assumed to operate at a fixed rotational speed of 12 rad/s and 7 degrees pitch angle. The power coefficients under different wind speeds, yet at that fixed rotational speed, are obtained and compared to experimental data [81] as depicted in Figure 4.15. Results of the simulation shows appreciable deviation from those obtained experimentally, while continue to exhibit a plausible trend.

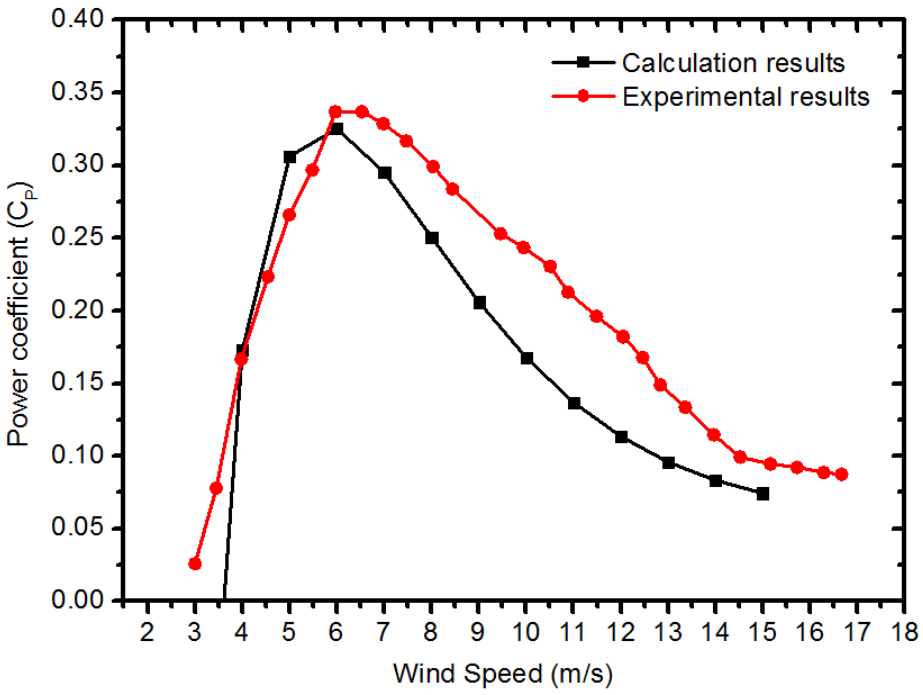

Figure 4. 15 Power coefficients under different wind speeds

The influence of the Pitch angle, twist angle, and TSR are also investigated. Figure 4.16 shows the effect of different Pitch angles at zero twist at the previously considered rotational speed (12rad/s). A Pitch angle in the range of {3,7} appears to be more optimal for a flow speed up to 8m/s. Figure 4.17 depicts the influence of the twist and clearly shows a 10˚ degrees twist can lead to a measurable increase in the

power coefficient. Higher twist resulted in near stall condition and drastic fall in the power coefficients. The influence of the tip speed ratio is also investigated at the optimal Pitch and Twist angles to observe their combined effect on the power coefficient. The tip speed is varying here by the rotational speed. The results suggest a maximum power can be obtained near TSR of 4.

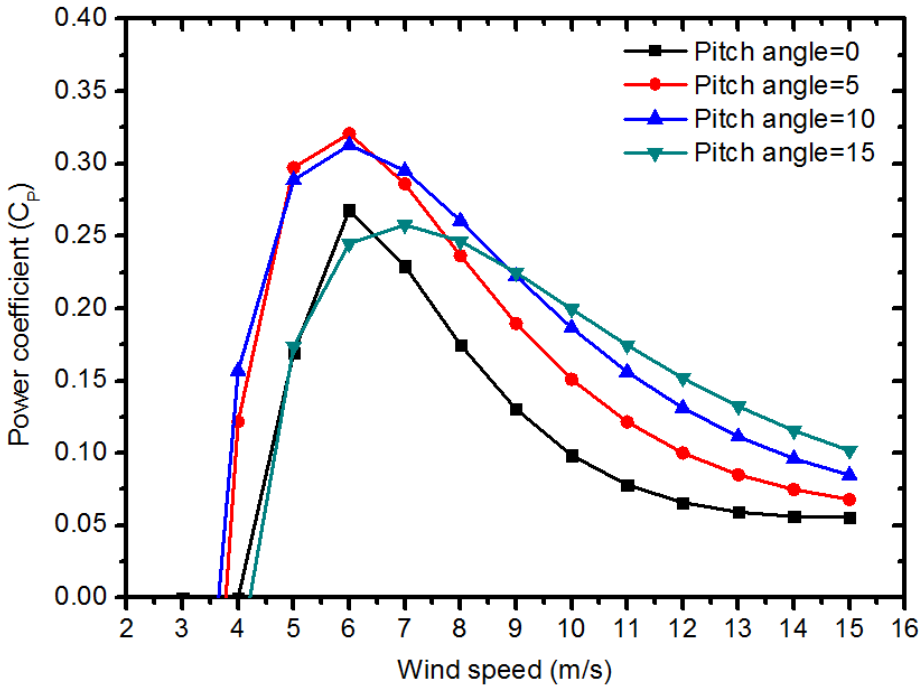

Figure 4. 16 Power coefficients under different pitch angles

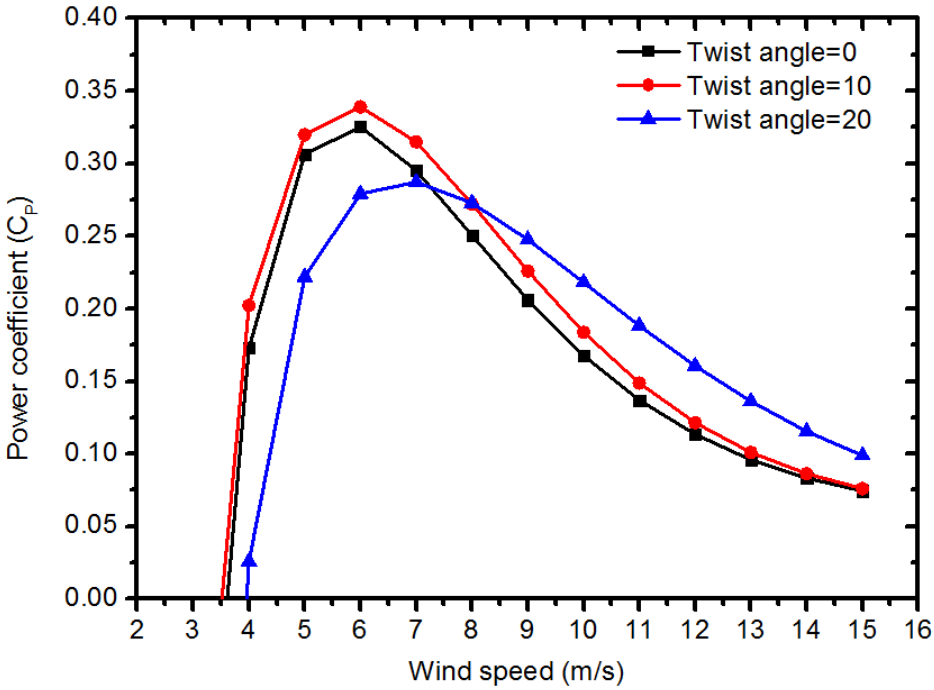

Figure 4. 17 Power coefficients under different blade twist angles

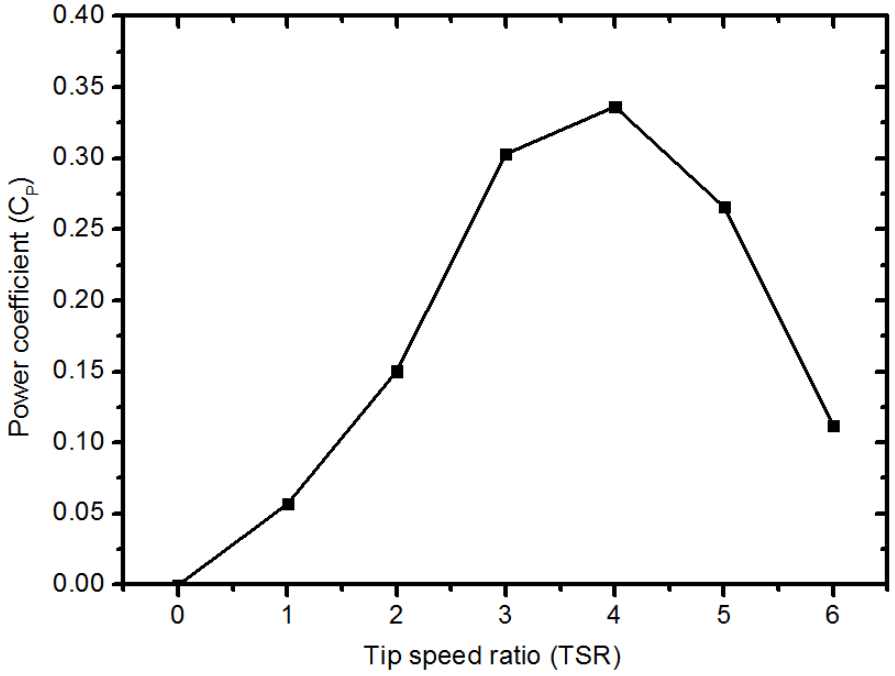

Figure 4. 18 Power coefficients under different TSRs

Table 4.2 was made in order to clarify the operation conditions used in the previous twist angle, pitch angle, and TSR studies. It is clear from Figure 4.16 and 4.17 that

choosing a proper pitch angle and designing a blade with proper twist angle are important for wind turbines. Excessive choice of pitch angle combined with twist would also lower the harvested wind turbine energy. Figure 4.18 shows that TSR as another important parameter for wind turbine and higher power coefficients is achieved by operating at a suitable TSR value.

Table 4. 2 Wind turbine operation conditions for Figure 4.16, 4.17 and 4.18

Figure number	Operation condition
4.16	Fixed rotation speed 12rad/s, no twisting of the blades, different pitch angles
4.17	Fixed rotation speed 12rad/s, blade twisted 10 degrees at the root and decrease to 0 degree at the tip, fixed 7 degrees pitch angle
4.18	Fixed wind speed 5m/s, blade twisted 10 degrees at the root and decrease to 0 degree at the tip, fixed 7 degrees pitch angle

4.6 Conclusion

An improved BEM code for HAWT is developed. It incorporated four different corrections, i.e. Tip loss, Buhl empirical correction, Skewed wake, as well as the "3D correction" of Snel et al. These corrections extend the application of the BEM method to the turbulent wake regime of the HAWT. The results of the code were compared to those of NREL measured data of the UAE phase-VI turbine. Key success and data input for BEM is to obtain accurate aerodynamic coefficients for C_l and C_d which can't be entirely relying on the potential flow theory (Panel method). As wind turbine airfoil shapes depart from classical NACA series, high fidelity CFD analysis is necessary. Following high fidelity analysis to the three-bladed Windspot 3.5KW airfoil, the updated BEM shows a plausibly match with the experimental trend following the incorporation of the correction factors. The performance of Windspot is

assessed by considering the effect of the twist angle, pitch angle and TSR. The code illustrated these effects and results show designing blades with proper twist angle that harmonized with suitable TSR and pitch angle can definitely lead to substantial gain in performance.

CHAPTER 5

3D RANS simulation study of 3.5KW Windspot

5.1 Introduction

The world possesses great wind energy potential. Onshore wind energy potential was estimated to be 96 PWh per year [4] in1004, representing 6 to 7 times the of the total globe electricity consumption in 2001. Enormous interest (30% annual growth) has been shown in wind turbine deployment and wind energy utilization. Vast potential for wind power development in Asia, Latin America, Africa and the Middle East was assessed and lead to the development of wind atlas by Global Wind Energy Council (GWEC) [82].

Today, industrial design codes for wind turbines are still based on BEM method. It was originally developed by Glauert [72], who combined blade element theory and momentum method together to predict the airplane propeller performance. He firstly introduced the concept that the blade can be divided into several sections which can

be treated separately like 2D airfoil and summed together to anticipate the blade performance. Later, lots of correction factors like tip loss correction [12], hub loss correction [13], Glauert correction [74], Skewed wake correction [15], and Stall-delay correction [83] were introduced to make the model applicable in the commercial world. Even now, industrial rotor design codes are mainly based on BEM method [84] due to its high efficiency and relatively accuracy. However, since BEM method assume a quasi-steady flowfield and use two dimensional aerodynamic approximations, it fails to resolve the flow with limited and empirical corrections considering for rotational effect [77]. The rotational effect, however, may cause phenomenon like stall-delay, lift augmentation, spanwise flow, and thus is crucial for accessing the wind turbine power generation and aeroelastic predictions.

Computational Fluid Dynamics (CFD) attracts more and more attention as the computational power and memory storage develops. The usage of CFD on resolving fluid flows dates back to 1953 when Kawaguti [85] obtained a solution for flow around a cylinder by using a mechanical desk calculator and working 20 hours per week for 18 months. Till today, different levels of numerical ways have been tried on wind turbine. Generalized Actuator Disc Model has been implemented to analyze the wind turbine rotor performance, which demonstrated good results in axisymmetric flow conditions by comparing with experimental results [86-88]. To overcome the limitation of axisymmetric assumption, an extended 3D actuator disc model was later developed [89].

With the CFD solvers capable of handling viscous flow on rotors, the usage on wind turbines are of practical interest. Most fluid flows of engineering interest are turbulent including flow around wind turbines. While numerous advances have been made in the numerical solution of the Navier-Stokes equations, turbulent flows still present

challenges for today's methods. Most CFD methods solve the Reynolds-Average Navier-Stokes (RANS) equations, in which only the mean flow is solved on the computational mesh, and the turbulent physics are replaced by closure models. RANS-based models include algebraic models, one equation models, e.g. Spalart-Allumaras model, two-equation models, e.g. k-episilon (k- ε) models, k-omega (k- ω) models, etc. Among which, k- ε and k- ω models are two well-known models, both of them are widely used in wind turbine simulation area. However, k- ε model has been shown to be too diffusive for wind energy applications [90]. As an improvement, the shear-stress transport (SST) k–ω model was developed by Menter [91, 92] to effectively blend the robust and accurate formulation of the k–ω model in the near-wall region with the free-stream independence of the k–ε model in the far field, which is suitable for partial stall simulation, e.g. wind turbine simulation. Another model that gives good agreement with experiments is the Reynolds stress model (RSM), which develops second-order closure relations instead of using eddy-viscosity approach. It is able to deal with anisotropic flow, but is more expensive and has rarely been used in wind energy applications.

As an alternative to the Reynolds-average methodology, LES techniques have been widely explored in the past years. Although LES gives a better physical representation of the eddy dynamics in separated flows, it is still limited for being widely used due to the requirement for high resolution mesh and intense computation effort. As the RANS equations fail to simulate massive separation, even when simulations are performed in a time-true sense, and LES are unaffordable, hybrid LES/RANS approaches, such as Detached Eddy Simulation (DES), represent an attractive compromise between computing cost and accuracy. The idea behind hybrid approaches is to combine fine-tuned RANS technology in the boundary layers, and

the simple power of LES in the separated regions. In the RANS regions, the turbulence model has full control over the solution through the eddy-viscosity based closure. In the LES region, little control is left to the model, the larger eddies are resolved both in space and time, and grid refinement directly expands the range of scales in the solution. This reduces considerably the computing costs, as compared to a full blown LES. Recently, Eric [93] just applied the hybrid RANS/LES model on the wind turbine simulation.

DNS is not a turbulence model. It is a solution of the complete time-dependent Navier-Stokes equations. This is prohibitively expensive and unaffordable especially at large Reynolds numbers as huge numbers of grid nodes would be needed to resolve all scales of motion. The biggest DNS, up to now, used 40963 mesh points and was carried out in the Japanese Earth Simulator supercomputer in 2002.

5.2 CFD overview

Fluid flow is commonly studied in three ways: experimental fluid dynamics, theoretical fluid dynamics and numerically (Computational Fluid Dynamics), among which the numerical way is emerging and becoming more important than ever due to the development of computation ability. Computational Fluid Dynamics (CFD) is the use of computers and numerical methods to solve problems involving fluid flow. Till now, CFD have been successfully applied in different areas, which include aerodynamics of cars and aircraft, hydrodynamics of ships, flow through pumps and turbines, combustion and heat transfer, chemical engineering, etc. The results obtained from CFD analyses can help, but not restricted to, conceptual studies of new designs, detailed product development, troubleshooting, redesign, etc.

The widely usage of CFD reveals its valuable advantages:

- CFD is relatively cheaper and faster

  Using physical experiments and tests to obtain essential engineering data is very costly and time-consuming, while CFD simulations are relatively inexpensive and can be executed in a short period of time. As computers are becoming more powerful, we tend to spend less money and time on obtaining engineering data from CFD.

- CFD is capable of simulating both real and ideal conditions

  CFD provides the ability to theoretically simulate any physical condition, which can be difficult to test or impossible to realize in the lab. Also it allows great controls over physical processes and simulation conditions, which help understand the flows.

- CFD gives detailed results for any purposes

  Experiments usually only permit data to be extracted at a limited number of locations, or limited time in the system, while CFD allows the analyst to exam a large number of locations in the region of interest and yields a comprehensive set of flow parameters for any research objectives.

- CFD gives a relatively accurate and reliable results

  Due to the continuous mathematical improvements of solution schemes, CFD is capable of obtaining reliable and accurate results. With the development of computation ability, CFD tend to become more reliable and accurate in simulating any physical problems.

However, one has to face the shortcomings of CFD as well. Since CFD solutions rely upon models of real world processes, there, sometimes, may exit some inaccuracies, which may include numerical error, round-off error, truncation error, etc. The accuracy of the solutions also depends on the initial/boundary conditions provided to

the model. Besides, it is generally more computationally intense compare to other analytical tools, e.g. BEM.

The numerical modeling of fluid dynamics problems requires firstly and most importantly, a precise definition of the physical phenomena. Simultaneously, all the relevant features should be indicated in a simplest, but not leading to obvious errors, way, such as geometry, mesh, materials, and boundary conditions. Nevertheless, a number of simplifications are always acceptable, and are always inevitable to model the problems properly.

5.2.1 CFD analysis procedures

Comprehensive overviews of the techniques used to solve problems in fluid dynamics on computers are given in [94-96]. A complete CFD analysis mainly consists of:

- Pre-processing

  On this stage, the physical problem is implemented into a mathematical model. It starts with defining the computation domain, which should be big enough to capture certain physical phenomena and be capable of giving reliable and accurate results; meanwhile it also should be small and simple enough to ease the computation effort. In order to achieve that, geometry simplification is often applied, symmetry and periodic are often considered. It is followed by dividing the whole domain into elements, which constitutes grid or mesh. Structured mesh can give more accurate results with fewer elements, but it is not always favored. Often compromises should be made between the results accuracy and meshing effort. At last, suitable boundary conditions should be assigned and appropriate model should be chosen accordingly.

- Solving

  In commercial CFD packages, the solver is often operated as a “black box”, which only requires users provide appropriate mesh, boundary conditions and model. Most of the commercial codes are based on a finite volume discretization and perform the following operations: integrating the governing equation over each control volume within the computational domain, discretizing of governing equations and solving the algebraic system of equations with iterative methods. Characteristics that make finite-volume method preferable in thermo-fluid dynamics problems include enforcing conservation, being flexible in terms of both geometry and variety of fluid phenomena, directly relate to physical quantities.

- Post-processing

  It mainly includes results visualization and analysis. The raw output of the solver is a huge set of numbers corresponding to the values of each field variable (u, v, w, p, …) at each point of the mesh, which must be manipulated further to obtain the desired predictive quantities. Most CFD packages contain a post-processing section; however others may need an external tool for data treatment.

5.2.2 Boundary conditions (BC)

Boundary conditions are a required component for the mathematical model. It directs motion of flow and specifies fluxes into the computational domain. A wide range of BC types permit the flow to enter and exit the solution domain, in which Neumann and Dirichlet boundary conditions are most well-known conditions, the former one defines the value at the boundary while the other prescribes the gradient of a variable

at the boundary. Taking 3.5KW Windspot simulation as an example, very widely used boundary conditions are listed below.

- Velocity inlet

  It defines velocity vector and scalar properties of flow at inlet boundaries.

- Pressure outlet

  It defines the static/gauge pressure at the outlet boundaries, and the backflow can occur at the signed boundaries.

- Wall (split or no-split)

  It is used to bound fluid and solid regions. In viscous flows, no-split condition is enforced at walls, which leads to, one, tangential fluid velocity equal to wall velocity, two, normal velocity component is set to be zero.

- Symmetry

  It is often used to reduce computational effort, which leads to, one, zero normal velocity at symmetry plane, two, zero normal gradients of all variables at symmetry plane.

- Periodic

  It is used when physical geometry and expected flow pattern or the thermal solution are of a periodically repeating nature, which can help reducing computational effort in problem dramatically.

- Interface

  It is defined on cell faces, which do not have finite thickness and provide means of introducing step change in flow properties.

- Cell zones: fluid

  A fluid zone is a group of cells for which all active equations are solved. It is required to specify the fluid materials and also the motion if necessary.

Usually four moving zone models are used, i.e. Single Reference Frame Model (SRF), Multiple Reference Frame Model (MRF), Mixing Plane Model (MPM), Sliding Mesh Model (SMM).

For SRF, the entire computational domain is referred to a moving reference frame. It is easier to solve due to simple BCs, low computational cost and easy to post-processing and analyze.

For MRF, selected regions of the domain are referred to moving reference frames, during which interaction effects or relative motions of zones with respect to each other are ignored.

For MPM, Influence of neighboring regions accounted for through use of a mixing plane model at rotating/stationary domain interfaces and circumferential non-uniformities in the flow are ignored.

For SMM, motions of specific regions are accounted for by a mesh motion algorithm, flow variables interpolated across a sliding interface. It becomes an unsteady problem and can capture all interaction effects with complete fidelity, but more computationally expensive than SRF, MRF, or MPM.

To sum up, it is recommended to select boundary locations and shapes in such a way that flow either goes in or out but not mandatory. One should not observe large gradients in direction normal to boundary near inlets and outlets, which otherwise indicate an incorrect problem specification. They should also be chosen to achieve better convergence. It is also recommended to minimize grid skewness near boundary.

5.3 Turbulence modeling and its governing equations

Turbulence or turbulent flow is a flow regime characterized by chaotic and stochastic property changes. It is also referred as the “the most important unsolved problem of

classical physics". Reynolds number is an important non-dimensional parameter which describes whether the flow is laminar, in which the flow is well ordered and particles are travel along neighboring layers, or turbulence, in which the orderly pattern of flow ceases to exist at higher Reynolds numbers.

$$R_e = \frac{\rho U L}{\mu} \tag{5.1}$$

Where L is a characteristic length scale, e.g. chord length for airfoil, diameter for cylinder, ρ , U and μ are density, velocity and viscosity for fluid, respectively. Physically, Reynolds number stands for the ratio between inertial forces and viscous forces. The critical number at which transition occurs is approximated between 2300. Flows for which the Reynolds number is smaller than 2300 are supposed to be laminar, while flows for which the Reynolds number is bigger than 2300 are expected to be turbulent.

Mathematically, turbulence is decomposed into a mean motion and into a fluctuation, or eddying motion. For example, assuming $\emptyset$ stands for the component of the flow, e.g. velocity, density, temperature, etc, it can be then denoted by the time-averaging of the component $\overline{\emptyset}$ and the fluctuating of the component $\emptyset'$. The time-averaging of the component are formed at a fixed point in space which is given by:

$$\overline{\emptyset} = \frac{1}{t_1}\int_{t_0}^{t_0+t_1} \emptyset dt \tag{5.2}$$

When approaching the study of fluid dynamics problems, the mathematical model is based on the fundamental mass, momentum and energy conservation principles. The main thrust of present-day research in CFD in turbulence flows is through the time-averaged Navier-Stokes equations, which is referred as RANS equations, which is shown below.

$$\text{Conservation of mass:} \quad \frac{\partial \rho}{\partial t} + \frac{\partial \rho U_i}{\partial x_i} = 0 \tag{5.3}$$

$$\text{Conservation of momentum:} \frac{\partial \rho U_i}{\partial t} + \frac{\partial \rho U_j U_i}{\partial x_j} = \frac{\partial}{x_j}\left(\mu \frac{\partial U_i}{x_j} - \rho\overline{u_i u_j}\right) - \frac{\partial P}{\partial x_i} + F_i \tag{5.4}$$

Where U_i is the time-averaging of the i-component velocity, u_i is the fluctuating of the i-component velocity, F_i is body force. It is shown in the equations that by using the Reynolds decomposition, there are newly introduced unknown, i.e. the Reynolds Stresses: $-\rho\overline{u_i u_j}$, Therefore the RANS equations describes an open set of equations, thus turbulence modeling arises in which additional equations are formulated to model the unknown Reynolds Stresses.

There are two widely used approaches for turbulence modeling, i.e. the Boussinesq approach and the Reynolds stress transport model. The Boussinesq approach relates the Reynolds stresses to the mean flow by a turbulent/eddy viscosity, μ_t, as shown below.

$$R_{ij} = -\rho\overline{u_i u_j} = 2\mu_t S_{ij} - \frac{2}{3}\mu_t \frac{\partial U_k}{\partial x_k}\delta_{ij} - \frac{2}{3}\rho k \delta_{ij} \tag{5.5}$$

Where $S_{ij} = \frac{1}{2}(\frac{\partial U_i}{\partial x_j} + \frac{\partial U_j}{\partial x_i})$, k is the turbulent kinetic energy, Kronecker delta $\delta_{ij} = 0$ for $i \neq j$ and $\delta_{ij} = 1$ for $i = j$. It is noted that the turbulent/eddy viscosity is flow property instead of property of the fluid. The problem now lies in obtaining means or models to find the new unknowns. The models include zero equation model (e.g. Algebraic Model), one equation model (e.g. Spalart-Allmaras model), two-equation model (e.g. k-ω model, k-ε model), they are also called first-order models.

The central concept of second order models is to make direct use of the governing equations for the second order moments (Reynolds stresses). It overcomes the limitations of first order models in dealing with the isotropy of turbulence and relying

on dimensional analysis. The overshoot of this approach, however, is large number of Partial Differential Equations (PDE) induced which involves many unknown or impossible to find corrections. The most famous second order models are the Algebraic Stress Model (ASM) and the Reynolds Stress Model (RSM).

Figure 5.1 illustrated the relationship of different RANS based models and their computation effort comparison.

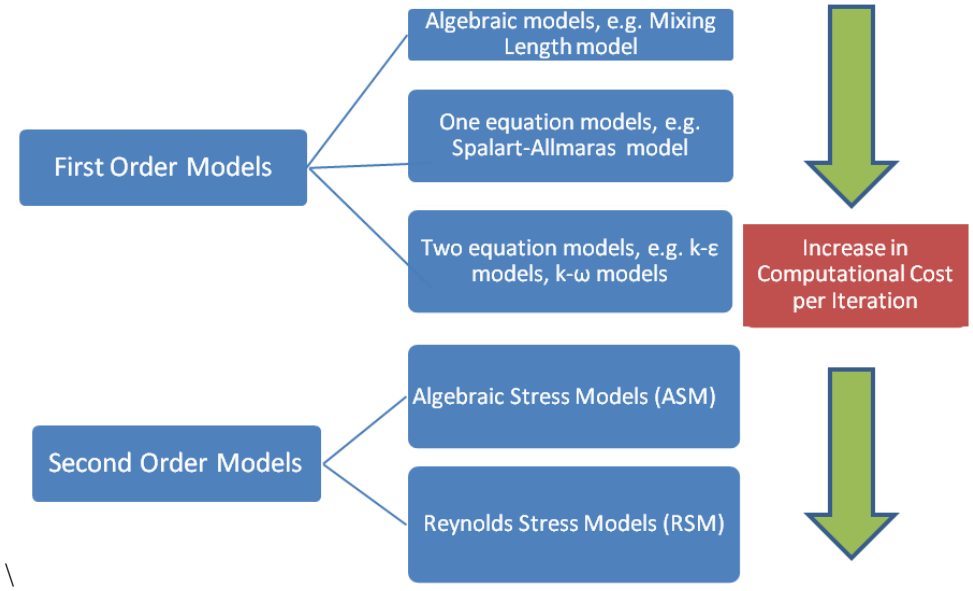

Figure 5. 1 Different RANS based models and their computation effort comparison

Among those turbulence models, k-ω turbulence models are undoubtedly one of the most famous models especially in wind energy application. In the k–ω turbulence models the transport equation of the turbulent kinetic energy is solved together with the equation of the specific rate of dissipation of turbulent kinetic energy, defined as ω = ε/k. This model performs well with free shear flows, flat plate boundary layer flows, complicated adverse pressure gradient flows and separated flows. A problem of the standard k–ω model is the dependency on the free stream boundary conditions. The shear-stress transport (SST) k–ω model was developed by Menter [91, 92] to model

more accurate and reliable for a wider class of flows (e.g., adverse pressure gradient flows, airfoils, transonic shock waves). The SST k–ω model equations are given [97]:

$$\frac{\partial}{\partial t}(\rho k) + \frac{\partial}{\partial x_i}(\rho k u_i) = \frac{\partial}{\partial x_j}\left(\Gamma_k \frac{\partial k}{\partial x_j}\right) + \widetilde{G_k} - Y_k + S_k \tag{5.6}$$

$$\frac{\partial}{\partial t}(\rho \omega) + \frac{\partial}{\partial x_i}(\rho \omega u_i) = \frac{\partial}{\partial x_j}\left(\Gamma_\omega \frac{\partial \omega}{\partial x_j}\right) + G_\omega - Y_\omega + D_\omega + S_\omega \tag{5.7}$$

Where $\widetilde{G_k}$ represents the generation of turbulence kinetic energy due to mean velocity gradients, G_ω represents the generation of ω, Γ_k and Γ_ω represent the effective diffusivity of k and ω, respectively, Y_k and Y_ω represent the dissipation of k and ω due to turbulence, D_ω represents the cross-diffusion term, S_k and S_ω are user-defined source terms.

5.3.1 Wall boundary modeling

In turbulence flow, it is of extreme importance to model the flow close to the wall wisely. Usually, walls are the main source of vorticity and turbulence, there exists very large flow gradients near it, successful prediction of frictional drag for external flow or pressure drop for internal flows depends on fidelity of local wall shear predictions. Simultaneously, using very fine mesh to resolve the steep profiles is still too expensive for many industrial CFD simulations.

In turbulence flow, the region near the wall can be divided into three layers: viscous sub-layer, where molecular viscosity makes the flow behave close to laminar; buffer layer, where the laminar and turbulent properties of the flow are both important; and fully turbulent layer, where the turbulent properties of the flow play the major role.

There are mainly two approaches of handling the turbulence flow over no-slip wall boundary condition. One is the Wall Function (WF) approach where the flow near the wall is not solved, but is given by a semi-empirical function called “wall function”. The other one is Near-Wall (Low-Reynolds Number Turbulence) model approach,

where the mesh is very fine close to the wall, and the conditions are solved all the way to the wall.

Near-wall models aim to resolve the flow right up to the boundary, which strictly require the near-wall gird node to satisfy $y^+ \leq 1$. y^+ is defined by

$$y^+ = \frac{u_\tau y}{v}, u_\tau = \sqrt{\tau_\omega/\rho} \quad (5.8)$$

Where $\tau_\omega$is the wall shear stress, y is the height of the first cell, v is the kinematic viscosity. The demanding requirement for the grid resolution makes the computation very expensive, particularly for the high-speed flows.

Two WF methods are used in FLUENT: standard wall function and non-equilibrium wall function. In FLUENT, for both wall functions, each wall-adjacent cell's centroid is recommended to be located within the log-law layer, $30 \leq y^+ \leq 300$. A value close to the lower bound ($y^+ \sim 30$) is most desirable. As much as possible, the mesh should be made either coarse or fine enough to prevent the wall-adjacent cells from being placed in the buffer layer ($5 \leq y^+ \leq 30$). In current study, $y^+ \sim 50$ was aimed to achieve in the pre-processing, and (5.8) can be used to pre-define the value of y.

5.4 Numerical Model Description and validation

5.4.1 Numerical model description

The numerical model is built around 3.5KW small size HAWT. It is a small scale three-bladed HAWT, with cut-in speed around 3m/s and cut-out speed around 20m/s. Negligible twist angle is observed along the blade. The blade has a rounded tip and unknown airfoil type with a rounded trailing edge, which all later added to mesh difficulties.

Neither the tower nor the ground was included into the model, and a uniform wind speed profile with 10% turbulence intensity is assumed at the entrance of the domain. The computation domain is cylindrical shaped at 3 blade spans in the radial direction and extending upstream roughly 5.25 blade lengths and 15.25 blade lengths downstream of the rotor. The whole computation domain was divided into two fluid regions that are connected with interfaces, i.e. an inner wedge domain which encloses 1/3 of the rotor blade and its immediate surrounding and the rest of the domain, as shown in Figure 5.2.

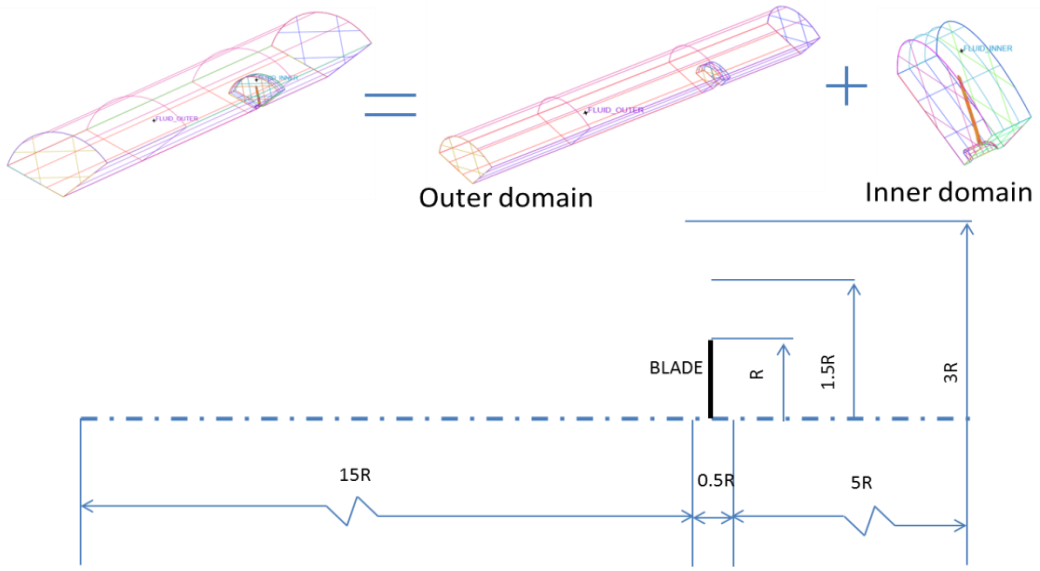

Figure 5. 2 Domain description

It has been proven that hexahedral elements are capable of providing more accurate results than any other type of elements, e.g. tetrahedral. Additionally, fewer elements are needed to mesh a domain with a certain number of nodes, it thus needs less memory for mesh and solution storage and a shorter time for computation [98].

The domain is subdivided into the hexahedral elements (reasonable aspect ratio, low twist and warp angles) carefully. Initial attempt to use Gambit fail to produce

hexahedral mesh, while ICEM pre-processor is successfully used to generate a hexahedral mesh over the topological solid geometry. The solid geometry was constructed in AutoCAD environment and transferred as IGES file into ICEM. The mesh is constructed from a multi block comprises of approximately 4.5 million hexahedral cell. Due to the geometrical complexity of the blade particularly near the blade root transition part, as well as the blunt blade and airfoil tip, multi-block strategy is adapted which greatly facilitated the meshing. The whole domain is initially fitted with a single block; it is then divided into as many as 128 blocks to enable hexahedral mesh type, as shown in Figure 5.3.

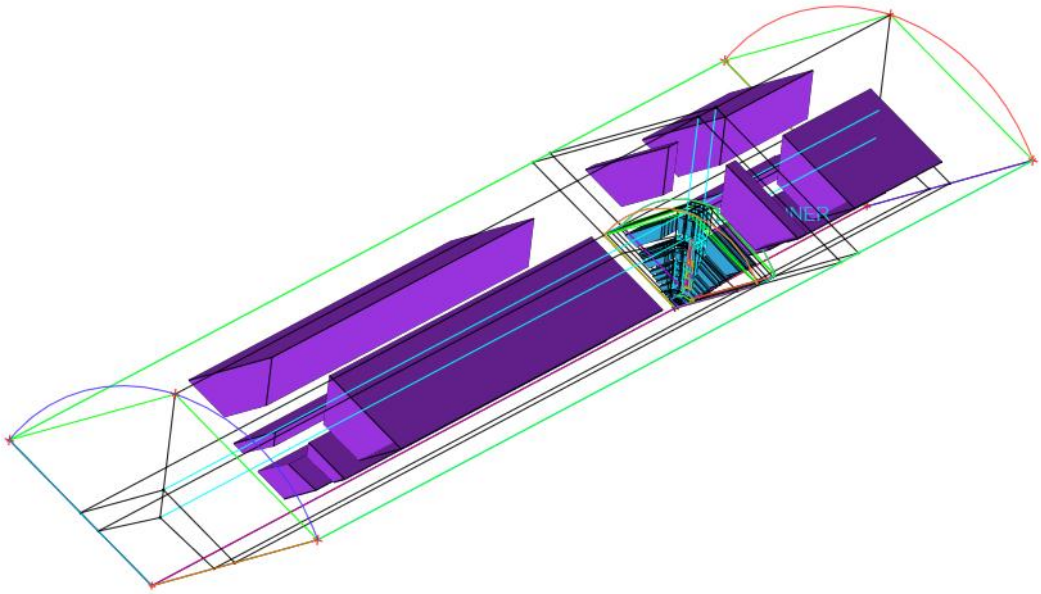

Figure 5. 3 Ultimate blocks for the whole domain

Three O-grids were built around the blade in order to get a better resolution around the blade, blade root and tip, respectively, as shown in Figure 5.4.

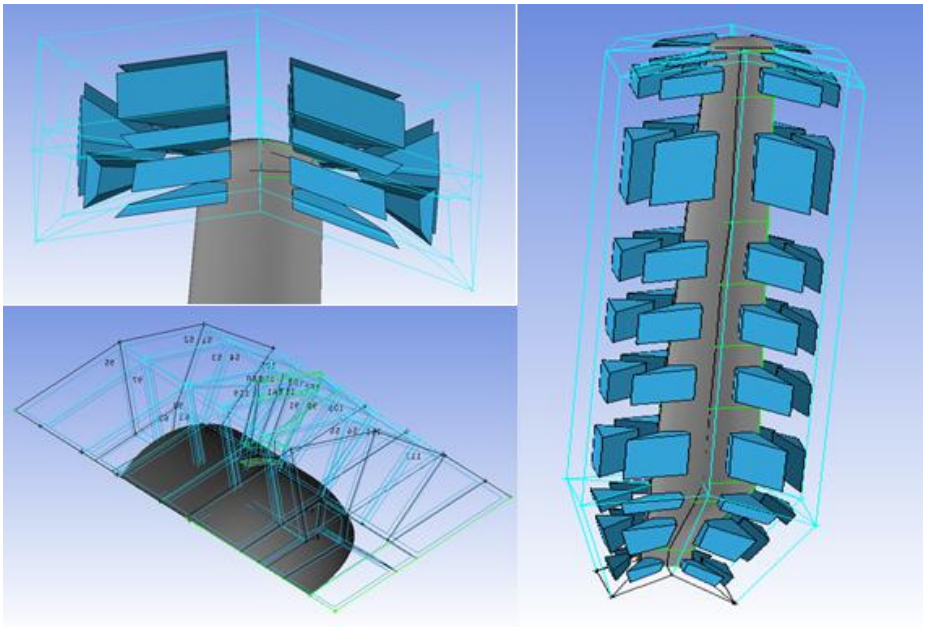

Figure 5. 4 O-grids around the blade, blade root and tip

In order to reduce the mesh size and leave more space for refining mesh at required places, 120 degrees periodicity of the rotor was exploited, only one blade along with the adjacent domain is meshed and the periodicity boundary condition is applied. The mesh for the whole domain is shown in Figure 5.5.

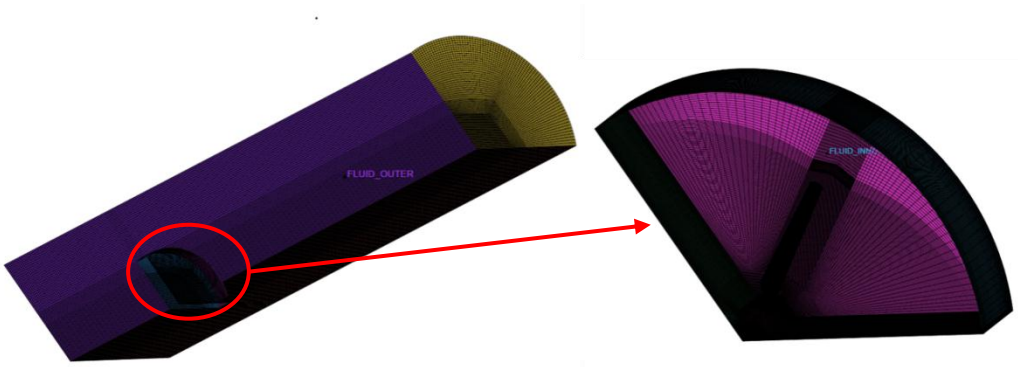

Figure 5. 5 Mesh for the whole domain

Generating mesh with hexahedral elements is generally more difficult for that with other types of elements, e.g. tetrahedral elements. However, the non-conformal interfaces between cells mesh increase flexibility and robustness of the hexahedral

mesh generation [98], which is utilized in the current study. In order to get a better resolution for the domain close to the blade, the whole domain was split into two sub-domains, i.e. inner and outer domain. Then, those two domains was meshed with different mesh parameters, the small inner domain end up with around 3.4 million elements while the outer domain end up with around 1.1 million elements, which lead to non-conformal mesh between this two domains, as shown in Figure 5.6. Interfaces were later assigned to overlapping face meshes.

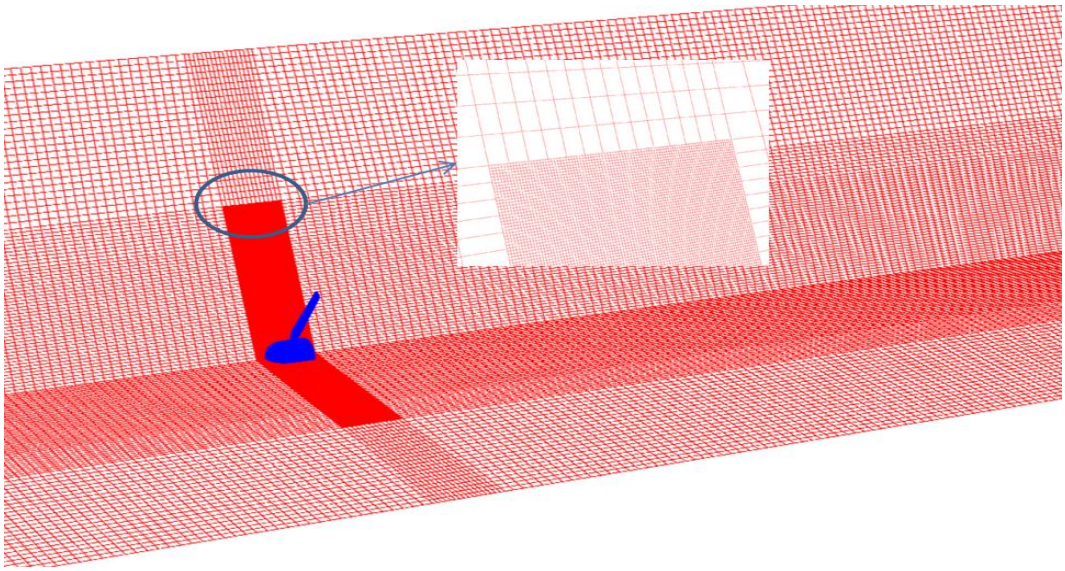

Figure 5. 6 Non-conformal mesh between two domains

The mesh for the blade was carefully taken care of, the two O-grids allows an inflation layer start with height of 0.0001m and 1.2 inflation ratio to achieve y^+ around blade below 50 around the blade, this way wall function can be utilized efficiently for the no-slip wall condition. The mesh detail can be found in Table 5.1 and Figure 5.7.

Table 5. 1 Mesh details for the whole domain

Domain	Mesh type	Element count	Height of fist raw (m)	Inflation ratio	Number of raw
Inner domain	Hexahedral	3.4 million			
Outer domain	Hexahedral	1.1 million			
Around the blade	Hexahedral	--	0.0001	1.2	8

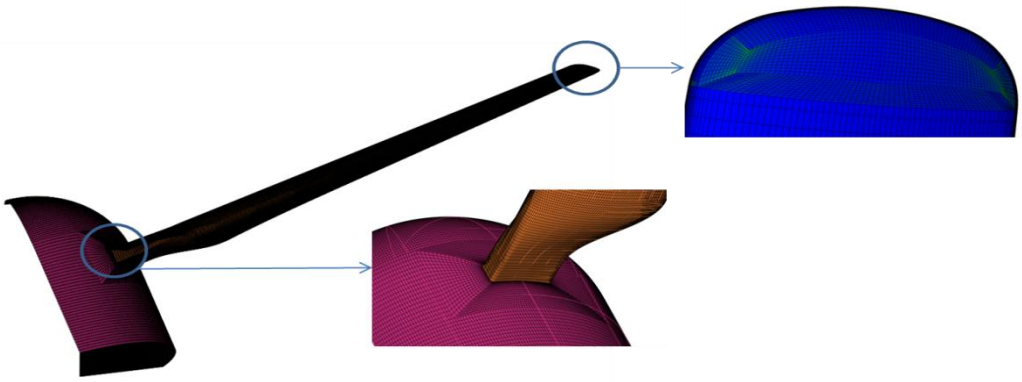

Figure 5. 7 Mesh around the blade

Faces and domains are labeled to assign BCs, as shown in Figure 5.8.

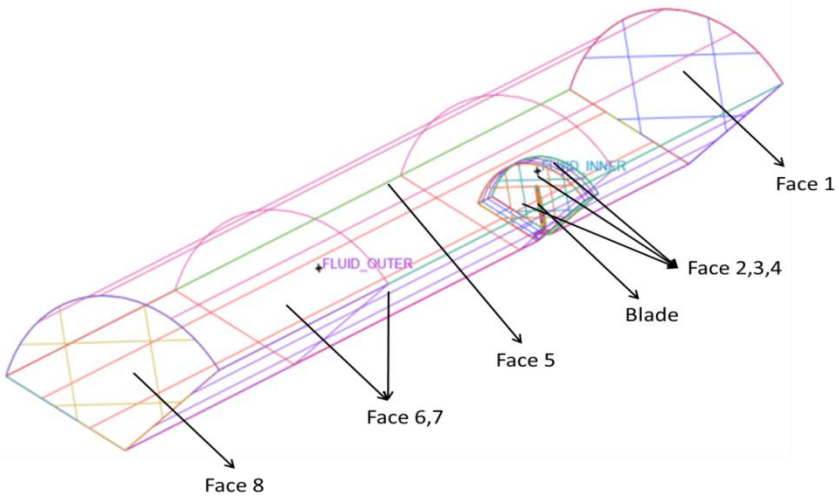

Figure 5. 8 Labeled faces and domains, face 1 represents upstream (z=0), and face 8 represents downstream

The assigned BCs for different faces and domains are shown in Table 5.2.

Table 5. 2 Assigned BCs

Face 1	Velocity inlet (u=v=0, w=constant)
Face 2,3,4	Interface
Blade	No-slip wall
Face 5	Symmetry
Face 6,7	Periodic
Face 8	Outflow

It is required to specify the fluid materials and also the motion in current study. CFD software, e.g. FLUENT, often provide four moving zone models, i.e. Single Reference Frame Model (SRF), Multiple Reference Frame Model (MRF), Mixing Plane Model (MPM), Sliding Mesh Model (SMM). In current study, SRF is used.

The steady, pressure-based solver was used, SIMPLE pressure-velocity coupling scheme, second order upwind was used for solving. The convergence criteria were set 10^{-5} for continuity. SST k-ω turbulence model was implemented to model the flow over the blades.

5.4.2 Model validation: mesh sensitivity study

Mesh sensitivity study was first explored to assess the mesh solution dependency of the model. Four levels of meshes was used, i.e. fine, baseline, course I and course II. Each comprises 5.5, 4.5, 3.05, and 2.26 million cells, respectively. They all ran under the same operating and boundary conditions, i.e. 5m/s velocity inlet, zero rotation speed and zero velocity gradient at the outlet. The calculated thrust and torque are tabulated below.

Table 5. 3 Forces report from model with different mesh size

Mesh level	mesh size (million)	Thrust (N)				Torque (N.m)			
		pressure based	Error (%)	Viscous based	Error (%)	Pressure based	Error (%)	Viscous based	Error (%)
Refined	5.5	33.62	--	0.16	--	5.97	--	0.03	--
Baseline	4.5	33.95	0.98	0.16	0.00	6	0.50	0.03	0.00
Coarse I	3.05	34.37	2.23	0.155	3.13	5.86	1.84	0.024	20.00
Coarse II	2.26	34.68	3.15	0.15	6.25	5.75	3.69	0.02	33.33

It is clear that the two stages of coarse mesh failed to predict the thrust and torque induced by viscosity. They generally have huge error compare to the refined mesh, e.g. 20%. Also the error for thrust induced by pressure is significant. However, when the mesh was refined from baseline to refined, the error for viscous-based force and torque, as well as for pressure-based force and torque becomes negligible, which indicate the mesh is already fine enough for the following studies.

5.5 Results and discussion

5.5.1 Experimental validation

The experimental work was carried out in the Centre for Energy, Environment and Technology (CIEMAT) in Spain. The power generation was recorded under different wind speed, and the rotation speed was recorded accordingly. Since the Windspot 3.5KW is using Passive Centrifugal Variable Pitch System with Shock Absorber for power control, in other words, the turbine will change its pitch angle by itself in order to maintain power output or avoid damages; it invalidates the comparison of the results from simulation and that from experiment. However, it is noted that the pitch angle is constant and equals to that of the non-rotation position if the wind speed is

under around 12m/s, here in the case of experiments carried in CIEMAT, the pitch angle was zero when the turbine is not rotating. This information is extremely important for validating the oncoming simulation work.

The model was simulated typically from 3m/s till 13m/s with 1m/s increment. The model was built with pitch angle zero which is the operation condition for the wind turbine less than 13m/s at the experiment. The wind speed versus the TSR is an important curve to infer from the experimental data. Their importance lies in assigning wind speed and its corresponding rotational rotor speed to avoid unrealistic evaluation of the turbine power coefficient, as plotted in Figure 12.

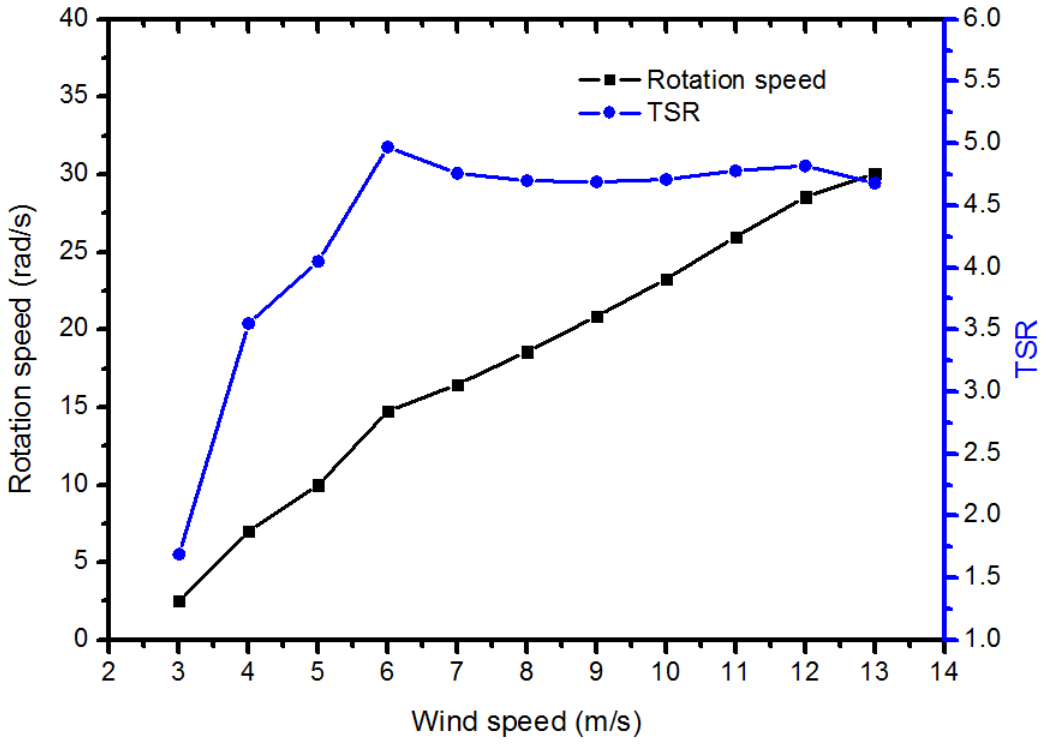

Figure 5. 9 Experimental measurements of rotation speed and TSR [99]

The simulation conditions along with the computed torque and thrust are summarized in Table 5.4.

Table 5. 4 Simulation conditions and corresponding results

Run	Wind speed (m/s)	Rotation speed (rad/s)	TSR	Torque	Thrust
1	3	2.50	1.69	1.45	6.67
2	4	7.02	3.55	4.20	15.98
3	5	10.00	4.05	9.14	42.06
4	6	14.73	4.97	12.65	75.34
5	7	16.47	4.76	17.89	98.46
6	8	18.58	4.70	23.77	127.16
7	9	20.85	4.69	32.91	165.97
8	10	23.26	4.71	37.75	199.86
9	11	25.98	4.78	45.62	246.15
10	12	28.55	4.82	54.50	295.92
11	13	30.06	4.68	65.02	337.48

The power generation under different wind speed obtained from both simulation and experiment are plotted in Figure 5. 10.

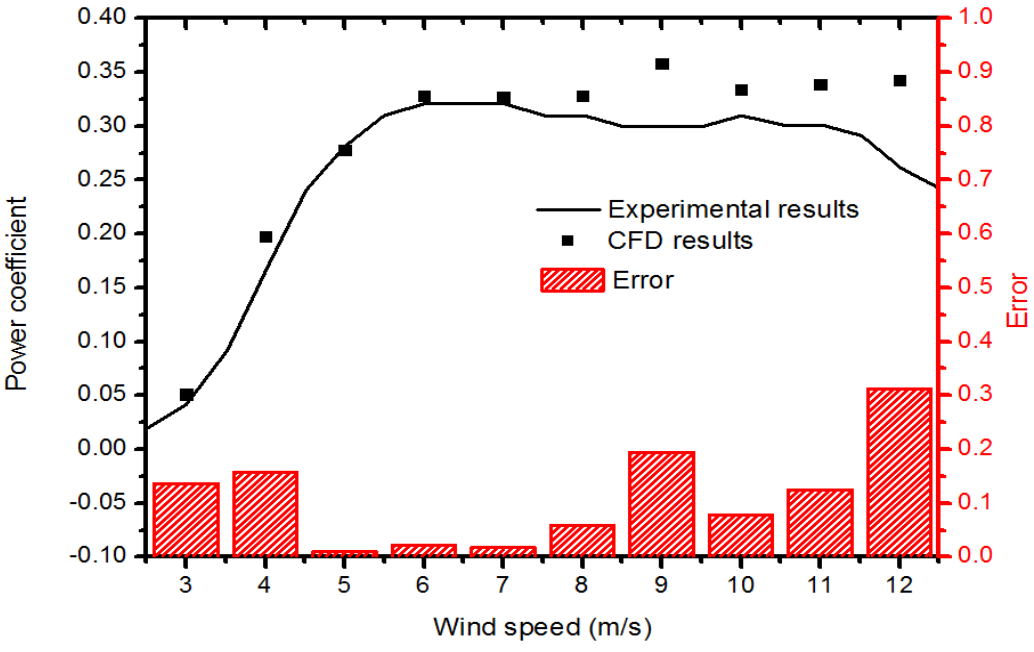

Figure 5. 10 Comparison of power coefficients from both experiment and CFD

Experimental measurements of power coefficient (C_P) and simulation results were plotted together in Figure 5. 10. A good agreement between the CFD simulation

results and experimental data, particularly at wind speed below 9m/s, can be observed. The discrepancy at velocity beyond 9m/s is mainly due to the Pitching System of the blade that connected to Shock Absorber, which tends to increase the Pitch blade angle and consequently increases the angle of attack as speed increases beyond the 9m/s. The trend is been captured experimentally as increasing the angle of attack lead to reduction in the power coefficient. Another reason in discrepancies is due to turbulence modeling. As the wind speed increases, separation and stall of the flow occurs over the blade which lead to SST k-ω turbulence model failure and augment simulation error.

5.5.2 Influence of TSR

The simulation was exploited further to emphasize the dependence of power generation on TSR, as each turbine provides optimal power generation at specific TSR. In these simulations the rotation speed of the wind turbine is fixed, i.e. 12 rad/s, while the inlet wind speed varied from 2m/s to 15m/s. The simulation conditions together with the power generation and power coefficients under these wind speeds are summarized in Table 5.5 and plotted in Figure 5.11 and 5.12.

Table 5. 5 Turbine power generation under different wind speed

case	Wind speed (m/s)	Rotation speed (rad/s)	TSR	Torque (N.m)	Thrust(N)	Power generation (W)
1	15	12	1.6	33.12	141.00	1192.45
2	10	12	2.4	25.18	91.22	906.34
3	8	12	3	20.90	76.11	752.40
4	6	12	4	13.38	60.53	481.83
5	4	12	6	4.23	39.92	152.25
6	3	12	8	0.58	27.95	20.87
7	2	12	12	-1.71	16.58	-61.49

Negative power implies unrealistic turbine conditions as observed at wind speed 2m/s and 12rad/s rotational speed. This is due to the imposed mismatch between low wind speed and high rotational speed. The simulation captured this characteristic successfully.

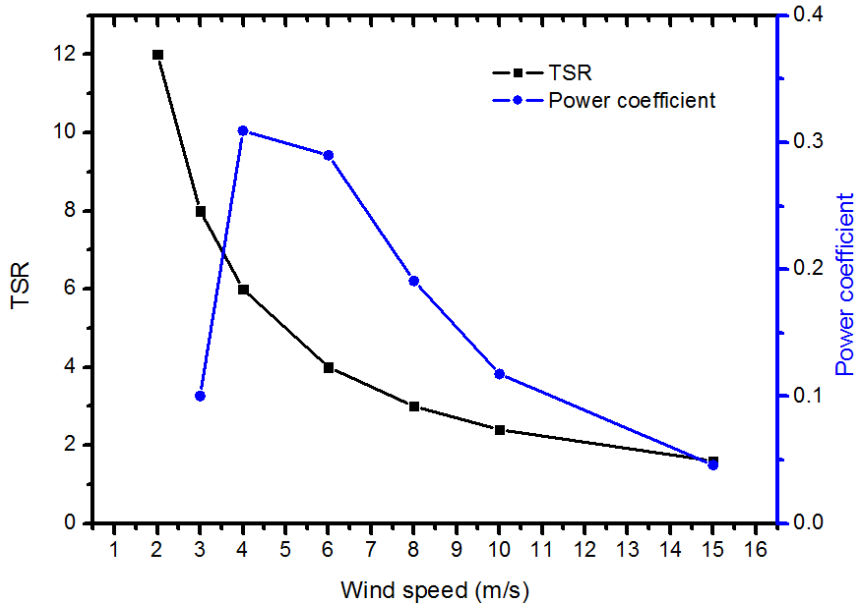

Figure 5. 11 Power coefficients and TSR under different wind speeds

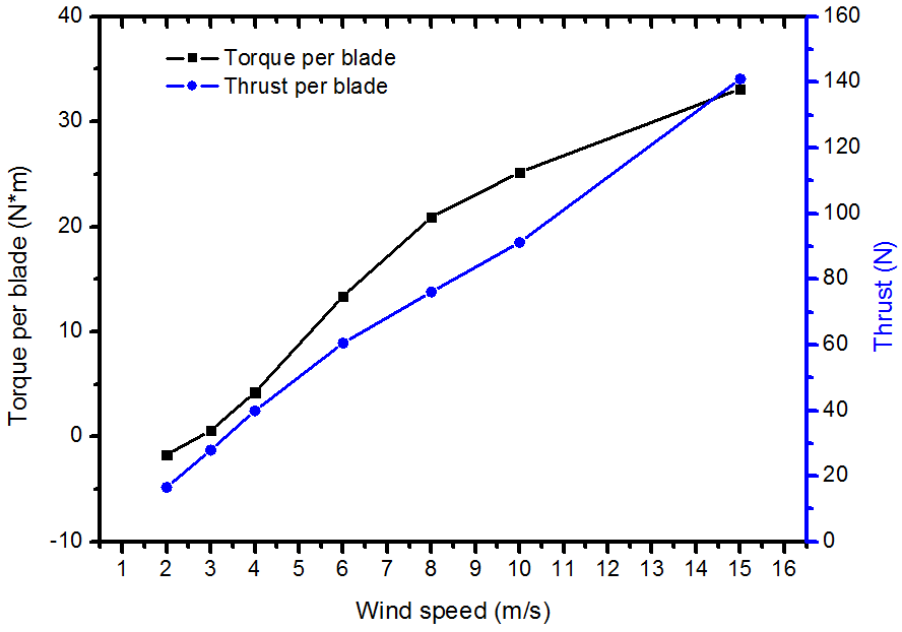

Figure 5. 12 Torque and thrust under different wind speeds

As clearly shown in Figure 5.11, the power coefficients reached by wind turbine dependent on TSR significantly, the difference for achieved power coefficients under different TSRs can be as high as 60 times, e.g. achieved power coefficient is 0.05 at TSR of 1.8 while the power coefficient can reach as high as 0.32 at TSR of 5. Therefore, a wise choice of the TSR of the Windspot is necessary. For the case of Windspot, it harnesses the maximum amount of wind power for the TSR values between 4.5 and 6.0. What can be noticed from Figure 15 is that both the thrust and torque are proportional to the wind speed linearly. The thrust and torque increases linearly as the wind speed increases when the wind speed is less than 15m/s.

5.5.2 Flow plot around blade

The model was simulated under certain conditions: the rotation speed of the wind turbine is fixed, i.e. 12rad/s, while the inlet wind speed ranges from 2m/s to 15m/s, i.e. 2m/s, 3m/s, 4m/s, 6m/s, 8m/s, 10m/s and 15m/s. The plane velocity along z axis are plotted in Figure 5.13, the position was normalized by the radius of the rotor.

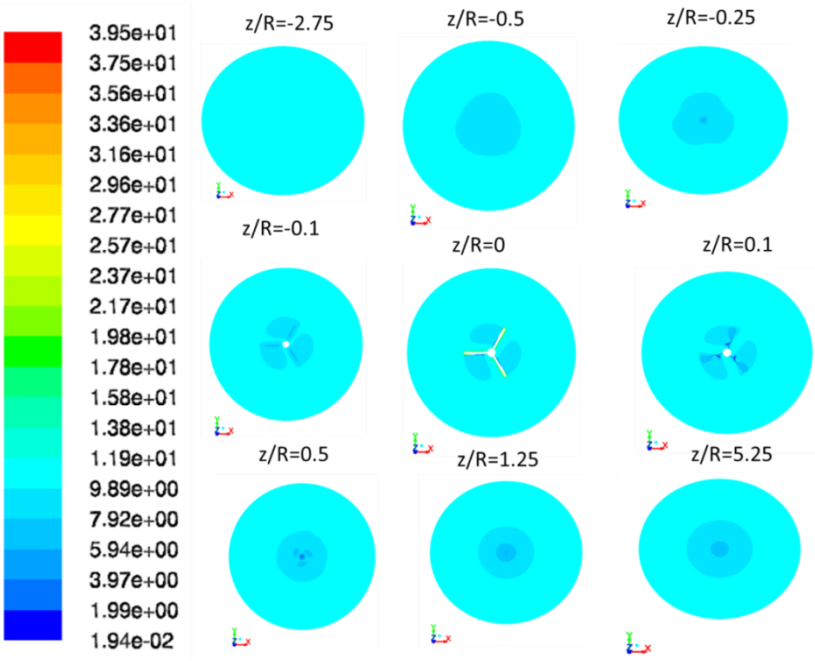

Figure 5. 13 Velocity magnitude along z axis (position is normalized by rotor radius)

The plot clearly show the flow velocity by approaching, passing through the rotor and afterwards. The flow is slowed down because of the turbine is trying to generate power out of the flow, thus the flow is slowed down.

In current work, the flow field past the rotating blade was investigated to give an insight understanding of the rotational effect. The pressure coefficient and velocity magnitude was plotted in Figure 5.15 and 5.16, respectively.

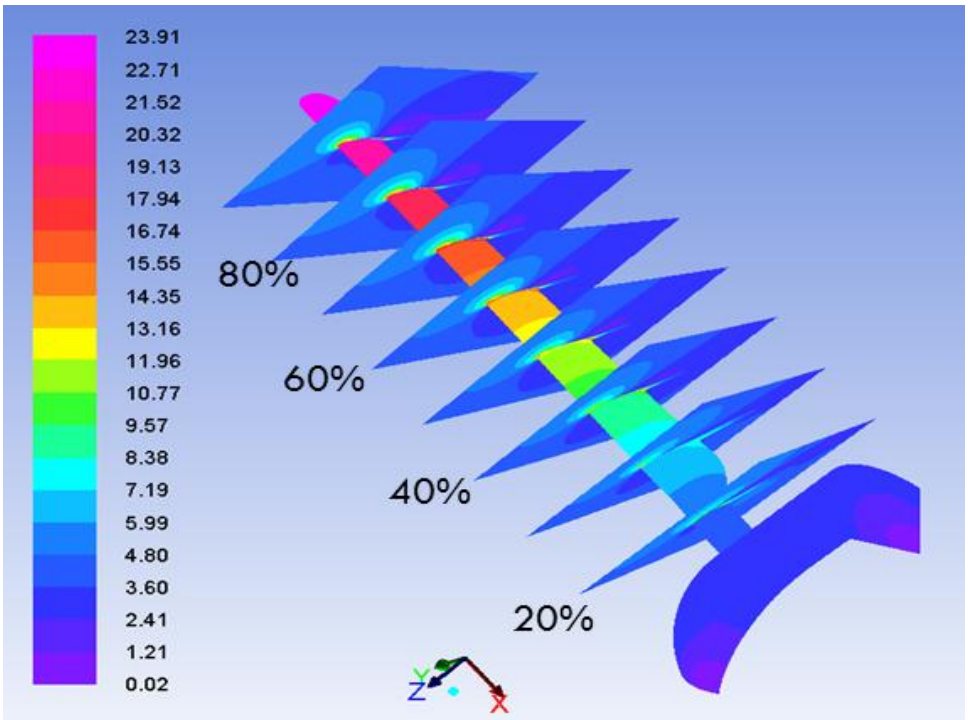

Figure 5. 14 Velocity magnitude along the blade spanwise

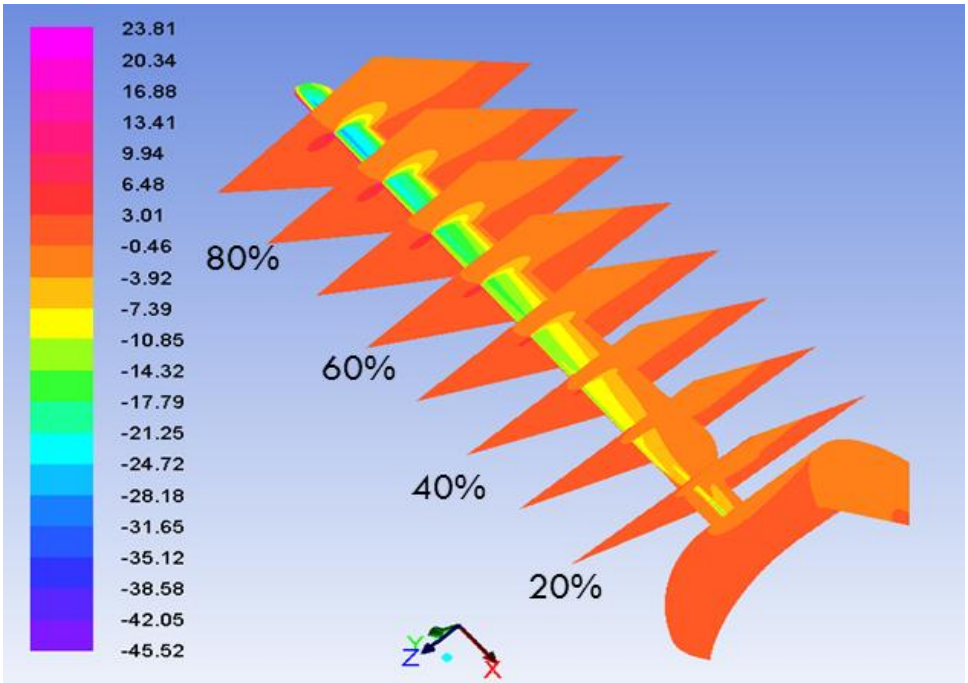

Figure 5. 15 Pressure coefficients along the blade spanwise

A more detailed analysis of the results is needed. Further flow situations (Reynolds number, angle of attack and rotational speed) need to be studied for the simpler geometry.

5.6 Conclusion

A 3D high fidelity CFD for full scale a three bladed 3.5kw HAWT turbine is modeled. The model is based on the full NS equation solution and SST k-ω RANS turbulence model. In order to reduce the computation effort, one third of the rotor domain was modeled enclosing one turbine blade and the periodic BC was imposed. The model was meshed in ICEM using nearly 128 blocks and comprises of 4.5 million hexahedral elements. The forces on blades were first reported under different operation conditions and based on which the power coefficients were obtained. The obtained power coefficients from CFD simulation was in agreement with the reported experimental data, particular under low wind speed, e.g. 9m/s before triggering of the

centrifugal pitching mechanisms and prior to the massive separation that risk the efficiency of the SST k-ω turbulent model. The extended running cases also suggested the importance of choosing appropriate TSR in order to obtain optimum power coefficients. Both the velocity and pressure plots gave a good representation of the flow over the blade.

CHAPTER 6

Conclusion and Future work

6.1 Conclusion

The aim of the thesis is multifold: i), to characterize the wind pattern in Masdar City, ii), to explore the possible implementation of both small scale (3.5 KW Windspot) and large scale (Nordtank 500/41) wind turbine, iii) to carry out low fidelity (BEM) , as well as high fidelity (detailed 3D CFD simulation) simulation to analysis the 3.5KW Windspot performance.

The work starts with a brief introduction to the wind turbine types with their disadvantages and advantages, as well as their main components. The literature review focused on the status of current wind energy development; and the models and techniques that are widely used for wind turbine design and performance prediction.

Measuring and analyzing the wind data at a given site has always been the first step in any wind project development. Consequently, both low and high resolution wind data were collected in Masdar City. The collected data were subjected to turbulence intensity identify, power law modeling, spectrum and wavelet analysis, and Weibull fitting. Masdar City is characterized as extremely poor wind region with high turbulence intensity, i.e. at the height of 10m the achieved power density is much lower than 100W/m^2, while the turbulence intensity can reach as high as 19.82%. The conducted FFT and Wavelet analysis showed the intermittency and turbulence nature

of the collected wind records. The comparison of probability obtained from normal fitting, Weibull fitting and measurement revealed good fitting quality of Weibull distribution. By coupling the wind probability distribution and the given power curve of Nordtank 500/41 and 3.5KW Windspot, the estimated power obtained by the Nordtank 500/41 is nearly equivalent to the power obtained from a hundred 3.5KW Windspots under the same height in Masdar City, i.e. 30m. The capacity factor achieved by the 3.5KW Windspot, however, was higher than that achieved by Nordtank 500/41. Nevertheless, the evaluated low capacity factors (3-10%) for both scale wind turbines are much below the capacity factor achieved in wind farms (20-40%) [100], which discourages their local implementation in Masdar City.

The BEM method was studied with four key corrections: i) Tip loss correction, ii) Buhl empirical correction, iii) Skewed wake correction, iv) the "3D correction" of Snel et al. The analyses showed these corrections were indispensable to attain reasonable accuracy. A MATLAB script was developed incorporating the aforementioned corrections and was validated against the available experimental data of UAE phase-VI turbine. It was then implemented on 3.5KW Windspot. Since it is extremely important to have an accurate aerodynamic data for the turbine airfoil, a detailed 2D CFD simulation was conducted for this purpose. Results of the sensitivity study to wind turbine key parameters (i.e. including pitch angle, twist angle and TSR) emphasized their significance to the design process and influence on wind turbine power generation. In case of 3.5KW Windspot, the study recommended that revising the blade design with twist angle between 0 and 10 degrees, operating the wind turbine under pitch angle between 5 and 10 degrees, and TSR around 4 can result in optimum power generation, i.e. the power coefficient can reach 0.35.

With the intention to have an insight look over the flow over the 3.5KW Windspot blades, 3D CFD simulation was conducted. Factors such as mesh, wall boundary modeling and turbulence modeling, were paid special attention due to the significant role that they play in simulation. The Windspot was meshed in ANSYS ICEM CFD comprising 4.5 million hexahedral elements. The confined rotor domain was subjected to SRF, which is commonly used for rotating flow regimes, i.e. turbomachinery and impellers, and SST k-ω turbulence model were utilized in the simulation. The mesh sensitivity study on the overall blade viscous forces was carried out and proper mesh was utilized for the subsequent analyses. The results showed good agreement with experimental data especially under low wind speed, e.g. below 9m/s. Numerous simulation were carried out under fixed rotation speed, and these results show higher power coefficient for 3.5KW Windspot can be achieved at TSR between 4 and 6. Nevertheless, the flow details around the blade, together with the wake, were also investigated which gave a detailed and micro look at the flow over the whole wind turbine blade.

6.2 Future work

This work opens the following research paths that can complement fundamental understanding of HAWT:

1) Develop better interface for the code of coupling the wind probability distribution and the wind turbine power curve to estimate the achievable capacity factor for wind turbine at a given region.
2) Improve the accuracy of developed BEM based MATLAB code by introducing better correction factor which better considers the rotational effect.
3) Carry out a detailed analysis for the obtained flow data along and cross the span of wind turbine blade.

4) Carry out 3D high fidelity simulation on 3.5KW Windspot utilizing unsteady RANS based turbulence model.

APPENDIX A

Matlab code for wind data analysis

```
%This Matlab script is developed to estimate the annual power
generation of wind turbine by
%coupling power curve of wind turbine with Weibull distribution
fitted to
%the wind data collected
%done by Liu Su

%% Winddata input and required variable declaration

I=load('wind_station_MeasData_2010_every10min.txt');
U_50=I(:,1); %wind speed at 50m
U_49=I(:,5); %wind speed at 49m
U_40=I(:,9); %wind speed at 40m
U_30=I(:,13); %wind speed at 30m
U_10=I(:,17); %wind speed at 10m
N=length(U_50);
d=I(:,27);% air density

%% Monthly and yearly average wind potential under different heights

%50m

P_50=0.5*(1/N)*(sum(d.*((U_50.*U_50).*U_50))) % Annual average
potential per square meter
P_50_month=zeros(12,1);
P_50_month(1)=0.5*(1/(length(1:4464)))*(sum(d(1:4464).*(((U_50(1:4464
)).*(U_50(1:4464))).*(U_50(1:4464)))));
P_50_month(2)=0.5*(1/(length(4465:8496)))*(sum(d(4465:8496).*(((U_50(
4465:8496)).*(U_50(4465:8496))).*(U_50(4465:8496)))));
P_50_month(3)=0.5*(1/(length(8497:12960)))*(sum(d(8497:12960).*(((U_5
0(8497:12960)).*(U_50(8497:12960))).*(U_50(8497:12960)))));
P_50_month(4)=0.5*(1/(length(12961:17280)))*(sum(d(12961:17280).*(((U
_50(12961:17280)).*(U_50(12961:17280))).*(U_50(12961:17280)))));
P_50_month(5)=0.5*(1/(length(17281:21744)))*(sum(d(17281:21744).*(((U
_50(17281:21744)).*(U_50(17281:21744))).*(U_50(17281:21744)))));
P_50_month(6)=0.5*(1/(length(21745:26064)))*(sum(d(21745:26064).*(((U
_50(21745:26064)).*(U_50(21745:26064))).*(U_50(21745:26064)))));
P_50_month(7)=0.5*(1/(length(26065:30528)))*(sum(d(26065:30528).*(((U
_50(26065:30528)).*(U_50(26065:30528))).*(U_50(26065:30528)))));
P_50_month(8)=0.5*(1/(length(30529:34992)))*(sum(d(30529:34992).*(((U
_50(30529:34992)).*(U_50(30529:34992))).*(U_50(30529:34992)))));
P_50_month(9)=0.5*(1/(length(34993:39312)))*(sum(d(34993:39312).*(((U
_50(34993:39312)).*(U_50(34993:39312))).*(U_50(34993:39312)))));
```

```
P_50_month(10)=0.5*(1/(length(39313:43776)))*(sum(d(39313:43776).*(((
U_50(39313:43776)).*(U_50(39313:43776))).*(U_50(39313:43776)))));
P_50_month(11)=0.5*(1/(length(43777:48096)))*(sum(d(43777:48096).*(((
U_50(43777:48096)).*(U_50(43777:48096))).*(U_50(43777:48096)))));
P_50_month(12)=0.5*(1/(length(48097:52560)))*(sum(d(48097:52560).*(((
U_50(48097:52560)).*(U_50(48097:52560))).*(U_50(48097:52560)))));

%49m

P_49=0.5*(1/N)*(sum(d.*((U_49.*U_49).*U_49))) % Annual average
potential per square meter
P_49_month=zeros(12,1);
P_49_month(1)=0.5*(1/(length(1:4464)))*(sum(d(1:4464).*(((U_49(1:4464
)).*(U_49(1:4464))).*(U_49(1:4464)))));
P_49_month(2)=0.5*(1/(length(4465:8496)))*(sum(d(4465:8496).*(((U_49(
4465:8496)).*(U_49(4465:8496))).*(U_49(4465:8496)))));
P_49_month(3)=0.5*(1/(length(8497:12960)))*(sum(d(8497:12960).*(((U_4
9(8497:12960)).*(U_49(8497:12960))).*(U_49(8497:12960)))));
P_49_month(4)=0.5*(1/(length(12961:17280)))*(sum(d(12961:17280).*(((U
_49(12961:17280)).*(U_49(12961:17280))).*(U_49(12961:17280)))));
P_49_month(5)=0.5*(1/(length(17281:21744)))*(sum(d(17281:21744).*(((U
_49(17281:21744)).*(U_49(17281:21744))).*(U_49(17281:21744)))));
P_49_month(6)=0.5*(1/(length(21745:26064)))*(sum(d(21745:26064).*(((U
_49(21745:26064)).*(U_49(21745:26064))).*(U_49(21745:26064)))));
P_49_month(7)=0.5*(1/(length(26065:30528)))*(sum(d(26065:30528).*(((U
_49(26065:30528)).*(U_49(26065:30528))).*(U_49(26065:30528)))));
P_49_month(8)=0.5*(1/(length(30529:34992)))*(sum(d(30529:34992).*(((U
_49(30529:34992)).*(U_49(30529:34992))).*(U_49(30529:34992)))));
P_49_month(9)=0.5*(1/(length(34993:39312)))*(sum(d(34993:39312).*(((U
_49(34993:39312)).*(U_49(34993:39312))).*(U_49(34993:39312)))));
P_49_month(10)=0.5*(1/(length(39313:43776)))*(sum(d(39313:43776).*(((
U_49(39313:43776)).*(U_49(39313:43776))).*(U_49(39313:43776)))));
P_49_month(11)=0.5*(1/(length(43777:48096)))*(sum(d(43777:48096).*(((
U_49(43777:48096)).*(U_49(43777:48096))).*(U_49(43777:48096)))));
P_49_month(12)=0.5*(1/(length(48097:52560)))*(sum(d(48097:52560).*(((
U_49(48097:52560)).*(U_49(48097:52560))).*(U_49(48097:52560)))));

%40m

P_40=0.5*(1/N)*(sum(d.*((U_40.*U_40).*U_40))) % Annual average
potential per square meter
P_40_month=zeros(12,1);
P_40_month(1)=0.5*(1/(length(1:4464)))*(sum(d(1:4464).*(((U_50(1:4464
)).*(U_50(1:4464))).*(U_50(1:4464)))));
P_40_month(2)=0.5*(1/(length(4465:8496)))*(sum(d(4465:8496).*(((U_40(
4465:8496)).*(U_40(4465:8496))).*(U_40(4465:8496)))));
P_40_month(3)=0.5*(1/(length(8497:12960)))*(sum(d(8497:12960).*(((U_4
0(8497:12960)).*(U_40(8497:12960))).*(U_40(8497:12960)))));
P_40_month(4)=0.5*(1/(length(12961:17280)))*(sum(d(12961:17280).*(((U
_40(12961:17280)).*(U_40(12961:17280))).*(U_40(12961:17280)))));
P_40_month(5)=0.5*(1/(length(17281:21744)))*(sum(d(17281:21744).*(((U
_40(17281:21744)).*(U_40(17281:21744))).*(U_40(17281:21744)))));
P_40_month(6)=0.5*(1/(length(21745:26064)))*(sum(d(21745:26064).*(((U
_40(21745:26064)).*(U_40(21745:26064))).*(U_40(21745:26064)))));
P_40_month(7)=0.5*(1/(length(26065:30528)))*(sum(d(26065:30528).*(((U
_40(26065:30528)).*(U_40(26065:30528))).*(U_40(26065:30528)))));
P_40_month(8)=0.5*(1/(length(30529:34992)))*(sum(d(30529:34992).*(((U
_40(30529:34992)).*(U_40(30529:34992))).*(U_40(30529:34992)))));
P_40_month(9)=0.5*(1/(length(34993:39312)))*(sum(d(34993:39312).*(((U
_40(34993:39312)).*(U_40(34993:39312))).*(U_40(34993:39312)))));
```

```
P_40_month(10)=0.5*(1/(length(39313:43776)))*(sum(d(39313:43776).*(((
U_40(39313:43776)).*(U_40(39313:43776))).*(U_40(39313:43776)))));
P_40_month(11)=0.5*(1/(length(43777:48096)))*(sum(d(43777:48096).*(((
U_40(43777:48096)).*(U_40(43777:48096))).*(U_40(43777:48096)))));
P_40_month(12)=0.5*(1/(length(48097:52560)))*(sum(d(48097:52560).*(((
U_40(48097:52560)).*(U_40(48097:52560))).*(U_40(48097:52560)))));

%30m

P_30=0.5*(1/N)*(sum(d.*((U_30.*U_30).*U_30))) % Annual average
potential per square meter
P_30_month=zeros(12,1);
P_30_month(1)=0.5*(1/(length(1:4464)))*(sum(d(1:4464).*(((U_30(1:4464
)).*(U_30(1:4464))).*(U_30(1:4464)))));
P_30_month(2)=0.5*(1/(length(4465:8496)))*(sum(d(4465:8496).*(((U_30(
4465:8496)).*(U_30(4465:8496))).*(U_30(4465:8496)))));
P_30_month(3)=0.5*(1/(length(8497:12960)))*(sum(d(8497:12960).*(((U_3
0(8497:12960)).*(U_30(8497:12960))).*(U_30(8497:12960)))));
P_30_month(4)=0.5*(1/(length(12961:17280)))*(sum(d(12961:17280).*(((U
_30(12961:17280)).*(U_30(12961:17280))).*(U_30(12961:17280)))));
P_30_month(5)=0.5*(1/(length(17281:21744)))*(sum(d(17281:21744).*(((U
_30(17281:21744)).*(U_30(17281:21744))).*(U_30(17281:21744)))));
P_30_month(6)=0.5*(1/(length(21745:26064)))*(sum(d(21745:26064).*(((U
_30(21745:26064)).*(U_30(21745:26064))).*(U_30(21745:26064)))));
P_30_month(7)=0.5*(1/(length(26065:30528)))*(sum(d(26065:30528).*(((U
_30(26065:30528)).*(U_30(26065:30528))).*(U_30(26065:30528)))));
P_30_month(8)=0.5*(1/(length(30529:34992)))*(sum(d(30529:34992).*(((U
_30(30529:34992)).*(U_30(30529:34992))).*(U_30(30529:34992)))));
P_30_month(9)=0.5*(1/(length(34993:39312)))*(sum(d(34993:39312).*(((U
_30(34993:39312)).*(U_30(34993:39312))).*(U_30(34993:39312)))));
P_30_month(10)=0.5*(1/(length(39313:43776)))*(sum(d(39313:43776).*(((
U_30(39313:43776)).*(U_30(39313:43776))).*(U_30(39313:43776)))));
P_30_month(11)=0.5*(1/(length(43777:48096)))*(sum(d(43777:48096).*(((
U_30(43777:48096)).*(U_30(43777:48096))).*(U_30(43777:48096)))));
P_30_month(12)=0.5*(1/(length(48097:52560)))*(sum(d(48097:52560).*(((
U_30(48097:52560)).*(U_30(48097:52560))).*(U_30(48097:52560)))));

%10m

P_10=0.5*(1/N)*(sum(d.*((U_10.*U_10).*U_10))) % Annual average
potential per square meter
P_10_month=zeros(12,1);
P_10_month(1)=0.5*(1/(length(1:4464)))*(sum(d(1:4464).*(((U_10(1:4464
)).*(U_10(1:4464))).*(U_10(1:4464)))));
P_10_month(2)=0.5*(1/(length(4465:8496)))*(sum(d(4465:8496).*(((U_10(
4465:8496)).*(U_10(4465:8496))).*(U_10(4465:8496)))));
P_10_month(3)=0.5*(1/(length(8497:12960)))*(sum(d(8497:12960).*(((U_1
0(8497:12960)).*(U_10(8497:12960))).*(U_10(8497:12960)))));
P_10_month(4)=0.5*(1/(length(12961:17280)))*(sum(d(12961:17280).*(((U
_10(12961:17280)).*(U_10(12961:17280))).*(U_10(12961:17280)))));
P_10_month(5)=0.5*(1/(length(17281:21744)))*(sum(d(17281:21744).*(((U
_10(17281:21744)).*(U_10(17281:21744))).*(U_10(17281:21744)))));
P_10_month(6)=0.5*(1/(length(21745:26064)))*(sum(d(21745:26064).*(((U
_10(21745:26064)).*(U_10(21745:26064))).*(U_10(21745:26064)))));
P_10_month(7)=0.5*(1/(length(26065:30528)))*(sum(d(26065:30528).*(((U
_10(26065:30528)).*(U_10(26065:30528))).*(U_10(26065:30528)))));
P_10_month(8)=0.5*(1/(length(30529:34992)))*(sum(d(30529:34992).*(((U
_10(30529:34992)).*(U_10(30529:34992))).*(U_10(30529:34992)))));
P_10_month(9)=0.5*(1/(length(34993:39312)))*(sum(d(34993:39312).*(((U
_10(34993:39312)).*(U_10(34993:39312))).*(U_10(34993:39312)))));
```

```
P_10_month(10)=0.5*(1/(length(39313:43776)))*(sum(d(39313:43776).*(((
U_10(39313:43776)).*(U_10(39313:43776))).*(U_10(39313:43776)))));
P_10_month(11)=0.5*(1/(length(43777:48096)))*(sum(d(43777:48096).*(((
U_10(43777:48096)).*(U_10(43777:48096))).*(U_10(43777:48096)))));
P_10_month(12)=0.5*(1/(length(48097:52560)))*(sum(d(48097:52560).*(((
U_10(48097:52560)).*(U_10(48097:52560))).*(U_10(48097:52560)))));

P_annual=[P_10 P_30 P_40 P_49 P_50];


%% Yearly average wind speed and Turbulence intensity under different
heights

%50m

Uavg_50=(1/N)*(sum(U_50)); % Mean wind velocity
thita_50=((1/(N-1))*sum((U_50-Uavg_50).*(U_50-Uavg_50)))^0.5;
TI_50=thita_50/Uavg_50; % Turbulence intensity

U_north_50=U_50.*sin((I(:,23)*pi/180));
Uavg_north_50=(1/N)*(sum(U_north_50)) % 50m, North time mean wind
velocity
thita_north_50=((1/(N-1))*sum((U_north_50-
Uavg_north_50).*(U_north_50-Uavg_north_50)))^0.5;
TI_north_50=thita_north_50/Uavg_north_50% 50m turbulence intensity

U_east_50=U_50.*cos((I(:,23)*pi/180));
Uavg_east_50=(1/N)*(sum(U_east_50)) % 50m, east time mean wind
velocity
thita_east_50=((1/(N-1))*sum((U_east_50-Uavg_east_50).*(U_east_50-
Uavg_east_50)))^0.5;
TI_east_50=thita_east_50/Uavg_east_50% 50m turbulence intensity

TI_50_average=0.5*(TI_north_50+TI_east_50);

%49m

Uavg_49=(1/N)*(sum(U_49)); % Mean wind velocity
thita_49=((1/(N-1))*sum((U_49-Uavg_49).*(U_49-Uavg_49)))^0.5;
TI_49=thita_49/Uavg_49; % Turbulence intensity

%40m

Uavg_40=(1/N)*(sum(U_40)); % Mean wind velocity
thita_40=((1/(N-1))*sum((U_40-Uavg_40).*(U_40-Uavg_40)))^0.5;
TI_40=thita_40/Uavg_40; % Turbulence intensity

%30m

Uavg_30=(1/N)*(sum(U_30)); % Mean wind velocity
thita_30=((1/(N-1))*sum((U_30-Uavg_30).*(U_30-Uavg_30)))^0.5;
TI_30=thita_30/Uavg_30; % Turbulence intensity

% U_north_30=U_30.*sin((I(:,21)*pi/180));
% Uavg_north_30=(1/N)*(sum(U_north_30)) % 50m, North time mean wind
velocity
% thita_north_30=((1/(N-1))*sum((U_north_30-
Uavg_north_30).*(U_north_30-Uavg_north_30)))^0.5;
```

```
% TI_north_30=thita_north_30/Uavg_north_30% 50m turbulence intensity
%
% U_east_30=U_30.*cos((I(:,21)*pi/180));
% Uavg_east_30=(1/N)*(sum(U_east_30)) % 50m, east time mean wind
velocity
% thita_east_30=((1/(N-1))*sum((U_east_30-Uavg_east_30).*(U_east_30-
Uavg_east_30)))^0.5;
% TI_east_30=thita_east_30/Uavg_east_30% 50m turbulence intensity
%
% TI_30_average=0.5*(TI_north_30+TI_east_30);

%10m

Uavg_10=(1/N)*(sum(U_10)); % Mean wind velocity
thita_10=((1/(N-1))*sum((U_10-Uavg_10).*(U_10-Uavg_10)))^0.5;
TI_10=thita_10/Uavg_10; % Turbulence intensity

%% Normal fitting function for wind speed under different heights

U=0:0.1:25;
Pro_50=(1/(thita_50*(2*pi)^0.5))*exp(-(U-Uavg_50).^2/(2*thita_50^2))
% 50m probability
Pro_49=(1/(thita_49*(2*pi)^0.5))*exp(-(U-Uavg_49).^2/(2*thita_49^2))
% 49m probability
Pro_40=(1/(thita_40*(2*pi)^0.5))*exp(-(U-Uavg_40).^2/(2*thita_40^2))
% 40m probability
Pro_30=(1/(thita_30*(2*pi)^0.5))*exp(-(U-Uavg_30).^2/(2*thita_30^2))
% 30m probability
Pro_10=(1/(thita_10*(2*pi)^0.5))*exp(-(U-Uavg_10).^2/(2*thita_10^2))
% 10m probability


%% Weibull fitting function for wind speed under different heights
%Maximum likelihood method was utilized to obtain the two key
factors:
%shape factor k and scale factor c

%50m

U_50r=U_50(U_50 ~= 0);
N_50=length(U_50r);
k_ini_50=2;
err_50=1;
while err_50>0.1
k_50=((sum((U_50r.^k_ini_50).*log(U_50r)))/(sum((U_50r.^k_ini_50)))-
(sum(log(U_50r)))/N_50)^(-1);
err_50=k_50-k_ini_50;
k_ini_50=k_50;
end
k_50=k_ini_50;
c_50=((1/N)*sum(U_50.^k_50))^(1/k_50);
fu_50=(k_50/c_50^k_50)*(U.^(k_50-1)).*exp(-(U./c_50).^k_50);
%probability density function at 50m
FU_50=1-exp(-(U./c_50).^k_50); %cummulative distribution function at
50m
U_50mp=c_50*((k_50-1)/k_50)^(1/k_50); %most probable wind speed at
50m
U_50maxe=c_50*((k_50+2)/k_50)^(1/k_50); %wind speed carrying maximum
energy at 50m
```

```
%49m

U_49r=U_49(U_49 ~= 0);
N_49=length(U_49r);
k_ini_49=2;
err_49=1;
while err_49>0.1
k_49=((sum((U_49r.^k_ini_49).*log(U_49r)))/(sum((U_49r.^k_ini_49)))-
(sum(log(U_49r)))/N_49)^(-1);
err_49=k_49-k_ini_49;
k_ini_49=k_49;
end
k_49=k_ini_49;
c_49=((1/N)*sum(U_49.^k_49))^(1/k_49);
fu_49=(k_49/c_49^k_49)*(U.^(k_49-1)).*exp(-(U./c_49).^k_49);
%probability density function at 50m
FU_49=1-exp(-(U./c_49).^k_49); %cummulative distribution function at
49m
U_49mp=c_49*((k_49-1)/k_49)^(1/k_49); %most probable wind speed at
49m
U_49maxe=c_49*((k_49+2)/k_49)^(1/k_49); %wind speed carrying maximum
energy at 49m

%40m

U_40r=U_40(U_40 ~= 0);
N_40=length(U_40r);
k_ini_40=2;
err_40=1;
while err_40>0.1
k_40=((sum((U_40r.^k_ini_40).*log(U_40r)))/(sum((U_40r.^k_ini_40)))-
(sum(log(U_40r)))/N_40)^(-1);
err_40=k_40-k_ini_40;
k_ini_40=k_40;
end
k_40=k_ini_40;
c_40=((1/N)*sum(U_40.^k_40))^(1/k_40);
fu_40=(k_40/c_40^k_40)*(U.^(k_40-1)).*exp(-(U./c_40).^k_40);
%probability density function at 50m
FU_40=1-exp(-(U./c_40).^k_40); %cummulative distribution function at
40m
U_40mp=c_40*((k_40-1)/k_40)^(1/k_40); %most probable wind speed at
40m
U_40maxe=c_40*((k_40+2)/k_40)^(1/k_40); %wind speed carrying maximum
energy at 40m

%30m

U_30r=U_30(U_30 ~= 0);
N_30=length(U_30r);
k_ini_30=2;
err_30=1;
while err_30>0.1
k_30=((sum((U_30r.^k_ini_30).*log(U_30r)))/(sum((U_30r.^k_ini_30)))-
(sum(log(U_30r)))/N_30)^(-1);
err_30=k_30-k_ini_30;
k_ini_30=k_30;
end
k_30=k_ini_30;
```

```
c_30=((1/N)*sum(U_30.^k_30))^(1/k_30);
fu_30=(k_30/c_30^k_30)*(U.^(k_30-1)).*exp(-(U./c_30).^k_30);
%probability density function at 30m
FU_30=1-exp(-(U./c_30).^k_30); %cummulative distribution function at
30m
U_30mp=c_30*((k_30-1)/k_30)^(1/k_30); %most probable wind speed at
30m
U_30maxe=c_30*((k_30+2)/k_30)^(1/k_30); %wind speed carrying maximum
energy at 30m

%10m

U_10r=U_10(U_10 ~= 0);
N_10=length(U_10r);
k_ini_10=2;
err_10=1;
while err_10>0.1
k_10=((sum((U_10r.^k_ini_10).*log(U_10r)))/(sum((U_10r.^k_ini_10)))-
(sum(log(U_10r)))/N_10)^(-1);
err_10=k_10-k_ini_10;
k_ini_10=k_10;
end
k_10=k_ini_10;
c_10=((1/N)*sum(U_10.^k_10))^(1/k_10);
fu_10=(k_10/c_10^k_10)*(U.^(k_10-1)).*exp(-(U./c_10).^k_10);
%probability density function at 10m
FU_10=1-exp(-(U./c_10).^k_10); %cummulative distribution function at
10m
U_10mp=c_10*((k_10-1)/k_10)^(1/k_10); %most probable wind speed at
10m
U_10maxe=c_10*((k_10+2)/k_10)^(1/k_10); %wind speed carrying maximum
energy at 10m

%% Coupling the power with weibull fitting, achievable capacity
factor evaluation
% The wind turbine power curve was fitted with the function:

V=0:0.1:25;
M=length(V);
P_cof=zeros(1,M);

% Nordtank 500/41

for i=1:M
if V(i)<=4
    P_cof(i)=0;
else P_cof(i)=0.0261*V(i)^4 - 1.4616*V(i)^3 + 26.298*V(i)^2 -
131.89*V(i) + 192.88;
end
end

P_annual_50_N=365*24*(sum(fu_50.*P_cof)); % Annual power generation
at height of 50m
P_annual_49_N=365*24*(sum(fu_49.*P_cof)); % Annual power generation
at height of 49m
P_annual_40_N=365*24*(sum(fu_40.*P_cof)); % Annual power generation
at height of 40m
P_annual_30_N=365*24*(sum(fu_30.*P_cof)); % Annual power generation
at height of 30m
```

```
P_annual_10_N=365*24*(sum(fu_10.*P_cof)); % Annual power generation
at height of 10m

f_cap_50m_N=P_annual_50_N/(365*24*(sum(fu_50.*500))); % Capacity
factor at height of 50m
f_cap_49m_N=P_annual_49_N/(365*24*(sum(fu_49.*500))); % Capacity
factor at height of 49m
f_cap_40m_N=P_annual_40_N/(365*24*(sum(fu_40.*500))); % Capacity
factor at height of 40m
f_cap_30m_N=P_annual_30_N/(365*24*(sum(fu_30.*500))); % Capacity
factor at height of 30m
f_cap_10m_N=P_annual_10_N/(365*24*(sum(fu_10.*500))); % Capacity
factor at height of 10m

% 3.5KW Windspot

for i=1:M
P_cof(i)=-1E-06*V(i)^6 + 0.0001*V(i)^5 - 0.0032*V(i)^4 +
0.0369*V(i)^3 - 0.1457*V(i)^2 + 0.2131*V(i) - 0.0163
end

P_annual_50_S=365*24*(sum(fu_50.*P_cof)); % Annual power generation
at height of 50m
P_annual_49_S=365*24*(sum(fu_49.*P_cof)); % Annual power generation
at height of 49m
P_annual_40_S=365*24*(sum(fu_40.*P_cof)); % Annual power generation
at height of 40m
P_annual_30_S=365*24*(sum(fu_30.*P_cof)); % Annual power generation
at height of 30m
P_annual_10_S=365*24*(sum(fu_10.*P_cof)); % Annual power generation
at height of 10m

f_cap_50m_S=P_annual_50_S/(365*24*(sum(fu_50.*3.5))); % Capacity
factor at height of 50m
f_cap_49m_S=P_annual_49_S/(365*24*(sum(fu_49.*3.5))); % Capacity
factor at height of 49m
f_cap_40m_S=P_annual_40_S/(365*24*(sum(fu_40.*3.5))); % Capacity
factor at height of 40m
f_cap_30m_S=P_annual_30_S/(365*24*(sum(fu_30.*3.5))); % Capacity
factor at height of 30m
f_cap_10m_S=P_annual_10_S/(365*24*(sum(fu_10.*3.5))); % Capacity
factor at height of 10m
```

APPENDIX B

Matlab code for BEM method

```
%This Matlab script is developed to estimate the performance of wind
turbine based on BEM method
%Incorporating the tip loss, rotational effect, turbulent wake and
skewed wake correction
%Application on 3.5KW Windspot
%done by Liu Su

%% Warning: error can occur if one try to run the code under
unrealistic wind turbine configuration or operating conditions


%% Variable Declaration 1: blade information (user input)

%%%%%%%%%%%%%%%%%%%%%%%%%%%%%%%%%%%%%%%%%%%%%%%%%%%%%%%%%%%%%%%%%%%%%%%
%Blade geometry data

%Blade section data:radius, chord length,pitch angle and element
length
I=load('Windspot blade information1.txt');
geo_data=I(:, [1 2 3 4]); %radius, chord length, section pitch angle
and element length
%N=input('N=') ;number of section
N=length(geo_data(:,1));
%B=input('B=');%number of blades
B=3;
%R=input('R='); % the radius of the blade in meters
% R0=0.405; %R0=1.044; the radius of the blade at the root in meters
% R=1.825; % the radius of the blade at the tip in meters
R0=0.405; %R0=1.044; the radius of the blade at the root in meters
R=2; % the radius of the blade at the tip in meters

%%%%%%%%%%%%%%%%%%%%%%%%%%%%%%%%%%%%%%%%%%%%%%%%%%%%%%%%%%%%%%%%%%%%%%%
%Airfoil aerodynamic data

H=load('Windspot airfoil data2.txt');
aero_data=H(:,[1 2 3]);%Angle of attack,lift coefficient and drag
coefficient

%% Variable Declaration 2: operating conditions (user input)

%D=input('D='); % the density of air(user input)
D=1.225; % the density of air(user input)
%blade rotational speed
```

```
% Rot1=72; %blade rotational speed in RPM
% Rot=Rot1*pi*2/60; % blade rotational speed in rad/s
Rot=12; % blade rotational speed in rad/s
pitch=3; % in degrees
%pitch=input('pitch='); % blade root pitch angle
M=input('M='); %highest wind speed value

%% Calculation procedure: the algorithm refers to Figure 4.7

Eff=1; % the mechanical(including electrical)efficiency
Cpmax=16/27; %the betz limit power coefficient
A=pi*R^2; % the swept area of the turbine
iter=0;
L=length([5:M]);
Q=zeros(L,1);
Ct1=zeros(L,1);
P=zeros(L,1);
Cp=zeros(L,1);
for V=5:M
    iter=iter+1;
    TSR=Rot*R/V; %Tip speed ratio

    %======= Calculation part
=========================================

    a=0.3;
    %a=input('a='); %guess value of axial induction factor
    aprime=0.1;
    %aprime=input('aprime='); %guess value of angular induction
factor
    achieved_err=0.01;

    for X=1:N; % it will decide the accuracy of calculation(user
input)
        R1=geo_data(X,1);
        Thita_pitch=geo_data(X,3)+pitch; %section pitch angle
        C=geo_data(X,2); %chord length according to the geometry
        LL=geo_data(X,4);
        LSR=TSR*R1/R; % the local speed ratio
        Sol=(B*C)/(2*pi*R1); % local solidity
        guess_err=1;
        guessap_err=1;
        iter3=0;
        while (guess_err>achieved_err || guessap_err>achieved_err) &&
iter3<500
            Phi=atan((1-a)/((1+aprime)*LSR));

            %Incorporating Tip loss

            F=(2/pi)*(cos(exp(B*(R1-R)/(2*R1*sin(Phi))))^(-1);
%considering tip loss
            %   Fhub=(2/pi)*(cos(exp(B*(R0-R1)/(2*R1*sin(Phi))))^(-
1)
            %   F=Ftip*Fhub
            %F=1;
            Phi_degree=Phi*180/pi;
            Aoa=Phi_degree-Thita_pitch;
            err=abs(Aoa-aero_data(:,1));
            err_index = find(err == min(err)); %error
            err_index=min(err_index);
```

```
            Cl_non=aero_data(err_index,2);%non-rotation lift
coefficient
            Cd=aero_data(err_index,3);

            %Incorporating 3D correction of Snel for non-rotation
lift coefficient

            err1=abs(aero_data(:,2)-0);
            err_index1=find(err1 == min(err1));
            Aoa_zero=aero_data(err_index1,1);%angle of attack when
lift coefficient=0
            Cl_pot=2*pi*sin((Aoa-Aoa_zero)*pi/180);
            Cl=Cl_non+3.1*((LSR^2)/(1+LSR^2))*((C/R1)^2)*(Cl_pot-
Cl_non);
            %%centrifugal pumping mechanism correction
            % f=0.8;
            % Aoa_rot=Aoa+((0.3/(2*pi))*1.5*(1-
f)*(C/R1)*((LSR^2)/(1+LSR^2)))*180/pi;
            % err1=abs(aero_data(:,2)-0);
            % err_index1=find(err1 == min(err1));
            % Aoa_zero=aero_data(err_index1,1);%angle of attack when
lift coefficient=0
            % Cl=Cl_non+1.5*(cos(Aoa_rot*pi/180)+0.3*cos((Aoa_rot-
Aoa_zero)*pi/180)*(1-f)*(C/R1)*((LSR^2)/(1+LSR^2)));
            % Cd=Cd+1.5*sin(Aoa_rot*pi/180)*(1-
f)*(C/R1)*((LSR^2)/(1+LSR^2));

            %%stall delay correction
            % err1=abs(aero_data(:,2)-0);
            % err_index1=find(err1 == min(err1));
            % Aoa_zero=aero_data(err_index1,1);%angle of attack when
lift coefficient=0
            % err_index2=find(aero_data(:,2)==max(aero_data(:,2)));
            % Aoa_max=aero_data(err_index2,1);
            % Aoa_shift=(Aoa_max-
Aoa_zero)*((C/R1/0.136)*(0.1517*R1/C)^(1/1.084)-1);
            % Aoa_rot=Aoa+Aoa_shift;
            % err3=abs(Aoa_rot-aero_data(:,1));
            % err_index3 = find(err3 == min(err3)); %error
            % err_index3=min(err_index3);
            % Cl=aero_data(err_index3,2)+0.1*Aoa_shift;%non-rotation
lift coefficient
            Ct=Sol*((1-a)^2)*(Cl*cos(Phi)+Cd*sin(Phi))/(sin(Phi))^2

            %Incorporating Buhl empirical correction

            if  Ct>0.96
                a1=(18*F-20-3*(Ct*(50-36*F)+12*F*(3*F-4))^0.5)/(36*F-
50);
                %a1=(1/F)*(0.143+(0.0203-0.6427*(0.889-Ct))^0.5)
%considering turbulent wake
                aprime1=a1*(Cl*sin(Phi)-
Cd*cos(Phi))/((Cl*cos(Phi)+Cd*sin(Phi))*LSR);
                %aprime1=0.5*((1+4*a1*(1-a1)/LSR^2)^0.5-1)
                %aprime=a*(Cl*cos(Phi)-
Cd*sin(Phi))/(LSR*(Cl*cos(Phi)+Cd*sin(Phi)));
            else

a1=(1+(4*F*(sin(Phi))^2)/(Sol*(Cl*cos(Phi)+Cd*sin(Phi))))^(-1);
```

```
                aprime1=a1*(Cl*sin(Phi)-
Cd*cos(Phi))/((Cl*cos(Phi)+Cd*sin(Phi))*LSR);
            end
            guess_err=abs(a1-a);
            guessap_err=abs(aprime1-aprime);
            a=a1;
            aprime=aprime1;
            iter3=iter3+1;
        end
        Ct1(iter)=(Ct*2*R1*LL+Ct1(iter))/(R^2-R0^2);
        Q(iter)=4*aprime*(1-a)*D*V*pi*(R1^3)*Rot*LL+Q(iter); % Torque
        P(iter)=Q(iter)*Rot; % power generation
        P_contain=0.5*D*A*V^3;
        Cp(iter)=P(iter)./P_contain;
    end
end

%% Results report

figure(1)
plot([5:M],smooth(Cp),'LineWidth',3,'MarkerSize',18)
set(gca,'XTick',5:2.5:25)
set(gca,'FontSize',20)
xlabel('Wind speed (m/s)','fontsize',22)
ylabel('Power coefficient (Cp)','fontsize',22);
```

Bibliography

[1] S. Shafiee and E. Topal, "When will fossil fuel reserves be diminished?," *Energy Policy*, vol. 37, pp. 181-189, 2009.

[2] A. Jha, "Wind turbine technology," 2011.

[3] S. Sawyer and A. Zervos, "Global Wind 2009 Report," *Global Wind Energy Council*, 2010.

[4] M. Hoogwijk, *et al.*, "Assessment of the global and regional geographical, technical and economic potential of onshore wind energy," *Energy Economics*, vol. 26, pp. 889-919, 2004.

[5] *World electricity consumption*. Available: http://www.indexmundi.com/world/electricity_consumption.html

[6] A. van Wijk and J. Coelingh, "Wind Power Potential in the OECD Countries, Department of Science," *Technology and Society, Utrecht University, Utrecht*, p. 35, 1993.

[7] "Masdar project remains on track," 2010.

[8] G. News. (September 04, 2010). *UAE tops world on per capita carbon foot print*. Available: http://gulfnews.com/news/gulf/uae/environment/uae-tops-world-on-per-capita-carbon-footprint-1.139335

[9] J. Ekanayake, *et al.*, "Dynamic modeling of doubly fed induction generator wind turbines," *IEEE Transactions on Power systems*, vol. 18, pp. 803-809, 2003.

[10] B. B. Sheet, "Wind Turbine Technology," ed, 2005.

[11] H. Glauert, "Aerodynamic theory, vol. 4," *Berlin, Germany: Julius Springer*, pp. 169-360, 1935.

[12] O. Vries, "Fluid dynamic aspects of wind energy conversion," DTIC Document1979.

[13] P. J. Moriarty, *et al.*, *Aerodyn theory manual*: National Renewable Energy Laboratory, 2005.

[14] H. Glauert, "A General Theory of the Autogyro. R. & M. No. 1111," *British ARC*, 1926.

[15] D. M. Pitt and D. A. Peters, "Theoretical prediction of dynamic-inflow derivatives," *Vertica*, vol. 5, pp. 21-34, 1981.

[16] H. Snel, *et al.*, *Sectional prediction of lift coefficients on rotating wind turbine blades in stall*: Netherlands Energy Research Foundation, 1994.

[17] H. Snel and J. Schepers, "Joint investigation of dynamic inflow effects and implementation of an engineering method," *Netherlands Energy Research Foundation, ECN. ECN-C—94-107*, 1995.

[18] J. Schepers and H. Snel, *Dynamic inflow: yawed conditions and partial span pitch control*: Netherlands Energy Research Foundation ECN, 1995.

[19] J. N. Sørensen, *et al.*, "Three-level, viscous-inviscid interaction technique for the prediction of separated flow past rotating wing," Technical University of Denmark, Department of Energy Engineering, 1986.
[20] M. O. L. Hansen, *et al.*, "State of the art in wind turbine aerodynamics and aeroelasticity," *Progress in Aerospace Sciences,* vol. 42, pp. 285-330, 2006.
[21] L. M. Milne-Thomson, *Theoretical aerodynamics*: Dover Pubns, 1966.
[22] W. J. M. Rankine and I. o. N. Architects, *On the mechanical principles of the action of propellers*, 1865.
[23] T. Wu, "Flow through a heavily loaded actuator disc," *Schiffstechnik,* vol. 9, pp. 134-8, 1962.
[24] M. D. Greenberg, *Nonlinear actuator disk theory and flow field calculations, including nonuniform loading*: National Aeronautics and Space Administration, 1970.
[25] M. Greenberg, "Nonlinear actuator disc theory," *Z Flugwissensch,* vol. 20, pp. 90-8, 1972.
[26] J. T. Conway, "Analytical solutions for the actuator disk with variable radial distribution of load," *Journal of Fluid Mechanics,* vol. 297, pp. 327-356, 1995.
[27] J. T. Conway, "Exact actuator disk solutions for non-uniform heavy loading and slipstream contraction," *Journal of Fluid Mechanics,* vol. 365, pp. 235-267, 1998.
[28] H. A. Madsen, *The actuator cylinder: a flow model for vertical axis wind turbines*: Institute of Industrial Constructions and Energy Technology, Aalborg University Centre, 1982.
[29] R. Arieli and M. Tauber, "Computation of subsonic and transonic flow about lifting rotor blades," *AIAA Atmospheric Flight Mechanics Conference* 1979.
[30] C. Borland, *et al.*, "Numerical solution of three-dimensional unsteady transonic flow over swept wings," *AIAA journal,* vol. 20, pp. 340-347, 1982.
[31] N. Sankar, *et al.*, "Implicit Conservative Algorithm for Steady and Unsteady Three-Dimensional Transonic Potential Flows," 1981.
[32] J. Steger, *A conservative implicit finite difference algorithm for the unsteady transonic full potential equation*, 1980.
[33] F. Caradonna, *et al.*, "Finite difference modeling of rotor flows including wake effects," *Journal of the American Helicopter Society,* vol. 29, p. 26, 1984.
[34] T. D. Stovall, "Simulations of wind turbine wake interactions in OpenFOAM," UNIVERSITY OF COLORADO AT BOULDER, 2010.
[35] L. J. Fingersh, *et al.*, "Wind tunnel testing of NREL's unsteady aerodynamics experiment," *AIAA paper,* vol. 35, 2001.
[36] D. A. Simms and N. R. E. Laboratory, *NREL unsteady aerodynamics experiment in the NASA-Ames wind tunnel: A comparison of predictions to measurements*: National Renewable Energy Laboratory, 2001.
[37] N. Sørensen, "Evaluation of 3D effects from 3D CFD computations," 2000.
[38] E. P. N. Duque, *et al.*, "Navier-Stokes and comprehensive analysis performance predictions of the NREL phase VI experiment," *Journal of Solar Energy Engineering,* vol. 125, p. 457, 2003.
[39] G. Xu and L. N. Sankar, "Application of a viscous flow methodology to the NREL phase VI rotor," 2002.
[40] J. Johansen, *et al.*, "Detached-eddy simulation of flow around the NREL Phase VI blade," *Wind Energy,* vol. 5, pp. 185-197, 2002.
[41] G. Wind, "Report. Global Wind Energy Council (GWEC), 2009," ed, 2008.
[42] G. Wind, "Report. Global Wind Energy Council (GWEC), 2010," 2010.

[43] R. Energy, "Wind Power's Contribution to Electric Power Generation and Impact on Farms and Rural Communities," ed: US Government Accountability Of ce, GAO-04-756, Washington, DC, 2004.
[44] J. Kelleher and J. Ringwood, "A computational tool for evaluating the economics of solar and wind microgeneration of electricity," *Energy,* vol. 34, pp. 401-409, 2009.
[45] P. Pilavachi, *et al.*, "The energy policy of the Republic of Cyprus," *Energy,* vol. 34, pp. 547-554, 2009.
[46] J. Seguro and T. Lambert, "Modern estimation of the parameters of the Weibull wind speed distribution for wind energy analysis," *Journal of Wind Engineering and Industrial Aerodynamics,* vol. 85, pp. 75-84, 2000.
[47] R. Pallabazzer and A. A. Gabow, "Wind resources of Somalia," *Solar Energy,* vol. 46, pp. 313-322, 1991.
[48] S. Pashardes and C. Christofides, "Statistical analysis of wind speed and direction in Cyprus," *Solar Energy,* vol. 55, pp. 405-414, 1995.
[49] P. C. Putman, "Power from the wind," *Van Norstrand Reinhold and Co. New York,* 1948.
[50] R. Sherlock, "Analyzing winds for frequency and duration," *Meteorological Monographs,* vol. 4, pp. 72-79, 1951.
[51] R. S. Chhikara and L. Folks, *The inverse Gaussian distribution: theory, methodology, and applications* vol. 95: CRC, 1989.
[52] R. Luna and H. Church, "Estimation of Long-Term Concentrations Using aUniversal'Wind Speed Distribution," *Journal of Applied Meteorology,* vol. 13, pp. 910-916, 1974.
[53] W. Weibull, "A statistical distribution function of wide applicability," *Journal of applied mechanics,* vol. 18, pp. 293-297, 1951.
[54] K. Ulgen and A. Hepbasli, "Determination of Weibull parameters for wind energy analysis of Izmir, Turkey," *International journal of energy research,* vol. 26, pp. 495-506, 2002.
[55] A. S. S. Dorvlo, "Estimating wind speed distribution," *Energy Conversion and Management,* vol. 43, pp. 2311-2318, 2002.
[56] V. Karsli and C. Gecit, "An investigation on wind power potential of NurdaI-Gaziantep, Turkey," *Renewable Energy,* vol. 28, pp. 823-830, 2003.
[57] A. Keyhani, *et al.*, "An assessment of wind energy potential as a power generation source in the capital of Iran, Tehran," *Energy,* vol. 35, pp. 188-201, 2010.
[58] M. Elhadidy and S. Shaahid, "Wind resource assessment of eastern coastal region of Saudi Arabia," *Desalination,* vol. 209, pp. 199-208, 2007.
[59] "CUP ANEMOMETER CALIBRATION PROCEDURE," 1997.
[60] I. T. Isam Janajreh*, "Wind Data Collection and Analyses at Masdar City for Wind Turbine Assessment," *Int. J. of Thermal & Environmental Engineering,* vol. 1, pp. 43-50, 2010.
[61] J. F. Manwell, *et al.*, *Wind energy explained*: Wiley Online Library, 2002.
[62] J. W. Cooley and J. W. Tukey, "An algorithm for the machine calculation of complex Fourier series," *Math. Comput,* vol. 19, pp. 297–301, 1965.
[63] V. C. Chen and H. Ling, *Time-frequency transforms for radar imaging and signal analysis*: Artech House Publishers, 2002.
[64] I. Daubechies, "The wavelet transform, time-frequency localization and signal analysis," *Information Theory, IEEE Transactions on,* vol. 36, pp. 961-1005, 1990.

[65] C. Torrence and G. P. Compo, "A practical guide to wavelet analysis," *Bulletin of the American Meteorological Society,* vol. 79, pp. 61-78, 1998.
[66] F. Chellali, *et al.*, "Wavelet spectral analysis of the temperature and wind speed data at Adrar, Algeria," *Renewable Energy,* vol. 35, pp. 1214-1219, 2010.
[67] M. Farge, "Wavelet transforms and their applications to turbulence," *Annual Review of Fluid Mechanics,* vol. 24, pp. 395-458, 1992.
[68] T. J. Chang, *et al.*, "Assessment of wind characteristics and wind turbine characteristics in Taiwan," *Renewable Energy,* vol. 28, pp. 851-871, 2003.
[69] I. Janajreh, *et al.*, "Aerodynamic flow simulation of wind turbine: downwind versus upwind configuration," *Energy conversion and management,* vol. 51, pp. 1656-1663, 2010.
[70] J. Isam, *et al.*, "Numerical Simulation of Tower Rotor Interaction for Downwind Wind Turbine," *Modelling and Simulation in Engineering,* vol. 2010, 2010.
[71] D. Hu, *et al.*, "A study on stall-delay for horizontal axis wind turbine," *Renewable energy,* vol. 31, pp. 821-836, 2006.
[72] H. Glauert, "Airplane propellers," *Aerodynamic theory,* vol. 4, pp. 169-360, 1935.
[73] J. F. Manwell, *et al.*, *Wind energy explained: theory, design and application*: John Wiley & Sons Inc, 2010.
[74] H. Glauert, *The analysis of experimental results in the windmill brake and vortex ring states of an airscrew*: HMSO, 1926.
[75] M. L. Buhl and N. R. E. Laboratory, *A new empirical relationship between thrust coefficient and induction factor for the turbulent windmill state*: National Renewable Energy Laboratory, 2005.
[76] A. Eggers, "Modeling of yawing and furling behavior of small wind turbines," 2000, pp. 1-11.
[77] C. Lindenburg, "Investigation into rotor blade aerodynamics," *Netherlands Society for Energy and the Environment, Paper ECN-C-03-025,* 2003.
[78] D. A. S. M.M. Hand, L.J. Fingersh, D.W. Jager, J.R. Cotrell, S. Schreck, and S.M. Larwood, "Unsteady Aerodynamics Experiment Phase VI: Wind Tunnel Test Configurations and Available Data Campaigns," 2001.
[79] W. D. Musial, *et al.*, *A comparison of two-and three-dimensional S809 airfoil properties for rough and smooth HAWT rotor operation*: Solar Energy Research Inst., 1990.
[80] A. Betz, "Das maximum der theoretisch möglichen ausnützung des windes durch windmotoren," *Zeitschrift für das gesamte Turbinenwesen,* vol. 26, pp. 307–309, 1920.
[81] "Site Expérimental pour le Petit Eolien de Narbonne Rapport de Test n ° 19 version 2 du 27 avril 2010 Eolienne Sonkyo Energy Windspot 3.5 kW," 2010.
[82] G. W. E. Council, "Global wind report 2010," ed, 2010.
[83] L. A. Viterna and R. D. Corrigan, "Fixed pitch rotor performance of large horizontal axis wind turbines," *Large Horizontal-Axis Wind Turbines,* vol. 1, pp. 69-85, 1982.
[84] NWTC.
[85] M. Kawaguti, "Numerical solution of the Navier-Stokes equations for the flow around a circular cylinder at Reynolds number 40," *J. Phys. Soc. Japan,* vol. 8, pp. 747-757, 1953.

[86] J. N. Sørensen and A. Myken, "Unsteady actuator disc model for horizontal axis wind turbines," *Journal of Wind Engineering and Industrial Aerodynamics,* vol. 39, pp. 139-149, 1992.
[87] J. N. Sørensen and C. W. Kock, "A model for unsteady rotor aerodynamics," *Journal of Wind Engineering and Industrial Aerodynamics,* vol. 58, pp. 259-275, 1995.
[88] H. A. Madsen, "A CFD analysis of the actuator disc flow compared with momentum theory results," 1996, pp. 109-124.
[89] I. Ammara, *et al.*, "A viscous three-dimensional differential/actuator-disk method for the aerodynamic analysis of wind farms," *Journal of Solar Energy Engineering,* vol. 124, p. 345, 2002.
[90] A. Crespo, *et al.*, "Experimental validation of the UPM computer code to calculate wind turbine wakes and comparison with other models," *Journal of Wind Engineering and Industrial Aerodynamics,* vol. 27, pp. 77-88, 1988.
[91] F. R. Menter, "Zonal two equation kappa-omega turbulence models for aerodynamic flows," *c1993,* vol. 1, 1993.
[92] F. R. Menter, "Two-equation eddy-viscosity turbulence models for engineering applications," *AIAA journal,* vol. 32, pp. 1598-1605, 1994.
[93] C. E. Lynch, "Advanced CFD methods for wind turbine analysis," 2011.
[94] J. D. Anderson and J. F. Wendt, *Computational fluid dynamics* vol. 206: McGraw-Hill, 1995.
[95] H. K. Versteeg and W. Malalasekera, *An introduction to computational fluid dynamics: the finite volume method*: Prentice Hall, 2007.
[96] J. H. Ferziger and M. Perić, *Computational methods for fluid dynamics* vol. 3: Springer Berlin etc, 1999.
[97] A. Fluent, "6.3 Documentation," *Fluent Inc., Lebanon, NH,* 2006.
[98] K. Kovalev, "Unstructured Hexahedral Non-conformal Mesh Generation," 2005.
[99] CIEMAT, 2010.
[100] W. Power, "Capacity Factor, Intermittency, and what happens when the wind doesn't blow," *Community Wind Power Fact Sheet,* 2008.